POLITECNICO DI MILANO
DEPARTMENT OF ELECTRONIC, INFORMATION AND BIOENGINEERING
PH.D PROGRAM IN INFORMATION TECHNOLOGY

TID MEKII:

A RAPID AND QUANTITATIVE DIAGNOSTIC SYSTEM FOR MALARIA

Doctoral Dissertation of:
Marco Giacometti

Supervisor:
Prof. Sampietro Marco

Tutor:
Prof. Fiorini Carlo Ettore

The Chair of the Doctoral Program:
Prof. Pernici Barbara

2020 – XXXII Cycle

Acknowledgements.

Many people contributed and are still contributing to the success of the Tid Mekii project without whose help it would have not been possible to have all the required multidisciplinary competences.
First, I would like to thank Prof. Riccardo Bertacco, head of the "Nanomagnetism for Biology and Spintronics group" (NaBis) and coordinator of the project, the core from whom the idea of the actual developed system was born and who invested precious and priceless time and resources in the organization and management of the project.
A special thanks goes to Prof. Marco Sampietro, head of the "Innovative Integrated Instrumentation for Nanoscience" (I^3N) who allowed me to work and carry out my master thesis and a doctoral course at his laboratory.
Among Sampietro's group warm thanks is due to Prof. Giorgio Ferrari, who gives strong and fundamental contributions to every project he is involved, as well as in Tid Mekii. His outstanding logic, intuition and problem solving abilities, that go far beyond science alone, are always overt and an example to anyone who works or simply converse with him.
I thank Prof. Gianfranco Beniamino Fiore, part of the Biomechanics Group for his valuable contribution and insights on the biological aspects of the project. Prof. Riccardo Bertacco, Prof. Giorgio Ferrari and Prof. Gianfranco Beniamino Fiore head the Tid Mekii team in all of three main different field of the project, respectively, nanomagnetism, electronics and electrochemistry and biology.
A personal thanks goes to all the past and actual master and Ph.D students which contributed and took part of the team: M. Monticelli, F. Milesi, L.P. Coppadoro, L.B. Callegari, A. Collovini, G. Benevento, E. Giuliani, F. Fagiani, L. Paroni.
My gratitude goes to Prof. P. Alano from Istituto Superiore di Sanitá, Prof. A. Spinello, Dr. R. Grande, Dr. A. Rizzo from Sacco Hospital, Prof. M.T. Raimondi, head of the "mechanobiology lab", Dr. P. Onambele and the medical staff of the Hopital Saint Luc of Mbalmayo for their contributions and support in the testing of the device.

Abstract

MALARIA is a life-threatening parasitic disease killing more than 400 thousands people every year, 61% of which are children aged under 5 years old. The fight against malaria demands billions of USD each year representing an unbearable burden which exasperate the already difficult economic situation of most of the malaria endemic countries. Despite many efforts have been put into the research of antimalarial drugs and prevention methods, the onset of drug resistance and the mosquito habits adaptations risk of putting them in jeopardy. In this ongoing struggle, diagnostic tools represent a fundamental guidance for a prompt and proper treatment of the disease, helping to reduce the mortality rate and counteracting the occurrence of adaptations of the parasite to antimalarials. The panorama of currently diagnostic methods sees three main techniques: microscopy examination, rapid diagnostic test and polymerase chain reaction based diagnosis. Their cost, complexity and time requirements, however, are not always adequate to allow a wide spread to support the constant need. It is precisely to face this lack that the World Health Organization itself calls for development of low cost, easy to use and reliable new diagnostic techniques. The developed innovative system here presented is aimed to support this request by proposing a panplasmodic, quantitative, easy to use, rapid and potentially low cost diagnostic tools. The name of the project itself, *Tid Mekii*, the name of the malaria in Cameroon language, highlights its aim and purpose to provide a rapid and valid alternative up to the actual devices and methods while ensuring a low cost to guarantee its wide spread in the poorest endemic countries. The technique relies on the selective magnetophoretic attraction and consequent electrical impedance detection and quantification of malaria infected red blood cells (iRBCs). The tests performed with the device demonstrate its capability of detecting and quantify both hemozoin crystals (HCs), i.e. the malaria pigment, and iRBCs concentrations down to, respectively, 10^4 HCs/μl and 10 iRBCs/μl in less than 10 minutes. The possibility to perform a follow up of the treatment and discriminating between different stages of the disease has emerged although further dedicated investigations are required to confirm said features. A preclinical validation have been carried out at Hopital Saint Luc of Mbalmayo, Cameroon, Africa on 108 suspected malaria patients. The outcomes of this study show the absence of false

negatives (100% sensitivity) but few false positives occurrences (65.5% specificity). However, the high inter-patient differences in blood properties prevented an accurate quantification of the parasitaemia. These results prove the possibility of the developed instrument and technique to become a reliable and useful diagnostic tool up to the task of competing with currently available ones and providing a valid alternative to them. The idea and the device here presented have been the subject of two social patent applications in which the inventors give up any revenues deriving from its exploitation which should be reinvested for social purposes.

Figure 1: *Photograph of Tid Mekii team and medical staff of Hopital Saint Luc of Mbalmayo taken during the preclinical validation carried out in Cameroon, Africa.*

Contents

CHAPTER 1

Introduction

In this chapter an introduction on malaria disease and its social impact is given (Section1.1). Afterwards, in Section1.2 the prevention and treatments procedures are here briefly presented. Moreover, the main methods for the diagnosis of the disease, both already commercial and at a research stage, are shown (Section1.3). Finally in Section1.4 the Tid Mekii project, which aim to develop an innovative sensor for the diagnosis of malaria, is presented.

1.1 Malaria disease

Malaria is one of the most diffused life-threatening disease worldwide, mainly in the African, South-east Asia, Eastern Mediterranean and South American regions as showed in Figure 1.1. It is caused by a family of protozoan parasites called *Plasmodium*, trasmitted to human hosts or other animals species like mammals, birds or reptiles through the bite of infected female mosquitoes of the *Anopheles* family. [1,2] Although the *Plasmodium* group comprises more than one hundred strains, only five of them (*P. falciparum, P. vivax, P. malariae, P. ovale and P. knowlesi*) can infect humans. [2, 3] However, only the first two species (i.e *vivax* and *falciparum*) are responsible for the most severe infections and symptoms. In particular, the former is mostly present in Latin America and Asia. Despite it does not cause lethal infections, it can persist into the blood stream for years after the mosquito bites facilitating the spreading of the disease. The latter, instead, is widespread in African continent and it is the most virulent and fatal one due to its high capability of multiplying. [2–4] In Figure1.2 the spreading of the two *Plasmodium* strains, taken from the "World Malaria Report 2017" by the *World Health Organization (WHO)*, is reported.

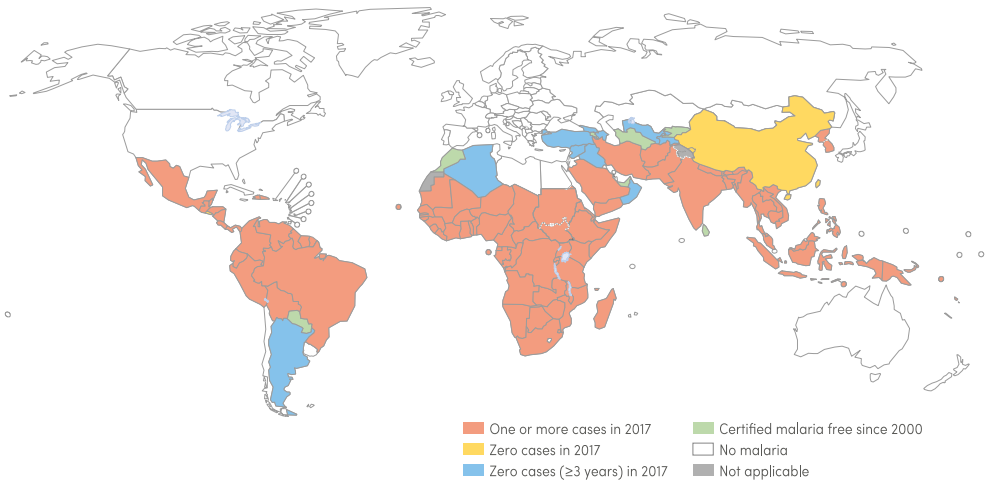

Figure 1.1: *Malaria endemic countries in 2017 compared to 2010. Countries with zero cases over at least the past 3 consecutive years are considered to be malaria free. [1].*

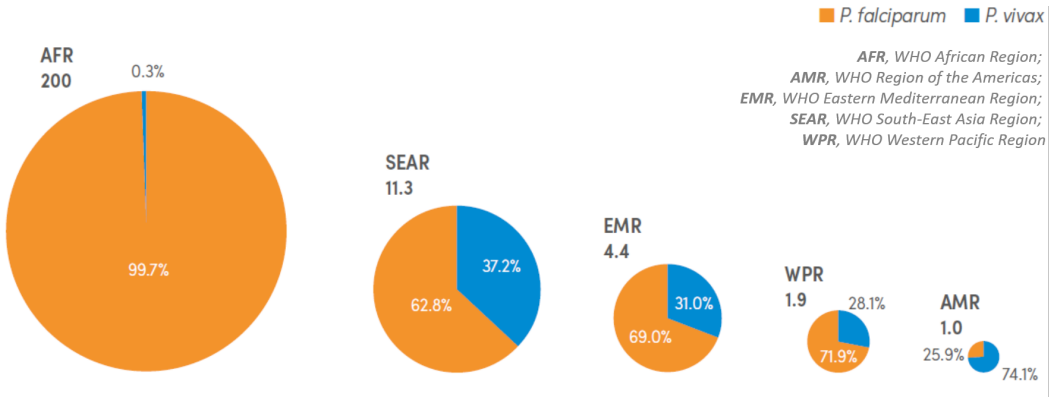

Figure 1.2: *Estimated malaria cases (millions) by WHO region in 2017. The area of the circles is proportional to the estimated number of cases in each region. [1]*

Initial manifestations of malaria begin 1-4 weeks after mosquito bite or even later if antimalarial drugs have been taken. [5,6] Some of the most common symptoms, almost similar for all *Plasmodium* species, include fever, headache, nausea, convulsion, joint and muscular pain. [7–9] The peculiarity of malaria is the cyclicity of the aforementioned symptoms approximately every 2 days. [10] Severe malaria infections, usually caused by *P. falciparum*, may cause respiratory distress, anaemia, pneumonia, kidney failure, enlarged liver, encelophalopathy, seizures and coma. [8, 11–13]
Lots and constant efforts and funds have been put in place from 2010 (see Figure 1.3) allowing a decrease in the number of cases by 18% globally and in the number of deaths worldwide by 28%. In particular, the number of malaria cases per 1000 population decreased steadily globally (Figure 1.4), going from 72 in 2010 to 59 in 2017. However, a reduction in this trend has been registered from 2014, due to an increase in American Region (AMR) and a flattening in the remaining regions except in South-East Asia Region (SEAR). In 2017 approximately 435000 deaths from malaria were registered, with a 3.5% decrease in respect to 2016 data. [1, 14] Moreover, compared to 2010, all regions, except AMR, registered a reduction in malaria mortality rate. Despite 93% of

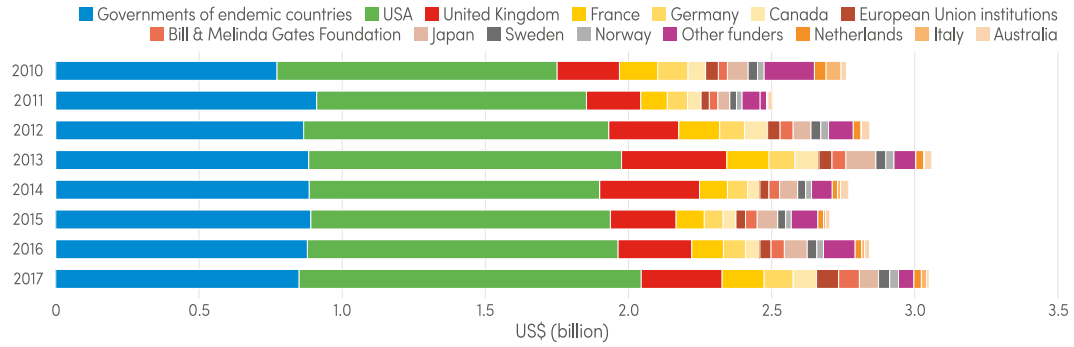

Figure 1.3: *Investments in malaria control and elimination programs from 2010 to 2017. [1].*

all death are accounted in African region, 88% of the reduction rate in mortality cases is observed in the same region. Children aged under 5 years present the highest risk of death, mainly due to the still underdeveloped immune system. Indeed, 61% of the deaths in 2017 concern this age group. [1] In Figure 1.5 the table reporting the number of malaria deaths registered each year from 2010 to 2017 and divided by regions is reported. Despite the aforementioned positive trends, malaria is still the most important parasitic disease in the world. Therefore great efforts are still needed on all three main fronts typical of the fight against infectious diseases, i.e. *prevention, treatment and diagnosis*. The first two topics will be deepened later in Section 1.2 while the latter in Section 1.3.
Besides the consequences on life and health themselves, malaria also brings with it social and economical issues. Some evidences suggest that it is both a cause and a result of poverty. [15] Every year, the economic cost of malaria, comprising health care, loss in investments, working days due to sickness and tourism, has been estimated to be over 12 billion USD every year. [16]

1.1.1 Biology and pathogenesis of malaria

Malaria, in human being, is caused by the strains of the *Plasmodium* parasites, *falciparum, vivax, ovale, malariae* and *knowlesi*, transmitted by the female mosquitoes of the *Anopheles* family which includes more than 400 different species. [2]
Malaria cycle in human host, graphically represented in Figure 1.6, begins with the bite of a malaria-infected mosquito. During the blood meal the mosquito inoculate an immature form of the *Plasmodium*, the *sporozoites*, a motile spore-like stage typical of some parasitic sporozoans, into the bloodstream. Travelling trough the blood vessels, the *sporozoites* reach the host liver after 30 minutes from the event and infecting its cells (*hepatocytes*). Once invaded the liver cell, the parasites initiate their first phase of mutation into *schizonts*. In the following one or two weeks, depending on the *Plasmodium* strain, each *schizont* multiplies asexually producing thousands of *merozoites*. The proliferation inside *hepatocytes* goes on until the cells rupture. Consequently to this event, *merozoites* are released into the bloodstream where they can now infect the red blood cells (*erythrocytes*) beginning the second phase of mutation and multiplication called *intra-erythrocytic stage*. [18, 19] In this phase the first malaria symptoms, such as fever and headache, appear. Inside the *erythrocytes* the *merozoites* develop through three consequential stages, *ring, thropozoites and schizonts* (see Figure 1.7), until the

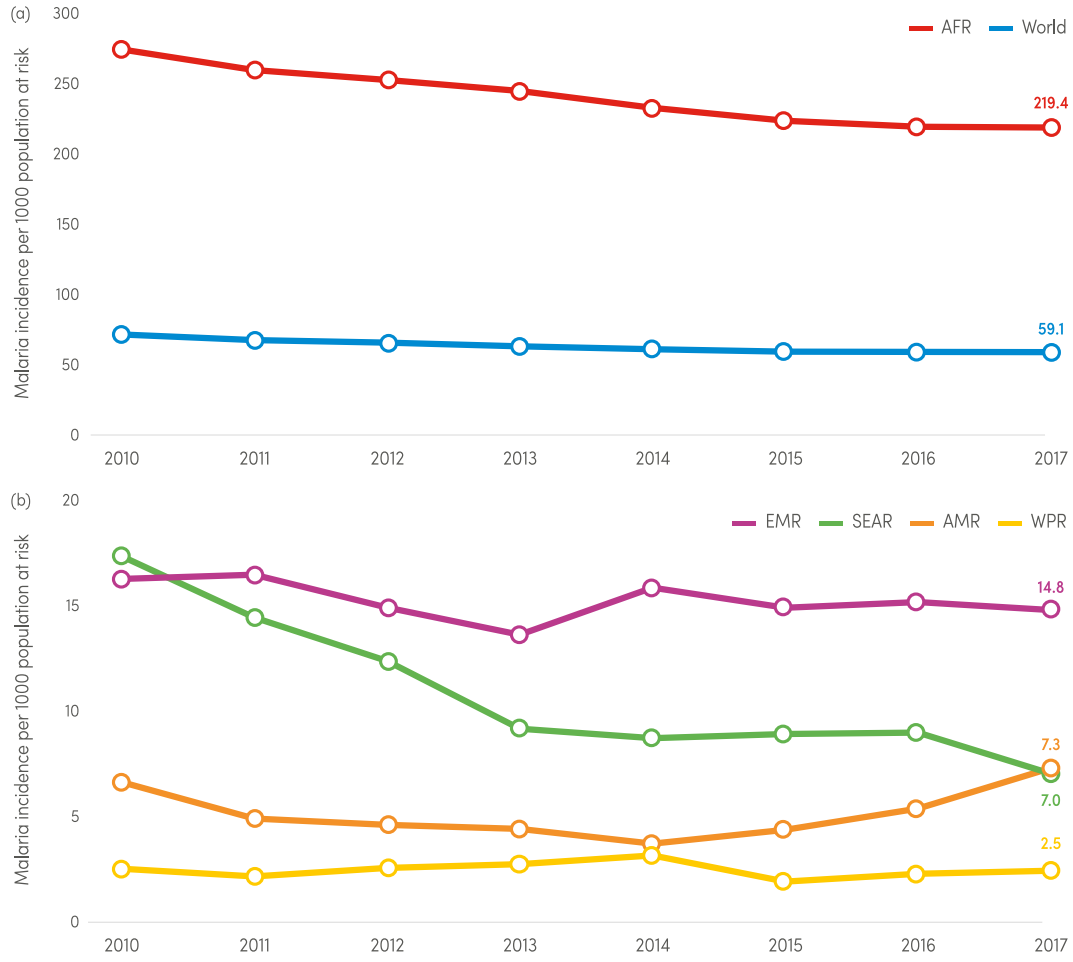

Figure 1.4: *Rate of incidence of malaria cases (a) globally and (b) by regions per 1000 population at risk. [1].*

rupture of the red blood cell. During this phase each parasite can reproduce asexually producing up to 24 new *merozoites*, which are released into the blood stream, after the lysis of the host cell, where they can infect new erythrocytes and starting the cycle anew. Thus a potentially infinite loop is formed which leads to a progressive increase in the level of parasitaemia. The time between the *erythrocytic* infection and its rupture depends on the *Plasmodium* strain causing the infection and it is usually 24 to 72 hours long, corresponding to the interval between fever attacks, symptom typical of malaria. Furthermore, few *merozoites* mutate into a sexual stage: female and male *gametocytes*. These forms of the parasite accumulate and remain in the human blood stream for even a year in the human host after the infection. Hence human represent a reservoir of *gametocytes* which are withdrew and transferred to another mosquito that bites the infected person. Inside mosquito's gut they can mate and reproduce producing embryonic forms called *ookinetes* which, in the end, produce new *sporozoites* that accumulate in the salivary glands of the insect. *Plasmodium* is then ready to be released and infect another host perpetuating the cycle and diffusion of the disease [20].

	Number of deaths							
	2010	2011	2012	2013	2014	2015	2016	2017
African	555 000	517 000	489 000	467 000	446 000	432 000	413 000	403 000
Americas	480	450	400	400	300	320	460	630
Eastern Mediterranean	8 070	7 280	7 340	6 750	8 520	8 660	8 160	8 300
European	0	0	0	0	0	0	0	0
South-East Asia	39 800	32 800	28 400	21 800	24 100	25 200	25 600	19 700
Western Pacific	3 770	3 340	3 850	4 600	4 420	2 860	3 510	3 620
World	**607 000**	**561 000**	**529 000**	**500 000**	**483 000**	**469 000**	**451 000**	**435 000**
World (children aged under 5 years)	**444 600**	**405 000**	**371 000**	**344 000**	**322 000**	**302 000**	**283 000**	**266 000**

Figure 1.5: *Estimated number of malaria deaths between 2010 and 2017. [1]*

1.1.2 Hemozoin

During the intra-erythrocytic stage *Plasmodium* consume up to 65% of host red blood cell (RBC) haemoglobin and 80% of its cytoplasm to syntetize amino acids. [22], [23] During the digestion of these substances, inside the digestive vacuole of the *thropozoites*, monomeric α-haematin is produced which is toxic to both the parasite and the RBC itself due to its lytic agent properties that can lead to the disruption of cell membranes. [24] *Plasmodium*, therefore, converts α-hematin through bio-crystallization into β-haematin crystals, a chemically inert compound also called *hemozoin* (HC). [25–27] Often *hemozoin* is also referred to malaria pigment due to its typical brownish color. The structure of said molecule is shown in Figure 1.8. β-hematin crystals are made of dimers of hematin linked together by hydrogen bonds. The central Fe^{3+} ion of each hematin is connected to the oxygen of the carboxylate (RCOO-) side-chain of the adjacent hematin through an iron-oxygen coordinate bond. *Hemozoin* crystals produced by *Plasmodium* are usually composed by approximately 80000 heme molecules forming crystals 100-400 nm long with a brick like structure (1:1:8). [29, 30]
The number and the size of the hemozoin crystals in the erythrocyte depend on the stage of the parasite development, with the least amount of the crystals detected in the ring stage and the highest amount in the schizont stage. [31]
Hemozoin crystals present a bluish or brownish colour and exhibit interesting physical properties like paramagnetism and optical dichroism(i.e. their absorption spectrum of light depends on the propagation direction).
Of particular relevance for the aim of this thesis is the paramagnetic property of hemozoin which is given by the central iron ion of hematin in ferric state Fe^{3+}. The ion is in the high-spin configuration due to five unpaired electrons $3d^5$ resulting in a spin angular momentum S=5/2 thus owning paramagnetic behavior. [32, 33] Thus the magnetic susceptibility of HCs has been measured to be in the order of $3.2 \cdot 10^{-4}$ as reported by [34–36].
After the conversion of haemoglobin into hemozoin, the latter is expelled by the plasmodium inside the host RBC. Consequently, the infected erythrocyte, containing HCs, exhibit magnetic properties that are dependent by its crystals content. However, HCs

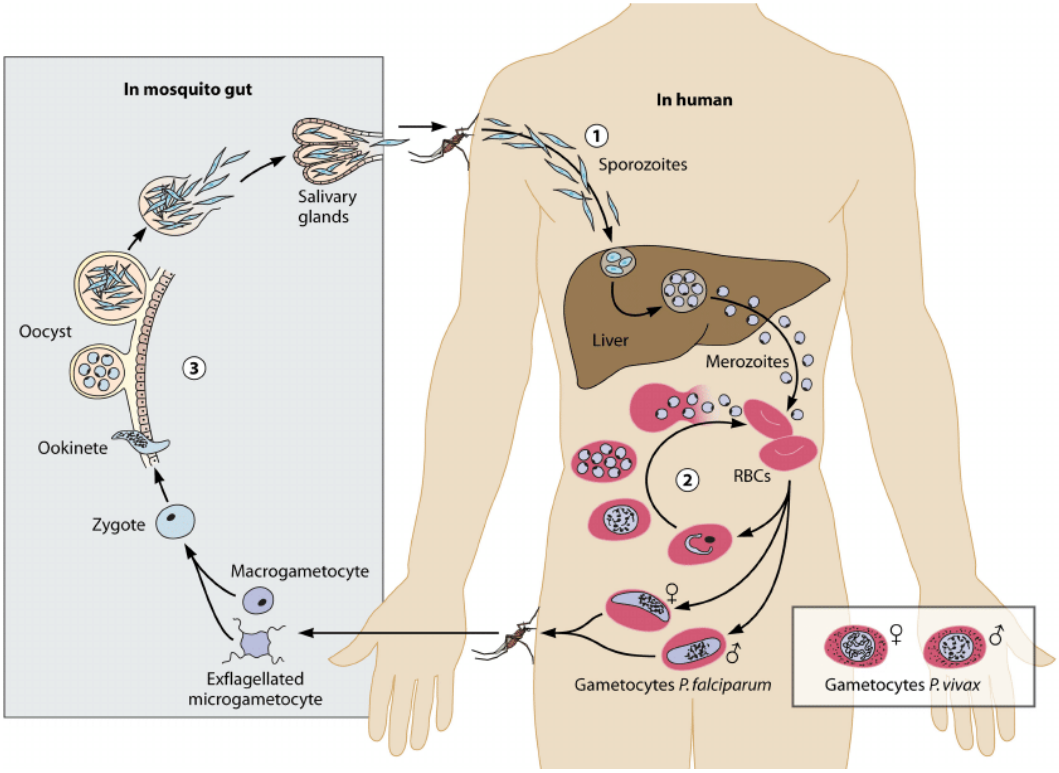

Figure 1.6: *Plasmodium life cycle and transmission: 1. Sporozoites inoculation in the human host through the bite of an infected mosquito and intra-hepatocytic stage; 2. Intra-erytocytic stage; 3. Plasmodium life cycle in mosquito. [17]*

can also be found free in blood after red blood cell lysis.
Since the formation of hemozoin is common and characteristic to all Plasmodium strain, and, moreover, its formation is essential for the survival of the parasite, malaria pigment is of overwhelming relevance for both diagnostic and treatment. As a matter of fact some commonly used antimalarial drugs aim at killing Plasmodium through the inhibition of α-haematin bio-crystallization.

1.2 Prevention and Treatments

Prevention and treatments, together with a prompt diagnosis, are the key elements for an effective eradication of a disease. In order to diffuse, Malaria, requires three key conditions:

- High human population density;
- High anopheles mosquito density;
- High transmission rates from mosquito to human and viceversa;

hence, in order to control and eliminate the presence of the disease it is necessary to act on the aforementioned fronts, in particular, for obvious reasons, on the last two. Prevention represents a more cost-effective way, in respect to treatment on long period, however the initial costs required are out of reach for some of the world's poorest countries. [38]

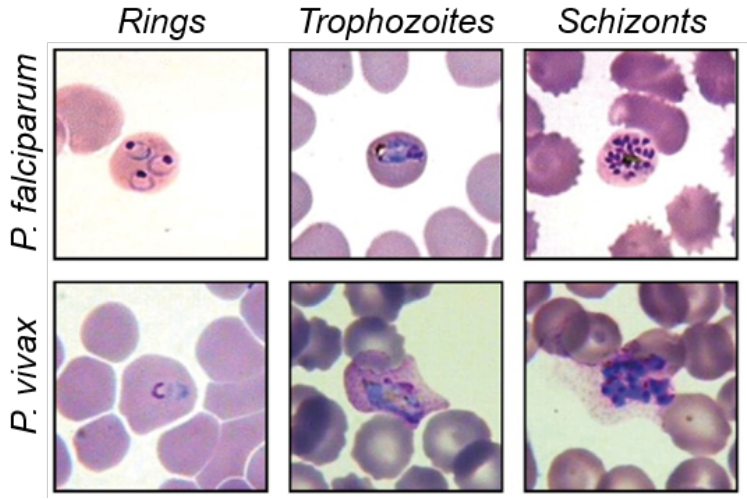

Figure 1.7: *Microscope images of intra-erithrocytic stages of Plasmodium falciparum and vivax. [21].*

The most effective methods to prevent malaria, according to the World Health Organization, are vector control (i.e. avoiding mosquito bites), chemoprevention (i.e. preventing infections by means of drugs) or mosquito elimination. In particular, WHO itself recommends the use of insecticide-treated mosquito nets (ITNs) and indoor residual spraying (IRS) to prevent mosquito bites in endemic regions. [1]
Sleeping under mosquito nets greatly decrease mosquito bites as they usually feed between dusk and dawn. However nets does not constitute a perfect barrier therefore they are often treated with insecticide in order to kill mosquitoes before they can cross the net. ITNs have been proved to be 50% more effective than untreated one and 70% compared with no net. [39] The insecticides mainly used are pyretroid, due to their low toxicity. The recommendation is to use them from dusk to dawn, and to tuck the edges under the mattress or to let it touch the ground. [40] From 2010 to 2017 ITNs coverage increased steadily of about 25% [1] and has been estimated that their use saved the lives of 250000 children in Sub-Saharan Africa. [40] IRS instead aims to control mosquito population by spraiyng insecticides on the inside walls of the houses as the insects usually rest on a nearby surface after a blood meal. The WHO recommends the use of DDT, although its use is decreasing nowadays due to its toxicity [41], cyfluthrin and deltamethrin [42].
However the presence of indoor insecticide caused a change in mosquitoes' habits which always more often tend to rest and live outdoors after a blood meal, making IRS less effective. This phenomenon is often referred to as insecticide resistance, even if it does non implies a real endurance of the insects to the chemical compounds used. [43] Mainly due to this reason the percentage of population using this kind of prevention has decreased by 2%, going from 180 million people covered in 2010 to 116 million in 2017, as shown in Figure 1.11. Other outdoor measures have been then taken to reduce mosquito bites and malaria spreading. Among them are the outdoor spraying of insecticides (mainly in agriculture), the reduction of available backwater or the addition of substances to it. [44]
There are also drugs to prevent the disease. However they can not be taken lifelong due to their side-effects and cost, making them unsuitable for a complete coverage of peo-

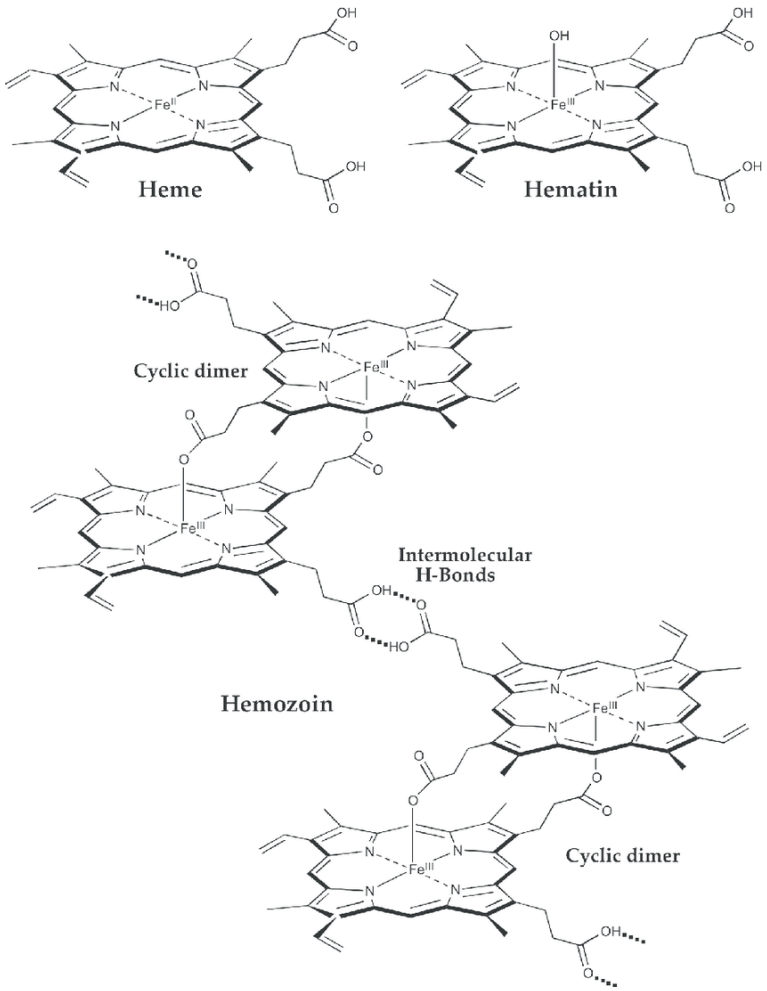

Figure 1.8: *Chemical structure of heme, hematin and hemozoin. [28]*

ple living in endemic regions but for short-term visitor or pregnant women. Drugs frequently used for prevention are mefloquine, atovaquone, doxycycline or proguanil. [45] Due to the delayed effect of these drugs it is recommended to take them at least one week before the arrival in the endemic country. [46] Also in this case, the extensive use of antimalarials is causing a partial resistace of the plasmodium to them. [47]
Among the prevention methods, social measures should also be mentioned, such as education, community participation and malaria awareness promotion. [48] Efforts are also being put in research to develop a non chemical vector control strategy based on genetic manipulation of mosquitoes to reduce their lifespan or make them more resistant to *Plasmodium*. Sterilization of Anopheles male is also ongoing in order to progressively reduce their population. [39]
Treatment of malaria is done through antimalarial drugs. The administration and family of medication to be used depends on the severity of the disease. In Figure 1.12 an extract from the "*World Malaria Report 2018*" containing WHO guideline for malaria treatment is reported. According to [1] all uncomplicated or simple infections should be treated with artemisinin-combination therapy (ACTs), i.e. a combination of artemisinins and other antimalarials such as mefloquine, amodiaquine, lumefantrine or sulfadox-

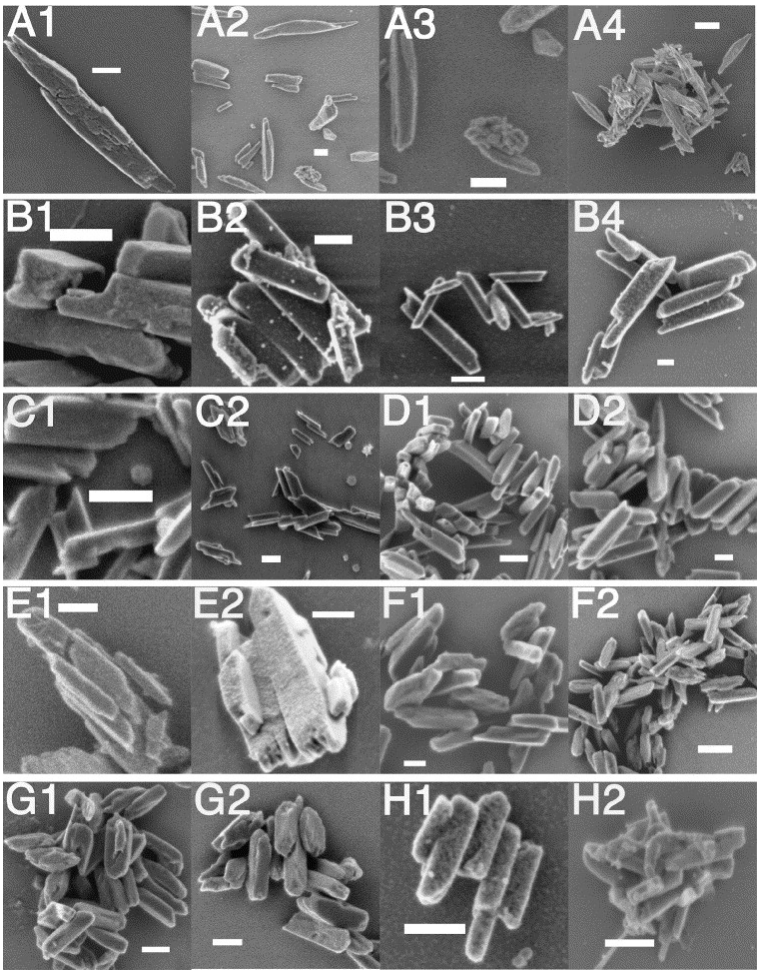

Figure 1.9: *SEM images of hemozoin crystals from plasmodium strains (from A to H) falciparum, vivax, P.ovale, malariae, brasilianum, knowlesi, yoelii. [37]*

ine/pyrimethamine. The combined use of these drugs has been proven to lower the probability of developing drug resistance to any component. [49] For pregnant women, instead, the combination of quinine and clindamycin should be delivered during the first trimester of pregnancy, while ACT during the second and third one. [50]
On the other hand, severe malaria, which is to be considered a medical emergency due to the mortality rates ranging from 10% to 50% [51], should be treated with intramuscular or intravenous medications like parenteral artesunate or its derivates artemether and arteether. [52] Moreover, patients affected by complicated malaria usually requires Intensive Care Unit support for breathing, fevers and seizures management. [53]
The development of specific resistance from *Plasmodium* to antimalarial medications is becoming a great issue nowadays. Resistances to all drugs except for artemisinins have been registered, the latter probably due to the limited use, in developing countries, due to its cost. [54]
Although vaccines against malaria are not yet available, research is still ongoing in order to find one. Several vaccines are currently under trials, like RTS,S, approved by European regulators in 2015 and under pilot trials in 2016. [39] Some vaccines ad-

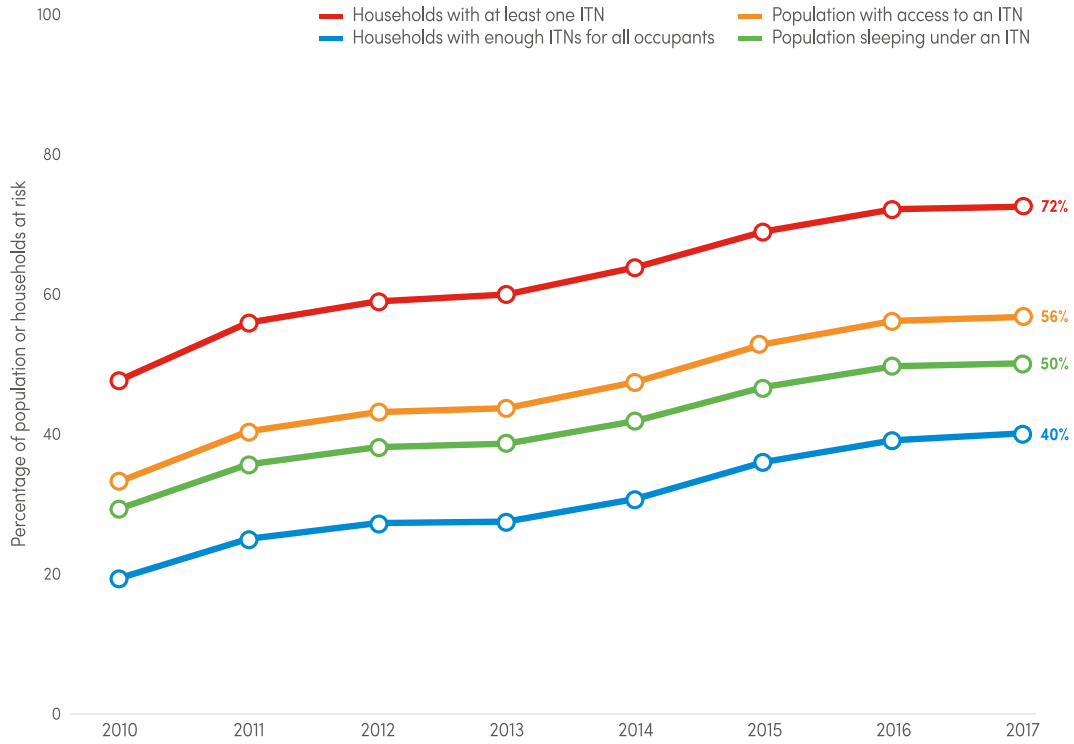

Figure 1.10: *Percentage of population protected by ITN. [1]*

minister a dose of *Plasmodium* (equivalent to a thousand bites of infected mosquitoes) made non-infectious by means of X-rays in order to stimulate the production of antibodies in the patient. [55]
Other vaccines, instead, more focused on avoiding the spread of the disease, directly administer antibodies to the patient, preventing the development of the parasite in the mosquito. [56] Vaccines aiming to target parasite in its blood stage have been proved to be insufficiently effective. [57]

1.3 Diagnosis

Prompt and effective diagnosis tools greatly help reducing the unnecessary use of antimalarial drugs, their associated side-effects and economic losses and the rapid emergence and spread of drug resistance. [1]
Clinical diagnosis, i.e. based only on symptoms evaluation, mostly used in the past, represent the cheapest strategy. However, due to the non-specific nature of the symptoms, it is often difficult to discern between from a simple fever or other diseases. In endemic regions this clinical practice lead to the preventive treatment of every kind of fever with antimalarial drugs. Evidence of this practice and its trend in the last years are shown in Figure 1.13. Clearly visible (green line) is the tendency to overuse, in the past and specially in endemic regions like Africa, antimalarial medications for the treatment of patients actually not affected by malaria due to the extensive practice of simple symptoms evaluation without the use of diagnostic tests (ACT:test ratio >1). From 2011 the trend started to decrease, reaching a value of ACT:test ratio equal or lower than one from 2015, result of an increased use, availability and trust in diagnos-

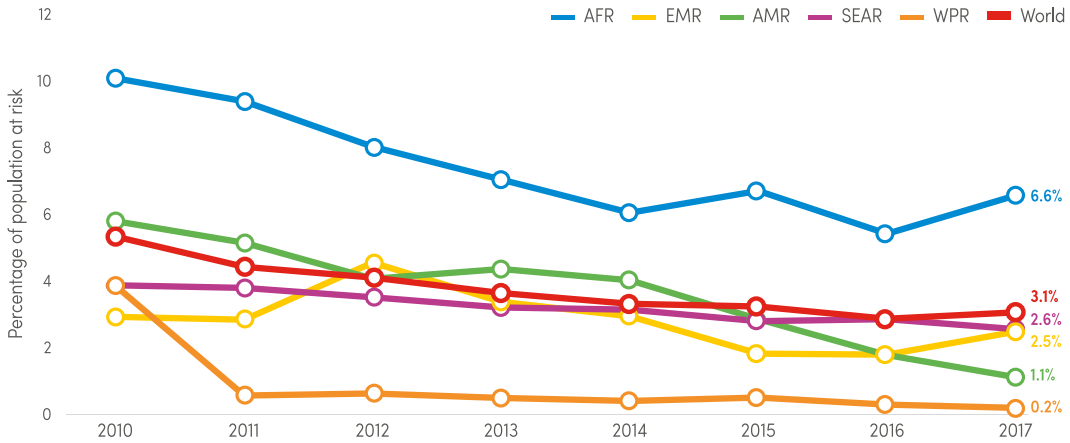

Figure 1.11: *Percentage of population protected by IRS. [1]*

tic tests results. The optimum point the green curve seems to aim asymptotically in the future years is represented by the blue line, i.e. antimalarial treatments are delivered only to positive patients assessed by diagnostic tests. Thus, in order to reach the aforementioned optimum, the following efforts have been and will be put in place to:

- Increase the sensitivity;
- Increase the reliability;
- Increase ease of use;
- Increase the accessibility and diffusion;
- decrease the costs;

of the current and new diagnostic tools. The conventional methods used for malaria diagnosis are microscopy using blood smears, Rapid diagnostic tests (RTDs) and Polymerase Chain Reaction (PCR). Currently there are several approaches under development; some are just an upgrade of conventional tests, others exploiting different physical properties such as fluorescence, dielectrophoresis, vapor nano-bubbles and magnetism. [58], [59], [60] Further in this section, both the actually used and future diagnostic tests will be shown.

1.3.1 Microscopy

Microscopic examination, thus the analysis of a blood droplet on a microscope slide through a microscope, represents the gold standard in malaria diagnosis. There are two techniques that mainly belong to this category: thin and thick blood smears. In both cases, blood needs to be collected, if possible, near a feverish attack and before administration of antimalarials. After being collected the sample should be processed within three hours otherwise shape changes or cells lysis may take place. The whole blood is mixed with heparin or EDTA anticoagulants to prevent clots formation. In Figure 1.14 a graphic representation of the thin and thick blood smear procedure is shown. In the case of thin blood smear analysis, after the aforementioned preliminary step, a droplet of blood is poured on a microscope slide. Another slide edge, held at a 45°, is

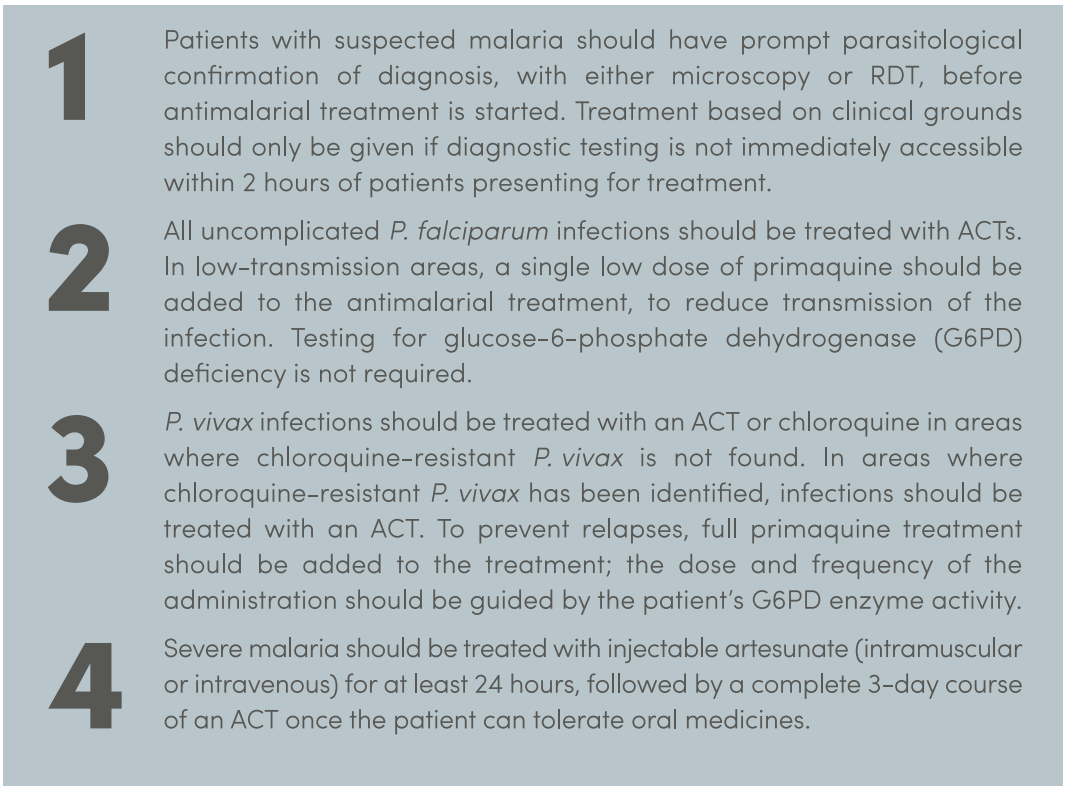

Figure 1.12: *World Health Organization treatment guidelines. [1]*

used to smear the droplet on the first slide in order to obtain a single layer of RBCs. Then, the sample is dried, fixed with methanol (100% or absolute for 15-30 seconds) and coloured. The latter is used to colour the blood cells and particles, GIEMSA or Wright's of Field's stains are usually used for the purpose. [62] Finally, for the analysis, 25 different fields of view are examined and the diagnosis is performed counting the number of iRBCs found. Sometimes only 10 fields are examined if the number of iRBCs in those fields is statistically relevant. Concerning the thick blood smear, a blood droplet is poured on a glass slide and then spread on it forming a 1 cm circle using the corner of another slide, taking care not make the preparation too thick. The sample is then let to dry without fixative. The dried blood sample is then coloured immersing it into GIEMSA staining for 20 minutes and washed rinsing it in deionized water for 3 minutes. The slide is then placed in vertical position and dried with air. [63] In this case the number of areas investigated under the microscope are only the ones needed to count about 200 white blood cells (WBCs), as the parasitaemia, in this technique, is expressed as a function of the WBC number. Microscopy is an common and relatively simple technique familiar to most clinicians. Due to the required equipment, laboratories that perform routine haematology analysis have the skills, tools and reagents to perform and evaluate blood smears. [64] The aforementioned techniques allow both to asses malaria infection, Plasmodium specie and quantify the amount of red blood cells infected. Thin film allows a facilitate species identification as Plasmodium appearance is best preserved. Thick film, however, screening a larger volume of blood is more sensitive than its counterpart allowing to detect slight infections. Thus, given the

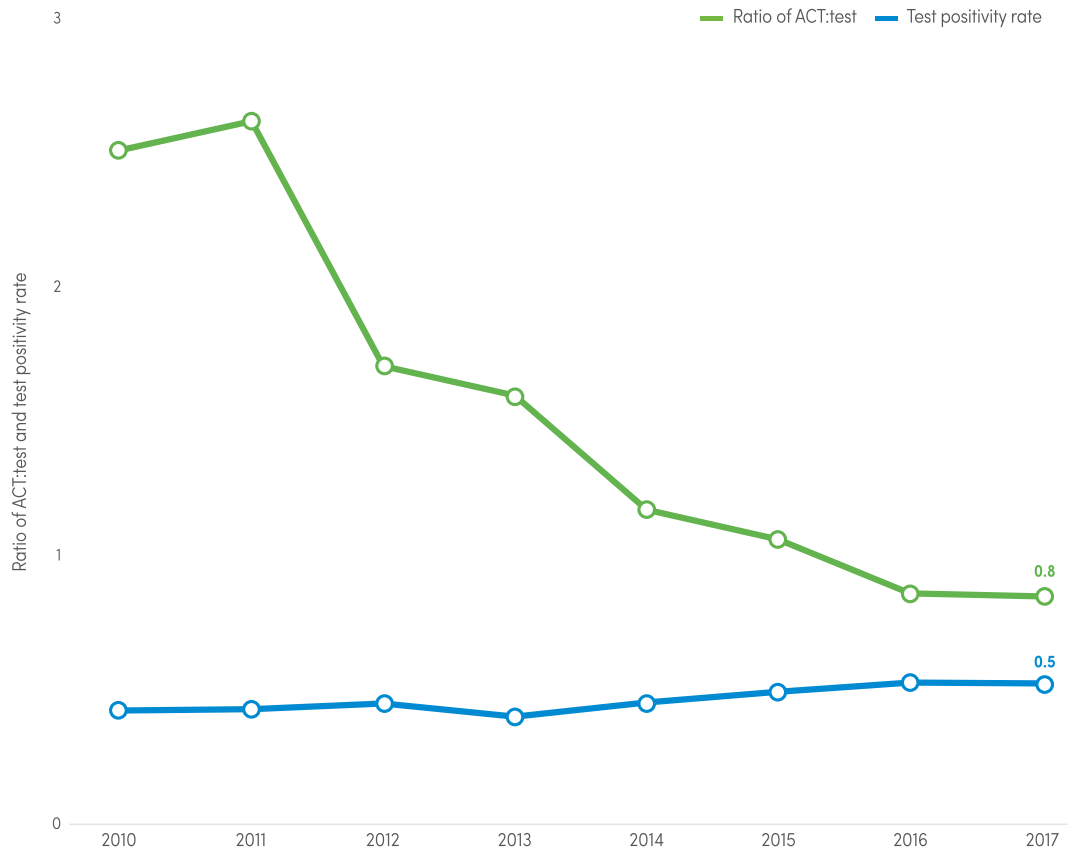

Figure 1.13: *Ratio between ACT treatment delivered to diagnostic tests performed and positive test rate in Africa. [1]*

complementary information of the two techniques, malaria diagnostic guidelines recommend to perform both in order to obtain a complete clinical picture. [62] Microscopy result, however, strongly depends on microscopist experience as well as on the laboratory equipment. Thus, to ensure diagnosis trustworthiness, several preventive and formative measures should be taken by the laboratories. Central coordinators for quality assurance, training systems, regular retraining and grading of competency, adequate budget and equipment. Thus, despite the cost of the personnel, glass slide and reagents required for microscopy examination mai seem negligible, other cost indices should be taken into account. As a matter of fact microscope purchase, maintenance, training and refresher courses represent the main expense. [65] Moreover, the main drawback of this technique resides in the time needed for a single diagnosis, which is about 30-60 minutes. The limit of detection (LoD), as previously anticipated, strongly depends on the technician skill and it ranges between 5 and 100 parasites/μL. [58] Despite being considered the gold standard for malaria diagnostic, the time and equipment required to perform it place severe limitations for population coverage in endemic countries. That is why others methods emerged in the last years: some are just an upgrade of already existing microscopy test which automate smear preparation, staining or slide-reading [66], [67]; others provide a completely different approach.
Among the formers, fluorochrome staining represents a more sensitive, rapid and easier to use alternative to GIEMSA staining. However, the mercury vapour fluorescence mi-

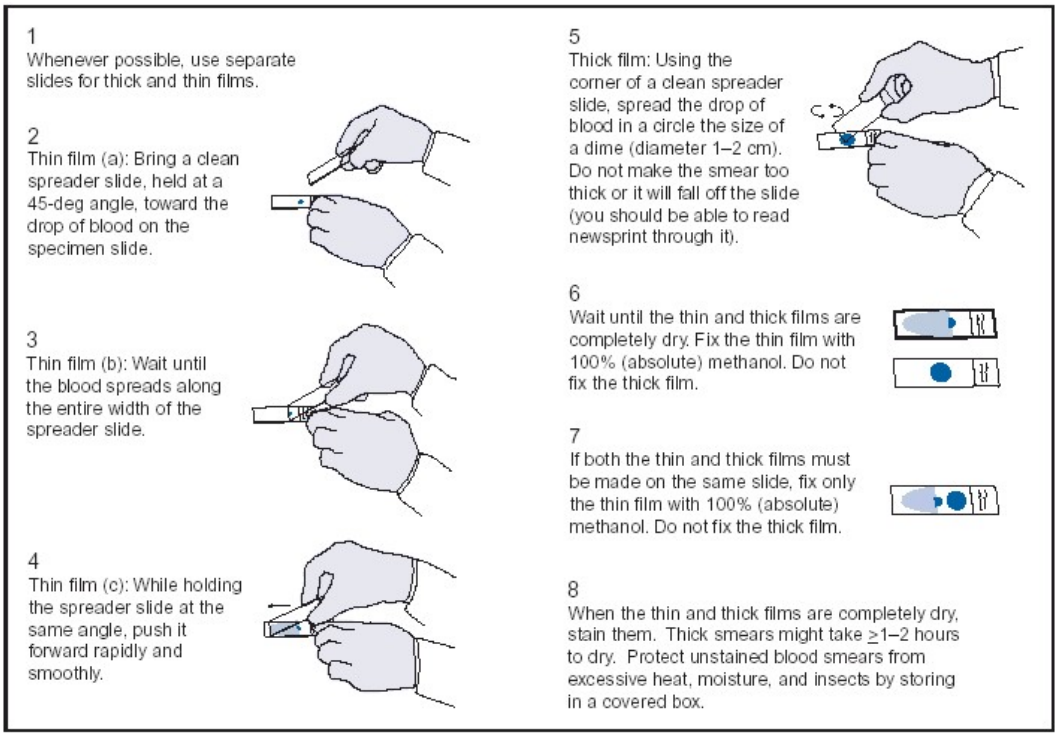

Figure 1.14: *Preparation of thin and thick blood films. [61]*

croscopes required are far more expensive. Fluorescence microscopy with a standard light microscope with an interference filter specifically designed for acridine orange fluorochrome has been successfully used for both thick and thin blood films. In this system two fluorescence colours, green for nuclei and red for cytoplasm, were emitted from stained parasites. This system actually helps the identification of parasites leading to a sensitivity around 90% even for low values of parasitaemia (100 parasites/μL). Despite the easier detection allowed an the increased reliability of the diagnosis, the slight dependence of the results on the microscopist and the time needed to be performed remain an issue.

1.3.2 Rapid Diagnostic Tests

Rapid diagnostic tests (RDTs) are able to diagnose malaria detecting the presence of Plasmodium antigens in human blood with a limit of detection around 200 parasites/μl. [1] RDTs represent an extremely easy to use and rapid diagnostic method for malaria. Their use is recommended particularly in remote areas where experienced technicians in performing microscopy examination are not available or there is no access microscopy services. RDTs are furthermore compact, disposable and their result-to-interpret. They exploit antibodies, i.e specific proteins produced by malaria parasites on its cellular membrane, to trap malaria specific antigens. RDTs are able to discern a single specie (P. falciparum or P. vivax) or distinguish between one and the others (P. malariae and P. ovale). [1], [58] RDTs based on lateral flow immuno-chromatographic antigen-detection. They rely on the binding interaction between a treated-membrane, covered by proper free labelled antibodies (for example HRP-II for P. falciparum), and

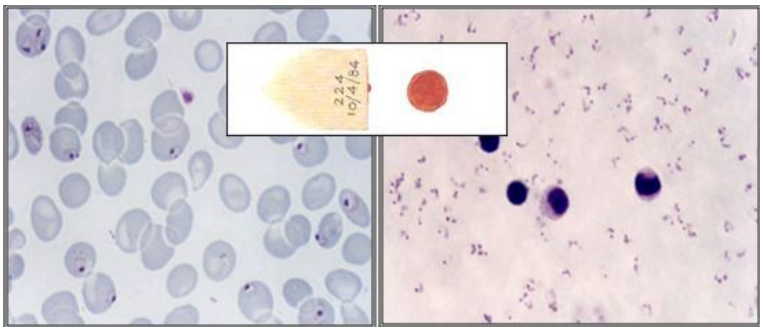

Figure 1.15: *Microscopy images of thin (left) and thick (right) blood smear. [61]*

the Plasmodium antigens in the patient's blood. The sample volume needed for the test is usually of about tens microlitres which can be obtained from a finger-prick. As the antigens are exposed on the cellular membrane of WBCs, the sample is mixed with a lysing agent which causes the rupture of the WBCs cellular membrane thus releasing antigens. During the test, the sample flows through the so-called RDT cassette (see Figure 1.16), thanks to capillary forces, binding to free labelled antibodies. If antigens are present in the sample, labelled antibody-antigen complexes are formed on the test line which is covered by antibodies immobilized at the test line, thus creating a coloured line given by the labelled antibodies. In order to assess the working condition of the test, another control-line is present. RDTs diagnosis times usually lies between 15 and 30 minutes. A comparison carried out between microscopy examination and Rapid di-

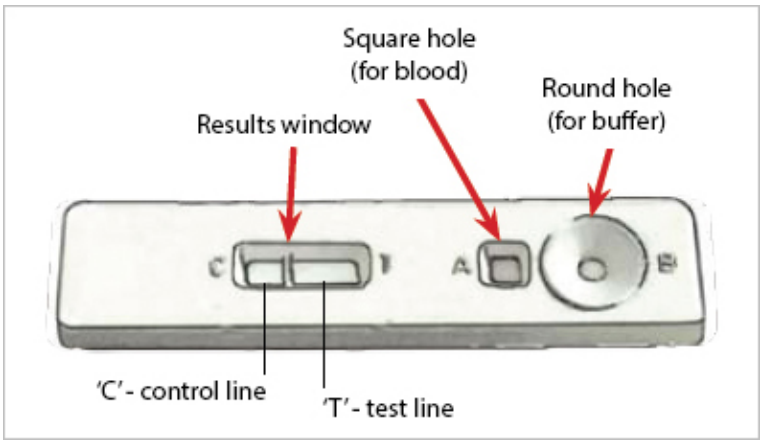

Figure 1.16: *Graphical representation of an RDT. [68]*

agnostic tests pointed out significant differences [69]. For the former case, a specificity of 81% and a sensitivity of 55% have been obtained while, 89% and 83% respectively for the latter one. Several reviews also specifically tested RDTs key performance indices throughout the years [58]. Even in these cases a sensitivity and specificity value greater than 90% have been attested. Following said results, RDTs proved their capability to provide an accurate diagnosis without the need of dedicated equipment or long processing times. Those features allowed RDT testing to significantly spread in endemic countries. According to WHO, in 2017, more than 270 million RTDs have been sold worldwide. [1] Most of them (66%) have been acquired by sub-Saharan African

region as an estimated 75% of malaria diagnosis have been performed using RDTs, a 20% growing figure since 2010. [58, 64] Despite the differences among the more than 200 different malaria RDTs available, the working principle, the execution time and key performace indices are similar. However, the main drawback of this technique resides in the working principle itself, i.e. te detection of plasmodium antigens. As a matter of facts, antigens persist in the blood stream of a patients for months after healing from the disease. This aspect prevents, not only the use of RDTs for a follow-up monitoring of the treatment but it also cause an high amount of false positives in endemic countries where the population is frequently exposed to plasmodium. Moreover, Plasmodium mutations, i.e. shifts in its genetic heritage, may bring a change in the antigens expression such that false negatives can occur. The limit of detection too is not enough to detect early stages of the disease and, on the contrary, high concentration of antigens may give rise to false negatives due to the "prozone" effect (i.e. an excess of antigen). [70] Moreover RDTs are at risk of deterioration and reduced sensitivity when exposed to heat and humidity for prolonged periods: their stability is assured at 4-40°C for 18-24 months. [58] Finally, RDTs, not offering a quantitative diagnosis, are often use in combination with other techniques to assess the severity of illness. Several efforts are under way to improve existing RDTs technologies such as urine-based malaria rapid test.

1.3.3 Polymerase Chain Reaction based methods

Polymerase Chain Reaction (PCR) based methods are based on the detection of the parasite genes (DNA/RNA) in a blood sample. The technique offers an highly sensitive diagnosis, being able to detect nucleic acid in minute quantities (i.e. a single molecule in a specimen) and, as a result, have revolutionized diagnostic medicine in many fields. With respect to malaria, several highly sensitive techniques for detecting the nucleic acid of the malaria parasite have been developed: the following discussion focuses on polymerase chain reaction and loop-mediated isothermal amplification (LAMP). PCR based tests detect malaria parasites in a blood sample by multiplying the nucleic acid present in the sample. This process, called amplification, is accomplished through the use of special reagents that catalyse gene replication and through precise control of the environment in order to create favourable conditions for the reactions (see Figure 1.17). In one cycle of PCR, it is theoretically possible to double the amount of target gene present; the cycle is typically repeated several times to produce large quantities (e.g. millions of copies) of the target gene. The product of this amplification process is then analysed for the presence of malaria using a variety of detection methods. PCR is able to detect extremely low parasite densities, generally surpassing microscopic and antigen detection methods in sensitivity and specificity. With regard to LoD, PCR can detect as few as 1 parasite/μL of blood (using a finger-prick sample) as compared to 50-100 parasites/μL for microscopy or RDTs. Using higher volumes of blood (e.g. venous-blood rather than finger-prick), researchers have developed ultrasensitive PCR with a LoD of 22 parasites/mL. [72] Generally, PCR requires a very well-equipped laboratory and technicians trained in molecular biology. In addition to the upfront investment in laboratory infrastructure, equipment and training for technicians, PCR is also several times more expensive on a per test basis than microscopy and RDTs. [73] As a result, malaria PCR is used for research, epidemiological surveys and as a reference standard

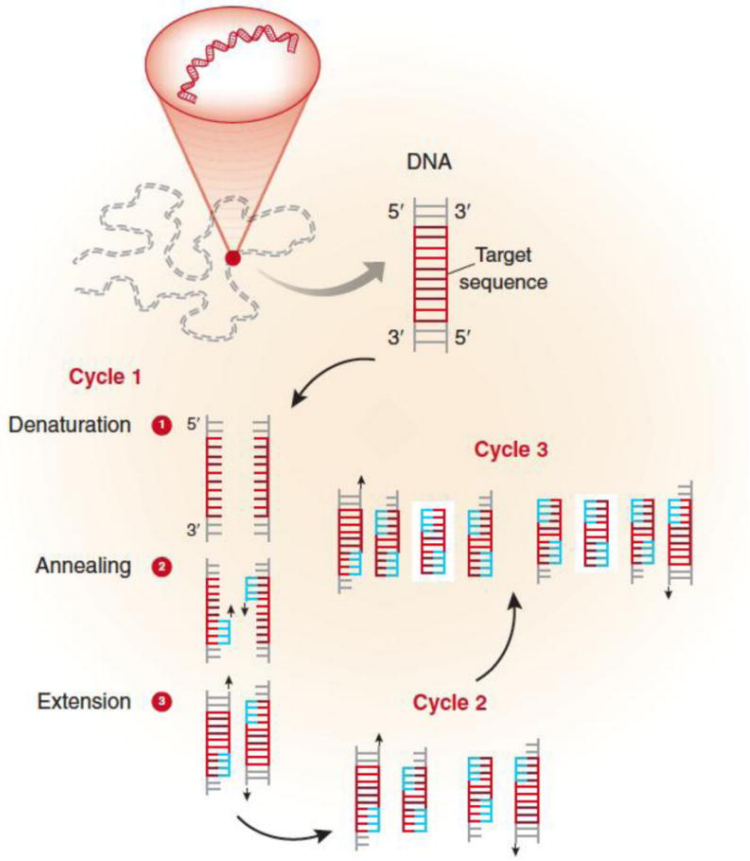

Figure 1.17: *Steps of PCR: (1) the DNA template is heated to 94°C and this breaks the weak hydrogen bonds that hold DNA strands together in a helix, allowing the strands to separate creating single stranded DNA. (2) The mixture is cooled to anywhere from 50-70°C. This allows the primers to anneal to their complementary sequence in the template DNA. (3) The reaction is then heated to 72°C, the optimal temperature for DNA polymerase to act. DNA polymerase extends the primers, adding nucleotides onto the primer in a sequential manner, using the target DNA as a template. With one cycle, a single segment of double-stranded DNA template is amplified into two separate pieces of double-stranded DNA. These two pieces are then available for amplification in the next cycle. As the cycles are repeated, more and more copies are generated and the number of copies of the template is increased exponentially,. [71]*

against which other methods are evaluated. Even in facilities with PCR availability, it is generally not used to diagnose patients as the results are not immediately available to the clinician and it is expensive. Even so, PCR is sometimes used to investigate complex cases; for example, to establish species after diagnosis has been made with microscopy or RDT. There are three main types of malaria PCR: conventional PCR in which result is qualitative; nested PCR which uses two rounds of amplification both for pan-malaria genes or specific gene; and real-time PCR that is the most commonly used method today due to its automation. On the other hand, there is LAMP approach: it is a recent diagnostic test which uses isothermal DNA amplification technology, whereby parasite DNA is amplified at a stable temperature and the by-products of amplification are detected based on changes in turbidity or emission of a fluorescent signal. The LAMP procedure begins with a sample preparation step to extract DNA, followed by amplification and detection of DNA through reaction at a constant temperature using

simple instruments such as water bath. During the process, large quantities of DNA are amplified, enabling simpler end-point detection as compared to PCR methods. In addition, the DNA sequences are amplified in such a way that the products fold into a looped structure causing the reaction mixture to appear turbid. Following amplification, detection is conducted through various methods, including visual, by using a fluorescent dye and UV light to enhance visual detection, or through the use of an instrument to measure turbidity. Recent works suggest that LAMP can achieve sensitivity and specificity comparable to PCR and well above RDTs and microscopy. Despite the advantages and high resolution seen, these nucleic acid detection methods present several factors that limit their use: high cost and sophisticated infrastructure needed, the lack of standardization methods and also limited availability of skilled technicians. Moreover, even if this problem is reduced with LAMP, a lot of time per sample is requested every time. [72], [58] Last but not least, these tests are not always quantitative. In the past years, among the principal efforts, there's the simplification of sample preparation (i.e. purification of DNA away from other sample components), the standardization of procedures and the attempt to reduce costs. By the way, it remains clear the fact that this approach, as far as accurate, remains entrusted to laboratories and not to endemic regions.

1.3.4 Serology and spectroscopy

Here we briefly analyse two uncommon techniques which, anyway, represent an interesting different point of view. Malaria serology refers to the use of antigens to detect malaria antibodies, which are a marker of malaria presence, as seen with RDTs. Although initially developed as a diagnostic test, nowadays they are not used any more to detect malaria for two reasons: first, it is not possible to distinguish between current and past infections; secondly, malaria parasites antibodies are not present during the acute phase of an infection, but they appear several days later. Serology tests for malaria are, however, used to detect exposure to malaria, because malaria antibodies parasites remain in the body long after an infection has been cleared. [58] In particular three main applications have been found about this [68]:

- screening blood donors involved in cases of transfusion-induced malaria when the donor's parasitemia may be below the detectable level of blood film examination;
- testing a patient, usually from an endemic area, who has had repeated or chronic malaria infections;
- testing a patient who has been recently treated for malaria but in whom the diagnosis is questioned.

Spectroscopy involves the absorption of particular wavelengths of electromagnetic radiation by molecules in a sample. The unique way through which molecules interact with light is used to classify and characterize the sample. Depending on the source exploited, different types of spectroscopy can be done resulting in different information. There are no platforms that currently use spectroscopic approach, but some of them are in development stage. [58]

1.3.5 Hemozoin based methods

As seen in section 1.1.2, malaria parasites produce hemozoin crystals (HCs), because they are not able to use the iron containing part of haemoglobin. Even though hemozoin was discovered and linked to malaria in the 1800s [58], however, it has not been used to diagnose malaria. While it is possible to see hemozoin in certain stages of the parasite's life cycle using microscopy, it is not always detectable with the traditional microscopy. Although the technologies under development differ in the approach, the methods shown in this section exploit two of the main physical properties of HCs: dichroism and magnetism. The former case take advantage of the way in which HCs interact with light, as described by a direction-dependent refractive index; the latter one, instead, exploit the magnetization due to unpaired electrons of Fe3+ atoms. Most of the hemozoin-based tests are designed to be hand-held devices that only use finger-prick blood sample. These kind of tests are usually very fast compared to the previous one, giving the results in about 5 to 10 minutes. [58] Moreover, as it follows by WHO statement [1], these new technologies can be suitable in endemic regions where infrastructures and well trained personnel are missing. Even if the target used to diagnose malaria here is always hemozoin, there are several technologies with many different performances. Magneto-optical technology (MOT): this test involves applying a magnetic field to the sample, causing alignment of any hemozoin crystals present. Then the device employs polarized laser to compare the transmittance of light before and after application of the magnetic field to the sample. A photodetector measures the change in transmittance of light that would indicate the presence of hemozoin and a microprocessor interprets the change in light providing the result to the test operator. Time needed is just 1 minute, sensitivity is about 90% and the LoD, still high, attested at 100 parasites/μL. It is important to underline that before the analysis, the sample has to be mixed up with a lysing agent to disperd hemozoin. [58] Several techniques exploit paramagnetic properties not only of hemozoin itself, but also of host RBCs which can be attracted with an high gradient magnetic separation method (HGMS). [74] This approach was the same used to separate deoxyhemoglobin (paramagnetic) by healthy RBCs with magnetic beads in microfluidic systems. Another similar approach is represented by MACS (magnetic-activated cell sorting): superparamagnetic nanoparticles are coated with antibodies that can be attached to antigens typically expressed by targeted cells. After mixing the cells and the beads in a solution, they are mixed and transferred to a magnetic column. Now, cells attached to the magnetic nanoparticles stay on the column, while other cells, which are not expressing the antigen, flow through. It follows that the cells can be separated positively or negatively with respect to the particular antigen. [75] Then, others more complex and promising methods exist such as a magnetic resonance relaxometry system (MRR) or non invasive tests where blood sample is obviated, collecting information just through the skin. [58], [74]

1.4 Tid Mekii project

Tid Mekii is the name of "malaria" in the local African language of Mbalmayo, a small village of Cameroon where the first preclinical validation of the test has been carried out. The idea is to design a novel diagnostic test with the following prerequisites: compactness, low-cost, user-friendly, pan-plasmodic and, above all, more rapid and, at

least, as sensitive as gold standard microscopy.

In order to do that two physical principles are used: magnetophoretic separation and

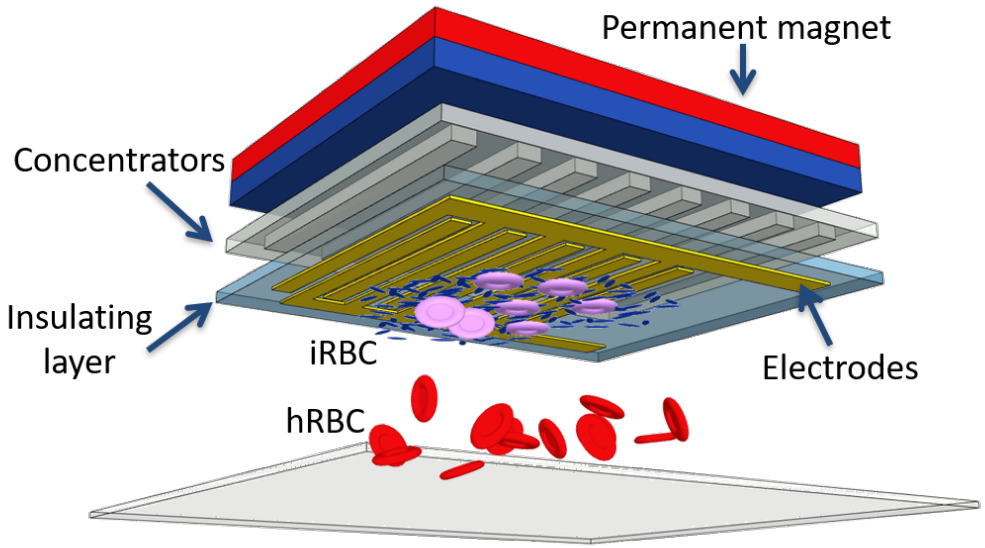

Figure 1.18: *Tid Mekii working principle and representative structure*

electrical impedance spectroscopy. As shownin Figure 1.18, magnetic field gradient ∇H is used to attract the target particles in specific areas where sensitive electrodes are placed such that a variation in resistance occurs. The targeted particles are iRBCs and hemozoin crystals. This is a lab-on-chip approach: so all the measurements are done thanks to a silicon chip in which nickel pillars are implanted and then, through a litoghraphy process, gold electrodes are deposited on top. After the blood sample is diluted with a solution made by phosphate buffered saline (PBS) and an anticoagulant (e.g. EDTA), it is placed in a PDMS gasket put in contact with the sensitive part of the chip. A magnetic force is provided, macroscopically, by permanent NdFeB magnets located on the back of the chip and, locally, by Ni pillars. The resulting total force allows the paramagnetic particles, i.e. HCs and iRBCs, to be attracted towards the sensitive areas of the chip, whereas the other ones sediment due to gravity force. The captured paramagnetic particles will then induce a variation in the electrical current, proportional to the number of particles, flowing between the electrodes. The current signal can be detected with an electronic system, composed by a trans-impedance amplifier and lock-in amplifier, and transferred to a computer where it is analysed with MATLAB software. The signal in Tid Mekii is proportional to the number of parasites, so it is quantitative and allows to perform the so-called "follow up", repeated checks along time in order to control the evolution of the disease and evaluate the drug response of the patient. It has to be underlined that this possibility is achieved thanks to the fact that in Tid Mekii, blood does not need to be treated with lysing agents with respect to the previous methods. There are still unexplored margins of growth for Tid Mekii, but all the improvements are oriented to satisfy the requirements stated by the World Health Organization in its guideline report "New Perspectives: Malaria Diagnosis" [76]:

- Compact, easy to use and low cost;
- Limit of Detection in the order of 10 parasites/μL such as gold standard;
- Aiming 100% of sensitivity for densities of >100 parasites/μL in all species;
- Reduced number of steps and test components;
- Reduced or suppressed time to perform the diagnosis (10 minutes);
- Develop methods that allow a quantification of parasite density.

In Table 1.1 an overview and comparison between the main diagnostic techniques for malaria and Tid Mekii is reported.

Technique	**Detectable parasite density (per μL)**	**Plasmodium species**	**Infection stage**	**Sensitivity**	**Cost (per test)**	**Operation time (per test)**
Microscopy	5-20, 50-100	All species	All stages	Gold standard	5000€ for a microscope, 0.12€-0.40€ per test	30-60 min
RDT	>100	All species	N/A	∼95%	∼1€	∼20min
PCR	<1	All species	All stages	90%	>100€	12-24h
Magnetophoretic methods	N/A	P. Vivax, P. Malariae	N/A	∼25%	<0.1€	6-12h
Tid Mekii	∼10	All species	All stages	>90%	<10	5-10min

Table 1.1: *Recap of the state of art diagnostic techniques*

CHAPTER 2

Magnetophoresis

2.1 Magnetostatic

Every atom of a material owns a magnetic moment, thus a solid exhibit a magnetic permeability, μ, which is given by the average of every atom moment composing it. This property of the material is used to define the magnetization vector **M** which is defined as the magnetic moment per unit of volume. In vacuum, since there are no materials, magnetization is absent, the magnetic flux density **B** is given by::

$$\mathbf{B} = \mu_0 \mathbf{H} \tag{2.1}$$

where the constant $\mu_0 = 4\pi \cdot 10^{-7}$ H/m is the permeability of free space and **H** is the magnetic field intensity. It is clear that the two fields have the same direction and are proportional to each other; **B**, the magnetic flux density, is measured in Tesla T while **H**, the magnetic field intensity, in A/m. In a solid, however, it is necessary to introduce and consider also the magnetization of the material, thus, **B** and **H** does not necessarily share the same direction as shown in Equation 2.2

$$\mathbf{B} = \mu_0(\mathbf{H} + \mathbf{M}) \tag{2.2}$$

In case of a linear magnetic material, the magnetization **M** is proportional to **H** through the dimensionless constant χ, called magnetic susceptibility: **M** = χ**H**. Thus, Equation 2.2 can be expressed as:

$$\mathbf{B} = \mu_0(1 + \chi)\mathbf{H} = \mu_0\mu_r\mathbf{H} \tag{2.3}$$

where μ_r = 1 + χ is the relative permeability of the material. Depending on this constant, which describes the response of a material when immersed in an external magnetic field, all the materials can be divided in three main categories:

- *Diamagnetic*: this class of materials is characterized by a relative permeability smaller than 1, thus presenting a -1<χ<0. The material magnetization **M** weakly opposes to the external magnetic field, thus causing a repulsion from it. It can be seen as a response of the magnetic moment of the material which opposes to the applied magnetic field that caused it.
- *Paramagnetic*: in this case the magnetic susceptibility is positive but smaller than one. The magnetization has the same direction of the applied magnetic field causing it. This property arises by the presence of unpaired electrons such that the magnetic moment of the atoms is different from zero and opposite with respect to the diamagnetic case. Without an applied field, the magnetic moments will point randomly due to thermal agitation. The application of a magnetic field, instead, aligns all the magnetic moments the stronger is the applied field.
- *Ferromagnetic*: in this last case μ_r » 1, thus a strong magnetization and attraction between the material and the external magnetic field occurs. In particular, while in the prior cases magnetization was absent without the presence of an external magnetic field, ferromagnetic materials exhibit a permanent magnetization even without **H**. This is linked to the phenomenon of hysteresis typical of ferromagnets where is also evident the relationship between **H** and χ which it is not a linear and univocal function.

In this thesis, all the above mentioned class of materials are present. The macroscopic external magnetic field and the local magnetic field gradient are both created using ferromagnetic materials. HCs and infected RBCs (iRBCs) are paramagnetic while healty RBCs (hRBCs), white blood cells and platelets are diamagnetic.

2.2 Magnetophoretic attraction

The force exerted on a magnetic particle, assuming that the length scale over which the magnetic field varies is much bigger with respect to the size of the magnetic particle itself and that the magnetic susceptibility of the particle is linear, can be expressed as:

$$F_m = \frac{\mu_0}{2} V_p \Delta\chi_p \nabla |\mathbf{H}|^2(\mathbf{x}_c) \tag{2.4}$$

where V_p is the volume of the particle, $\Delta\chi = \chi_{particle} - \chi_{fluid}$ the difference between the magnetic susceptibility of the particle and the surrounding medium, and $\mathbf{H}(\mathbf{x}_c)$ represents the field in position $\mathbf{x}_c$ (i.e. center of the particle) considering the particle absent. As it can be noticed from Equation 2.4, to attract a particle magnetophoretically, it is not important the χ value of the particle itself, but its difference in respect to the surrounding medium. In particular the blood particles are suspended in the blood plasma, which has a χ_{plasma} = -8.97·10^{-6}. [77,78] This value is close to the one of PBS χ_{PBS}=-9.05·10^{-6} for a 150 mM solution [79], which will represent the surrounding medium in some early experiments carried out using Tid Mekii device. Moreover, as mentioned before in section 1.9, the magnetic properties of RBCs depends on their HCs content. Thus, depending on the stage of the disease (i.e. ring, thropozoite or schizont stage), these particles will assume the $\Delta\chi$ values listed in Table 2.1. MetHb treated RBCs (tRBCs) are red blood cells in which the haemoglobin is oxidized into methemoglobin

(metHb). This oxidized form exhibits magnetic properties similar to hemozoin since it goes through a phase transition achieving an unpaired electron configuration such that S=5/2, thus giving to the host RBC almost the same magnetic properties of an iRBC. This change can occur naturally but it can be also obtained through the use of oxidising drugs.

Looking at Equation 2.4 it is possible to notice that the only and most relevant parameter that can be tuned during the design phase is the magnetic field gradient $\nabla \mathbf{H}^2(\mathbf{x}_c)$. As a matter of fact, a particle is attracted (or repelled, if $\Delta\chi$<0) toward the space where the magnetic field density is higher, and the more the magnetic field density changes in space, the stronger is the force that the particle is subjected. Magnetic force, combined with others, has already been employed in biochips and microfuidic systems for blood particles sorting or separation. [80, 81] Even if a particle does not exhibit spontaneous magnetic properties, it can be labelled with magnetic micro- or nano-particles.

Table 2.1: *Net magnetic susceptibilities of hemozoin and RBCs with respect to PBS, [34–36, 77–79]*

Particle	$\Delta\chi(\cdot 10^{-6})$
Healty RBC	0.01
Ring RBC	0.82
Trophozoite RBC	0.91
Schizont RBC	1.82
MetHb treated RBC	3.9
Hemozoin crystals	320

However, in addition to magnetophoretic force, particle motion is influenced by many forces of different nature: viscous drag, gravity, buoyancy, thermal kinetics, particle-fluid interactions and inter-particle effects. For most magnetophoretic applications involving micrometric particles, the magnetic and viscous forces are dominant, and one can ignore all other effects. Thus only the first three aforementioned terms will be taken into account. [82] The gravity force F_g, linked to the mass of the particle, and the buoyancy force F_b, related to Archimedes's principle share the same direction perpendicular to the floor, however, their effects are opposite, such that the net contribute is:

$$F_{g-b} = \frac{4}{3}\pi r_p^3(\rho_p - \rho_{fluid})\mathbf{g} \tag{2.5}$$

where ρ_p and ρ_{fluid} are, respectively, the density of the particle and the fluid, r_p the radius of the particle (in the assumption of spherical particle) and **g** is the gravity acceleration. [82]

Regarding the drag force F_{drag} since the corpuscles dimensions are bigger than 10 nm, it is possible to avoid discrete considerations within fluid analysis, such that both fluid and particles can be studied through Navier-Stokes equations. Assuming moreover a small Reynolds number Re « 1000 (i.e. Reynolds number quantifies how much the flow is turbulent) and that the fluids are incompressible, it comes out, for a particle with radius r_p:

$$F_{drag} = 6\pi\eta_{fluid} r_p(\mathbf{u} - \mathbf{v}) \tag{2.6}$$

where η_{fluid} is the fluid viscosity, **u** the velocity of the fluid while **v** the one of the particle. Due to the fact that in the device described in this thesis the fluid does not

move, it follows that **u** = 0, leading equation 2.6 to:

$$F_{drag} = -6\pi\eta_{fluid} r_p \mathbf{v} \tag{2.7}$$

from which is evident the classical viscous contribute of F_{drag}, opposite and linearly proportional to the velocity of the particle. [82]
As anticipated at the beginning of this section, other second order terms are involved in the motion of the particle: one of them is related to the thermal kinetics, which gives rise to a random motion said Brownian motion. This term can be analytically expressed through a diffusion coefficient D that, according to Stokes-Einstein equation, for a spherical particle is:

$$D = \frac{k_B T}{6\pi\eta_{fluid} r_p} \tag{2.8}$$

where k_B = 1.38·10^{-23} J/K is the Boltzmann constant and T the absolute temperature (K). Using D it is possible to obtain the so-called diffusion length l_{diff} which represents the average distance explored in a time interval, t, by the particle considering only diffusion, and whose expression is:

$$l_{diff} = \sqrt{Dt} \tag{2.9}$$

So, the bigger l_{diff}, the bigger the contribution of the Brownian motion. Nevertheless, from previous numerical simulations, it was shown that the overall physics is not affected by this term (e.g. RBC within blood travels 150 nm each second, which should be compared to hundreds of microns of the microfluidic chamber).
Once the main force contributions have been identified, it is possible to write the motion equations.
Tid Mekii device can be used in different configurations. In this thesis two main configurations have been exploited. Depending on the angle of the chip, it is possible to make the capture easier or selective. In a first configuration the chip is positioned parallel to the ground plane and facing downwards (see Figure 2.1(A)). In this case the magetophoretic force must completely counteract the gravity force, partially compensated by the buoyancy one, and the drag force. This configuration is the one requiring the highest magnetophoretic force but it is also the most selective one. On the other hand, when the chip is positioned perpendicular to the ground (see Figure 2.1(B)) the magnetic force required to attract a particle is lower as it is only in contrast with the projection, along the direction perpendicular to the chip surface, of the drag force. However the particle sediment due to gravity force with a certain speed, thus the magnetic force should be strong enough to attract it before it completely sediments going out of the capture region of the chip. The resulting motion equation for the case depicted in Figure 2.1(A) is:

$$\frac{\mu_0}{2} V_p \Delta\chi_p \nabla \mathbf{H}^2(\mathbf{x}_c) - V_p(\rho_p - \rho_{fluid})\mathbf{g} - 6\pi\eta_{fluid} r_p \mathbf{v} = \rho_p V_p \frac{d\mathbf{v}}{dt} \tag{2.10}$$

Grouping some terms, Equation 2.10 can be recognized as the one of an accelerated motion inside a viscous medium with a time constant needed to reach a steady state equal toτ=($\rho_p V_p$)/($6\pi\eta_{fluid} r_p$). Due to the short distance that particles have to travel before reaching the chip surface (i.e. few tens of micrometers), $\nabla\mathbf{H}^2$ can be considered almost constant in the region of motion. Given this assumption and referring to the physical and morphological properties resumed in Table 2.2, τ results to be less than

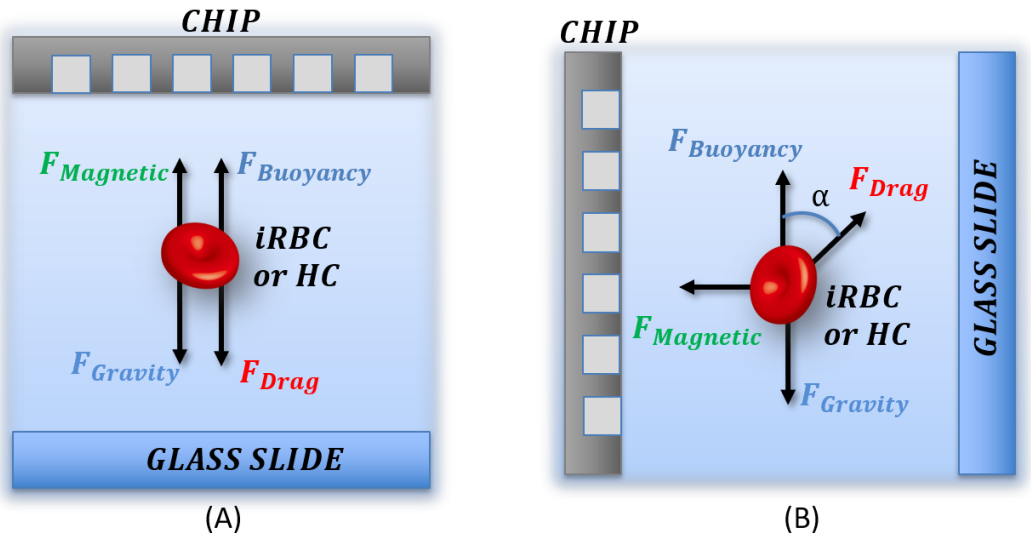

Figure 2.1: *Tid Mekii forces distribution depending on the configuration. (A) Horizontal configuration: The chip is placed facing downwards parallel to the ground and the gravity force is opposite in respect to the magnetophoretic one. (B) The chip is placed perpendicular to the ground and the gravity force is perpendicular to the magnetophoretic one.*

1μs, so a little time interval is sufficient to reach a steady state condition (i.e. uniform straight motion). Thus the particles can be considered having a constant speed $\mathbf{v}$ driven by the, approximately, constant magnetic force.
The steady state velocity can be obtained starting from equation 2.10, zeroing the right

Table 2.2: *Summary of physical and morphological properties of HCs, iRBCs and hRBCs.*

Property	HCs	iRBC	hRBC
Net susceptibility ($\Delta\chi$)	$320.72{\cdot}10^{-6}$	$1.8{\cdot}10^{-6}$	$0.01{\cdot}10^{-6}$
Radius (r)	0.18(μm)	2.78(μm)	2.78(μm)
Density (ρ_p)	1490(kg/m^3)	1125(kg/m^3)	1125(kg/m^3)

term and rearranging the remaining ones:

$$\mathbf{v} = \frac{\frac{\mu_0}{2} V_p \Delta\chi \nabla \mathbf{H}^2(\mathbf{x}_c) - V_p(\rho_p - \rho_{fluid})g}{6\pi\eta_{fluid} r_p} = \frac{2r_p^2}{9\eta_{fluid}} \left[\frac{\mu_0}{2}\delta\chi_p \nabla \mathbf{H}^2(\mathbf{x}_c) - (\rho_p - \rho_{fluid})\mathbf{g}\right] \tag{2.11}$$

In order to move towards the chip, $\mathbf{v}$ must be positive according to the reference system chosen, so the gradient of the squared magnetic field must satisfy the following condition:

$$\nabla \mathbf{H}^2(\mathbf{x}_c) > \left(\frac{2(\rho_p - \rho_{fluid})\mathbf{g}}{\mu_0 \Delta\chi_p}\right) \tag{2.12}$$

Thus, the fundamental physical quantities to determine the minimum gradient of magnetic field are the susceptibility of the particle in respect to the fluid it is immersed in and the difference between their densities. In Tid Mekii sample preparation, blood is diluted within a solution made of PBS and plasma, in order to achieve a 4% value of haematocrit HT. The mass densities of these two fluids are, respectively, 1.025 g/mL for

plasma and 1 g/mL for Dulbecco's PBS (1X), such that in both cases it can be assumed $\rho_{fluid} \approx 1$ g/mL. The values of $\Delta\chi_p$ are the one reported in 2.1. Knowing all these values, is possible to extract the minimum gradient of magnetic field needed to attract magnetic particles towards the chip. The results are reported in Table 2.3.

From Table 2.3, it is clear that hRBCs, since their $\Delta\chi_p$ is almost zero, require the

Table 2.3: *Minimum gradient of magnetic field values needed to attract particles towards the chip.*

Particle	Minimum $\nabla\mathbf{H}^2$ value (A^2/m^3)
hRBC	$1.56{\cdot}10^{17}$
Ring RBC	$1.9{\cdot}10^{15}$
Trophozoite RBC	$1.72{\cdot}10^{15}$
Schizont RBC	$8.6{\cdot}10^{14}$
metHb RBC	$4{\cdot}10^{14}$
HCs	$2.26{\cdot}10^{13}$

highest field gradient rather than the others. The strong difference of minimum $\delta\mathbf{H}^2$ required to attract health RBC and infected RBC gives the possibility to selectively attract only the infected one: this is the core idea of Tid Mekii device. Between these latter particles, by the way, there is a different $\nabla\mathbf{H}^2$ corresponding value, in term of order of magnitude, meaning that HCs and metHb will be, overall, more paramagnetic with respect to any iRBC stage.

2.3 Magnetic Design of the chip

It is now clear that the most important parameter to successfully capture the infected RBCs, and the only one it is possible to act on during the design phase is the magnetic field gradient $\nabla\mathbf{H}^2$. Thus, as showed in Section 2.2 the minimum required $\nabla\mathbf{H}^2$ should be greater than 10^{15} but lower than 10^{17} in order to avoid the capture of hRBC which will lead to false positive results.

In order to achieve magnetic separation, Tid Mekii exploits a two-levels approach: a macroscopic and approximately uniform $\nabla\mathbf{H}^2$ is provided by external permanent magnets, strong enough to attract iRBC at a distance of approximately 100 μm. A more localized gradient is provided by micrometric pillars made of Nickel embedded inside the silicon chip. The latter gradient is fundamental for a successful detection of the particle and in order to optimize the resolution. As it will be explained in detail in Section 3.2, the resistance variation, ΔR/R, caused by a particle captured between the detection electrodes is proportional to the ratio between the volume of the particle, V_p, and the volume of solution sensed by the electrodes V_{el}. The main purpose of the concentrators is therefore to concentrate the particles in the smallest possible area of the chip. Thus, if the particles are captured in few small spots on the chip, the electrodes can be put only in those areas, minimizing V_{el} and consequently increasing ΔR/R that in turn maximize the recorded signal, allowing to be able to measure a smaller parasitaemia.

In order to design and maximize both the macroscopic and microscopic magnetic field gradient, numerical simulations have been carried out using COMSOL Multiphysics 5.2. Concerning the macroscopic field, its main purpose is to generate the highest magnetic field gradient possible. Considering that the magnetic field decreases with the square of distance from it source, maximising $\mathbf{H}$ is then the first step in order to

increase the gradient. Thus the choice of the magnetic field source is relevant. Two common ways to generate strong magnetic fields are: electromagnet and permanent magnet. The former, however, in order to produce magnetic flux densities in the order of 1 T consumes a lot of power (even 200 W), have large dimensions (coil diameter 5-10 cm) and produces interferences that could affect the electrical detection. Permanent magnets on the other hands, are compact, does not consume any electrical power nor affect the measurement. Neodymium-Iron-Boron (NdFeB) are the strongest permanent magnets available on the market and they are given a grade depending on Residual Flux Density, i.e. the remaining magnetic field exerted by a material after the magnetizing field has been removed. For the purpose of this thesis the strongest magnets available from **K&J Magnetics, Inc.**, which are N42 grade have been deployed. However the gradient produced by those magnets alone it is not enough to capture iRBCs as it is well below $1 \cdot 10^{14}$ A^2/m^3. Thus, different magnets configurations have been simulated using COMSOL to increase the magnetic field gradient. The strongest gradient has been obtained with two N42 NdFeB magnets with parallelepiped shape (20x20x5mm^3) put in close contact to each other but with opposite magnetization, and interposing a 0.2 mm μ-metal sheet (i.e. a nickel-iron soft ferromagnetic alloy) between them as shown in Figure 2.2. The two magnets strongly repel each other, thus a custom press-like system

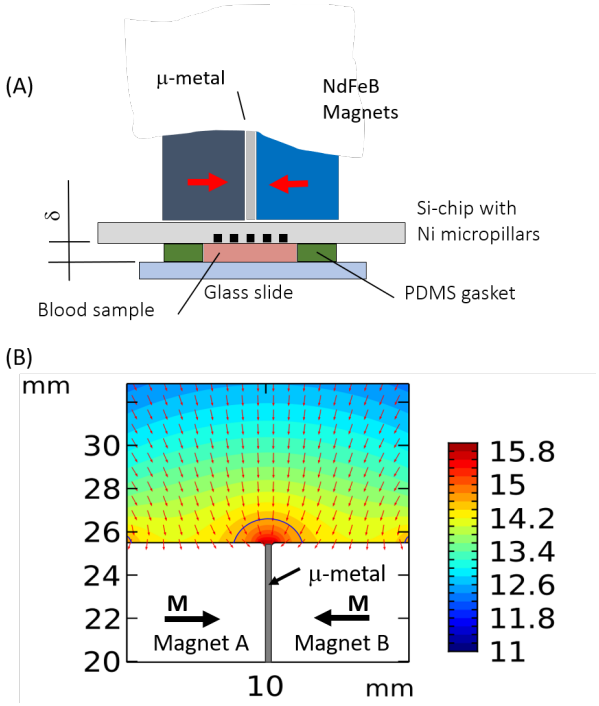

Figure 2.2: *Permanent magnets assembly. (A) Position of the permanent magnet in respect to the chip, (B) Numerical simulation using COMSOL of the assembly. The colour plot represents the intensity of the square of the magnetic field density in logarithmic scale while the blue line is the isoline defining the border between the capture and no capture of iRBCs. The red arrows represent the direction of* $\nabla \boldsymbol{H}^2$

has been fabricated to put and held them in position. The principle why the assembly works is simple: the magnetic field lines produced by the magnets are perfectly opposite and perpendicular to their face in the centre of the surfaces that are put in contact,

cancelling each other. However, moving out from the centre of said surfaces, the lines start to bend, acquiring a component parallel to the magnet surface that grows stronger as the distance from the centre increase. This parallel components sum each other, and are carried outside by the μ-metal sheet. The resulting magnetic field between the two magnets is almost doubled, going from 0.55 T for the single magnet to 0.98 T for the assembly. Moreover in this way all the magnetic field lines are focused in a smaller spot, i.e. along the line between the two magnets. Using this solution it is possible to successfully attract iRBC up to a distance of approximately 750 μm from the magnets. Concerning the microscopic magnetic field gradient, a possible solution, already successfully used in literature for similar applications [83–86], is to use micrometric elements made of ferromagnetic material. In order to understand how this solution is able to generate $\nabla\mathbf{H}^2$ it is useful to remember the relation between **B** and **H** from Equation 2.2. The application of an external uniform magnetic field H_0, like the magnetic field generated by a permanent magnet and such the one showed in Figure 2.3(A), cause the magnetization **M** of every material subjected to it. However, such magnetization generate itself a magnetic field, called demagnetizing field H_d, which, inside the material, is opposite to the magnetization vector. Indeed Equation 2.2 can be rewritten, making clear the two terms of **H**:

$$\mathbf{B} = \mu_0(\mathbf{H}_0 + \mathbf{H}_d + \mathbf{M}) \tag{2.13}$$

where H_d=-N**M** and N is the demagnetizing tensor which is connected to the geometry of the material. In Figure 2.3.B the demagnetizing field is shown and it is possible to note that outside the material the field lines have the same direction of H_0 near the faces of the solid perpendiculars to it, while they are opposite between the solids. Due to this concordance and discordance of the two fields composing **H**, they interact constructively and destructively in different areas of the space around the concentrators, thus creating areas with different magnetic field intensities which in turn create a magnetic field gradient as shown in Figure 2.3(C). It is now possible to notice that the stronger the magnetization of the material, the stronger will be $\mathbf{H}_d$. Consequently, in order to maximize $\nabla\mathbf{H}^2$ it is useful to select materials with high μ_r, like ferromagnetic materials. In this work of thesis, the magnetic microconcentrators have been fabricated in Nickel, which has a $\mu_r \approx 450$.
Different concentrators geometries and position have been simulated using COMSOL in order to maximize both $\nabla\mathbf{H}^2$ and the concentration factor. The latter, is defined as the ratio between the volume which every pillar is able to capture and the area in which it brings and concentrate the particles. As already mentioned in this section, this parameter is extremely important in order to have an higher resistance variation for every particle captured. The optimal geometry found consist in an hexagonal array of cylinders with an height of 20 μm while the choice of their optimal diameter and spacing will be decided trough practical capture experiments (see Section 2.5) . Some considerations about the role of those parameters are needed. Reducing the space between pillars brings to a more efficient attraction, however the concentration factor worsen as the number of capture spots increase while the capture volume decrease. Increasing the height of the pillars make it easier to magnetize the pillars due to the shape anisotropy, which makes easier to magnetize a solid along its longest axis, called easy axis. However micro-fabrication technological limitations arise (see Section 4.1). More than generating the macroscopic magnetic field gradient, the permanent magnets assembly, also

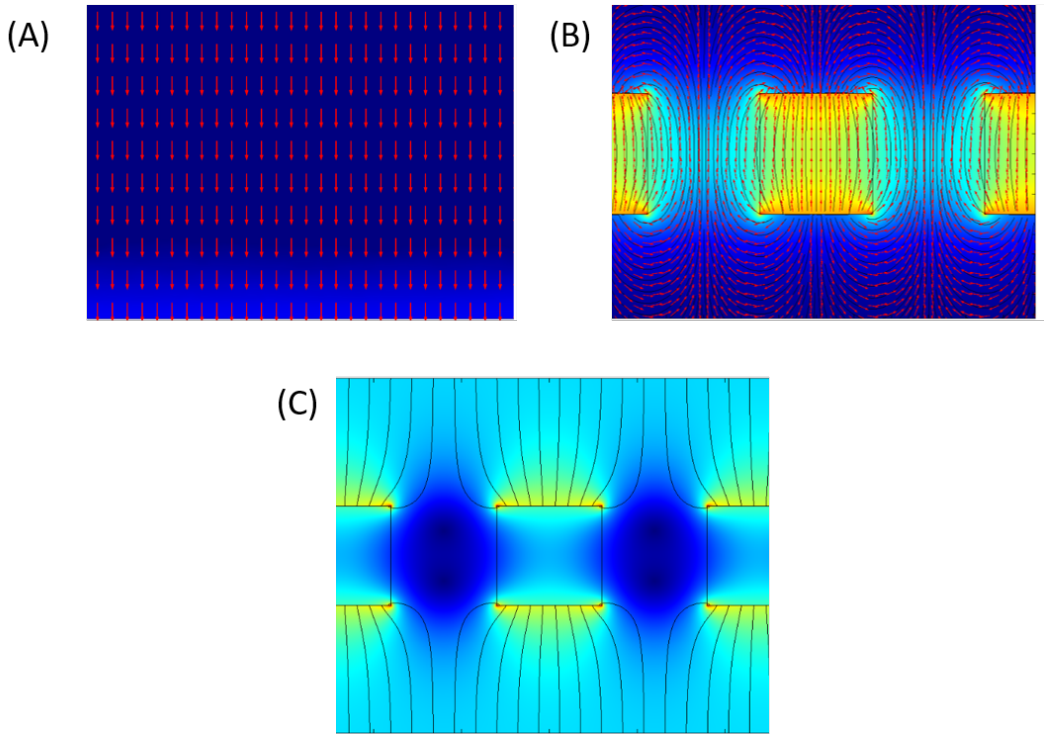

Figure 2.3: *Simulated working principle of the magnetic concentrators. (A) Uniform external magnetic field H_0, (B) Demagnetizing field $\boldsymbol{H}_d$ produced by the ferromagnetic material as a consequence of its magnetization caused by H_0, (C) Resulting magnetic field $\boldsymbol{H}$. The colour plots and arrows represent, respectively, the normalized intensity and direction of the different components of $\boldsymbol{H}$.*

represents the magnetic field source needed to magnetize the Ni pillars. Chips with different pillars spacing and diameter have been tested using tRBCs in order to assess the optimal configuration and the results of this activity are reported in the next section (Section 2.5).

2.4 Hemozoin - Electrical and magnetic properties

Hemozoin crystals are a well known malaria marker and also widely studied in order to better understand the behaviour of *Plasmodium* during its intra-erythrocytic stage, with the purpose of creating effective antimalarial drugs. However, electrical and magnetic properties of HCs are not well known and the studies are not always in agreement. Concerning the electrical properties of HCs, there are no studies reporting their electrical impedance in liquid except for some recent studies performed on Hemozoin crystals suspended in liquid [87] and cyclic voltammetry measurements. [88] As HCs can be also found free into the blood stream after the erythrocyte lysis, they can be attracted and sensed, as well as iRBCs, by Tid Mekii device. Thus it is useful to understand if they behave as an insulating or conductive particle. Regarding the magnetic properties, in particular magnetic susceptibility, there are few and not always in agreement results. In particular, two studies report a paramagnetic behaviour of HCs, measuring a susceptibility value $\mu_r \approx 3.2 \cdot 10^{-4}$ [34,35], while one one research group claims hemozoin to be superparamagnetic with μ_r in the order of 10^3, [30] thus seven order of magnitude

higher than the aforementioned studies.
In order to obtain a clear information about those properties, which are relevant both for a feasibility study and the design phase of the device, a preliminary study has been carried out in this thesis. [36] Tests have been performed using synthetic Hemozoin crystals, provided by Invivogen, which have the same size and properties of their natural counterpart. [89, 90]
In order to assess the electrical conductivity of hemozoin in DC, current sensing atomic force microscopy (CS-AFM) has been exploited. HCs have been dispersed on a silicon substrate covered by a 100 nm Au layer, thus making conductive its surface. For this purpose a Pt-Ir coated n-doped silicon by Applied NanoStructures Inc has been used. In order not to wear off the coating of the tip, some I-V curves have been performed in different points of the substrate, subsequently, the topography, of the same region where the I-V were taken, has been acquired. Doing so, it was also possible to associate to each I-V the corresponding topological spot where it was taken, either on an HC or on gold. The voltage applied to the tip during the I-V ranges from -10 V to +10V while the resulting current measured by the AFM trans-impedance amplifier connected to the gold-coated substrate. In Figure 2.4 both the topographical AFM scan of the gold surface, with some HCs deposited on top, and the graph reporting two I-Vs made both on gold and Hemozoin crystals, are shown. As can be seen from Figure 2.4(B), on gold, the current cause the saturation of the trans impedance amplifier (10nA) for every non null voltage value as expected from a conductive behaviour. On the other hand, when performed on HCs, the current recorded is lower than 10pA even for the maximum applied voltage. From this measurements a precise value of resistivity hemozoin can not be extracted due to the amplifier resolution. However, it is possible to assert that the resistance of gold lays below $10^5\Omega$, while the one of hemozoin above $10^{12}\Omega$. It can therefore be said that HC behaves like an insulator for DC frequencies. On the other hand, in order to measure the hemozoin behaviour at AC frequencies, in particular in the MHz range, the impedance change, caused by the sedimentation of HCs on the surface of some interdigitated electrodes has been measured. The interdigitated electrodes are 2 μm wide, with a 2 μm gap between them and a thickness of 100nm (see inset Figure 2.5(A)). As can be noticed from Figure 2.5(A), reporting the impedance spectrum of the aforementioned electrodes, from DC to MHz frequencies, the impedance is characterized by a capacitive behaviour, C_{dl}, while at higher frequencies, the resistance of the solution, R_{sol} become the dominant term. Due to the fact that C_{dl} is not sensitive to the presence of particles between the electrodes, the measurements have been performed at 3MHz in order to sense the resistance of the solution. For a more detailed explanation of the aforementioned impedance spectrum terms, see Section 3.1 and 3.2. Electrodes have been immersed in a Dulbecco's Phosphate Buffered Solution (1x), then a certain amount of HCs have been added to the solution and the resistance variation of the solution due to the sedimentation of Hemozoin on the electrodes has been recorded. In Figure 2.5(B), the normalized resistance variations, $\Delta R/R_0$, resulting from the sedimentation of three different HCs concentrations is shown. In particular the hemozoin concentrations are: C1= 0.01 mg/ml, C2= 0.03 mg/ml, C3= 0.06 mg/ml. As can be noticed, $\Delta R/R_0$ increases in time as the particles deposit on the electrodes and the variation is proportional to their concentration. This increase indicate that HCs have a resistivity higher than PBS, which is equal to 0.66 Ω·m. However, being such re-

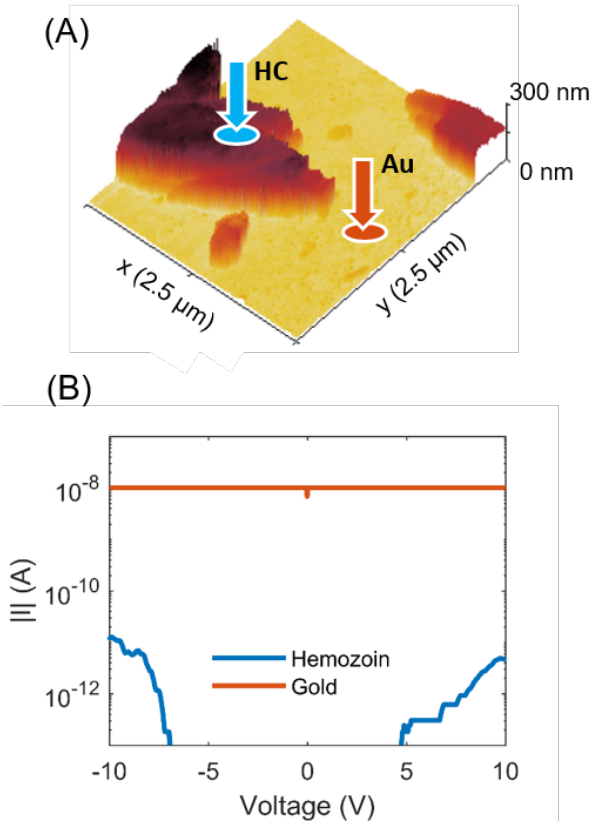

Figure 2.4: *CS-AFM scans performed to study HCs properties. (A) Topographical scan of a gold coated silicon substrate with HCs dispersed on it , (B) Electrical I-V sweeps on HC (blue line) and gold (red line).*

sistivity low it does not allow to determinate if the HCs are to consider as insulating particles. Therefore, a quantitative analysis has been performed. The volume fraction of the sensitive volume of the electrodes occupied by the particle has been estimated by means of microscopy images of the electrodes taken after the experiments for every concentration. In Figure 2.5 from (C) to (E), the aforementioned images for the concentration C1, C2, C3 respectively are shown. The volume fraction estimation has been used to calculate the expected $\Delta R/R_0$ with the equation: $\Delta R/R_0 = \frac{3}{2}\phi$, where ϕ is exactly the volume fraction. Said relation comes from the Maxwell's mixture theory, assuming the particle to be insulating (see Section 3.2). Thus, the experimental asymptotic signal values have been compared to the estimated one. The results are reported in Table 2.4. The agreement between experimental and theoretical values allows

Table 2.4: *Comparison between the experimental and theoretical $\Delta R/R_0$ variation depending on HCs concentration.*

HCs concentration (mg/ml)	Experimental $\Delta R/R_0$ (%)	Theoretical $\Delta R/R_0$ (%)
C1 =0.01	1.8±0.2	2.0±0.25
C2= 0.03	2.9±0.3	3.6±0.5
C3= 0.06	6.2±0.5	6.0±0.5

to conclude that HCs can be considered insulating particles even at MHz frequencies.

At last the magnetic properties of hemozoin, in particular its magnetic susceptibility

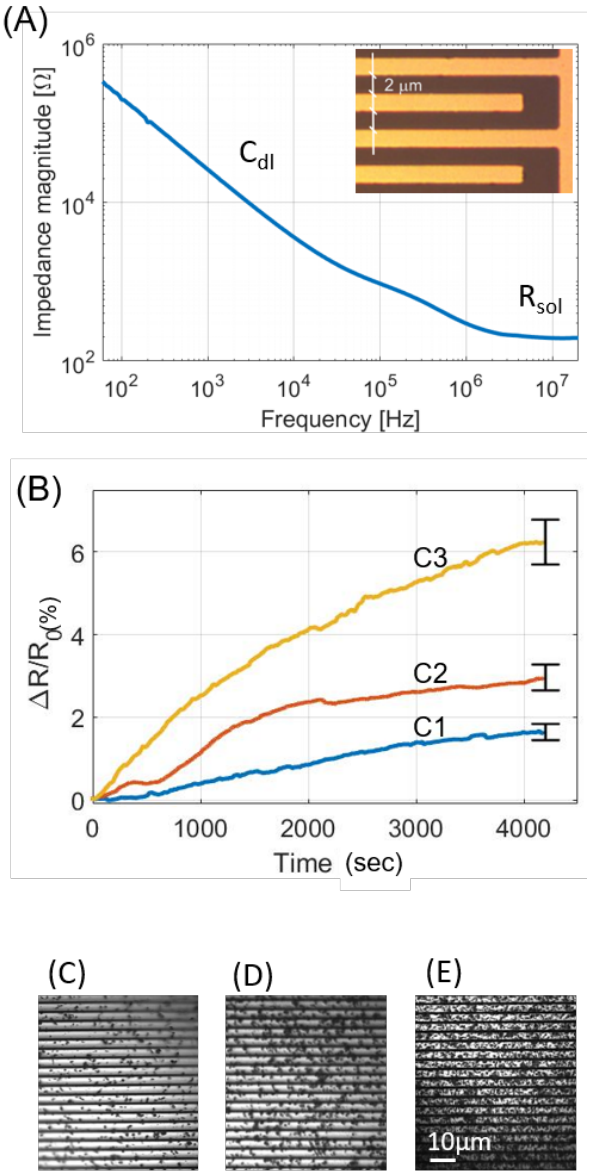

Figure 2.5: *(A) Electrical Impedance spectrum of the interdigitated electrodes used for the study of HCs electrical properties, the inset shows a microscopy image of said electrodes. (B) Normalized resistance variation $\Delta R/R_0$ caused by the sedimentation of hemozoin crystals on the electrodes surface. (C-E) Microscopy images of the HCs sediment on the electrodes at the end of the experiments for the concentration C1=0.01 mg/ml, C2=0.03 mg/ml, C3=0.06 mg/ml respectively.*

value and magnetization curve have been measured through a Vibrating Sample Magnetometer (VSM). For these tests, two hemozoin samples of 3.3±0.2 g have been used undiluted, as shipped from the supplier. In Figure 2.6(A) the magnetization curve, obtained sweeping the external magnetic field from -1.5 T to 1.5 T, of HCs is reported. In order to obtain the aforementioned graph, a normalization has been done in order to obtain the magnetization **M** starting from the raw data coming from the instrument, i.e. magnetic moment. In order to estimate the volume, starting from the mass of HCs, a

density value of 1.49 g/cm^3 has been considered. The positive slope and linearity of the curve are indicators of a paramagnetic or superparamagnetic property. However the susceptibility $\chi = \mathbf{M}/\mathbf{H}$ is equal to $3.5\pm0.2\cdot10^{-4}$ for the first sample of hemozoin and $4.7\pm0.4\cdot10^{-4}$ for the second one. Thus giving an average χ $\approx4.1\cdot10^{-4}$. This value clearly points to a paramagnetic behaviour of HCs (superparamagnetic particles have $\chi > 1$) and it is in agreement with the value found by [34, 35] equal to $3.2\cdot10^{-4}$, which is seven order of magnitude lower than the one reported by [30]. In order to further

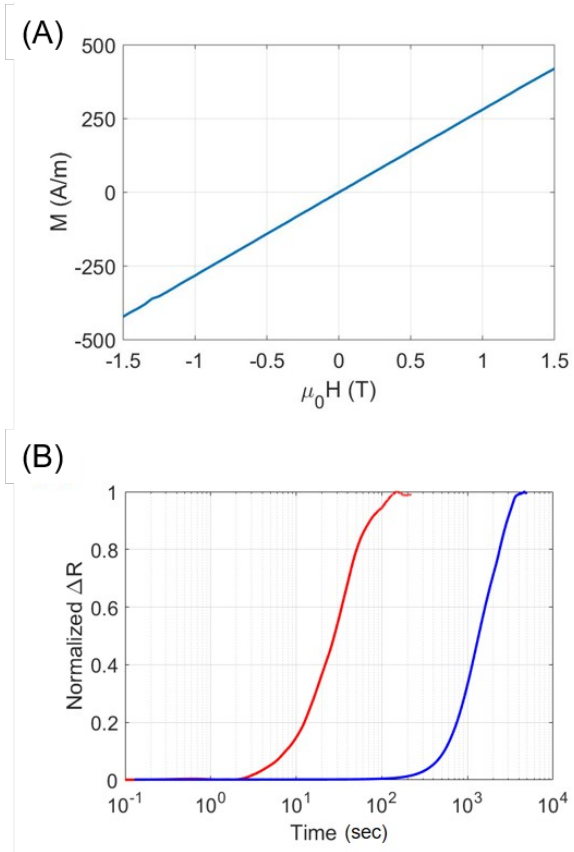

Figure 2.6: *(A) Magnetization curve of synthetic hemozoin obtained from a VSM measurement, (B) Resistance variation caused by the attraction of superparamagnetic beads (red line) and HCs (blue line) on the electrodes surface as a function of time.*

confirm the result obtained, the same approach used for the measurement of the electrical properties of HCs in AC frequencies has been exploited. However, this time the particles have not been left to settle down on the electrodes thanks to the gravity force, but attracted on said surface through a magnet positioned behind the chip. In this test two different particles have been considered: HCs and superparamagnetic beads with 1 μm radius (Dynabeads MyOne Carboxylic Acid), whose $\chi\approx1$. Given the measurement setup, the particles are expected to sediment onto the electrodes due to two forces: the gravity force and the magnetophoretic force. The latter exerted by the magnet on the particle (see Section 2.2). A first approximation of the force acting on the particles, F_p, in the aforementioned configuration is given by the simplified balance of forces:

$$F_p = (\rho_p - \rho_f) \cdot V_p g + \frac{1}{2}\mu_0 V_p \Delta\chi \nabla \mathbf{H}^2 \tag{2.14}$$

where ρ_p and ρ_f are the density of the particle and the fluid respectively, V_p the volume of the particle, g the gravity force, $\Delta\chi$ the difference between the susceptibility of the particle and the fluid, which for PBS is -9.05·10^{-6} A/m^2 thus negligible in respect to the one of the particle considered, lastly $\nabla\mathbf{H}$ is the magnetic field gradient, which for these experiments has been estimated to be 8.2·10^6. Using Equation 2.14 the magnetic field assisted sedimentation time for superparamagnetic beads and HCs, using the χ value for hemozoin found in previous experiments, has been estimated to be 7 s and 7500 s respectively. Those values have been also confirmed trough numerical simulations using COMSOL 5.2a. In Figure 2.6(B) the $\Delta R/R_0$, produced by the beads (red line) and the hemozoin (blue line), caused by the progressive sedimentation of the particle on the electrodes is reported. The resistance variation has been normalized from 0 to 1 so that both the signals have the same amplitude. The important information that should be noticed from the graph is the sedimentation time which are in the order of 10^2 and 3·10^3 for beads and HCs respectively, thus in agreement with the simplified estimation. A susceptibility value of 10^3 for hemozoin, three order of magnitude higher than the magnetic beads used, like the one reported by Inyushin et al. [30] would give a much lower sedimentation time. Thus, in conclusion, the measurements performed on hemozoin crystals show an electrical insulating behaviour both in DC and AC and a paramagnetic property.

2.5 Magnetic capture of RBCs

The capture capability and concentration factor of the Ni pillars geometry have been assessed through capture experiments using a model of iRBC, i.e. red blood cells treated with $NaNO_2$ (tRBC) in order to convert the hemoglobin into a met-hemoglobin which have paramagnetic properties similar to the infected RBCs (see Section 4.5 for a detailed explanation on the treatment procedure). Starting from the identified optimal geometry, namely an hexagonal matrix of cylinders with 20 μm height, four promising variants have been tested, in which the radius, r, and the centre-centre spacing between the pillars, d, have been varied. In particular, the geometries object of this study are (indicated with the abbreviation $2r$-d): 20-80, 20-160, 40-80, 40-160. Different chip layouts have been fabricated following the micro-fabrication process described in Section 4.1. Of the 1.5x1.5cm^2 chip surface, a 1x1cm^2 portion presents the pillars embedded into the substrate. The experimental setup used in this experiments is schematically depicted in Figure 2.2(A). The magnet assembly is positioned on the back of the chip, whose opposite side, presenting Ni pillars embedded on its surface, is facing downwards perpendicularly to the ground. The silicon chip is leaning on a glass slide.
A 40 μm thick confinement ring, also called *gasket*, interposed between the chip and glass slide is used as a lateral confinement for the sample fluid defining a δ=40μm deep microfluidic chamber. The gasket has been micro-fabricated onto the glass substrate through optical lithography using the positive photoresist AZ40XT (MicroChemicals). For each experiment a few μl drop of the sample is dispensed on the glass slide, inside the gasket. The sample consist in a solution of heparin-plasma-PBS solution (1:1:100) in which tRBC, labelled with a green fluorescent dye (Cell Tracker Green CMFDA Dye, C7025, Invitrogen) and/or hRBCs in different amount and ratios in order to simulate different haematocrit values. The chip and magnet assembly are placed on the

glass substrate after 30 s, which is slightly higher than the time needed to perform all the manipulations required to correctly position the chip in respect to the gasket and such time interval is kept fixed during all the experiments in order for the starting state of the sample to be reproducible. The development of the capture progress is monitored through a fluorescence microscope (Olympus IX70) and taking pictures both of the chip and glass surface in order to be able to count the number of tRBCs captured and not respectively. In Figure 2.7 two fluorescence microscopy images of the tRBCs captured by the pillars are shown. Pictures are taken at fixed time intervals from the

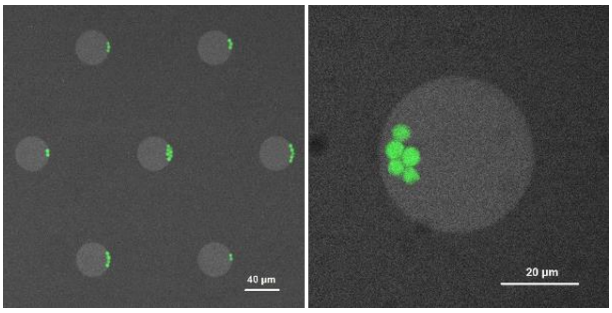

Figure 2.7: *Fluorescence microscopy images of tRBCs, labelled with a fluorescent dye, capture by the magnetic pillars.*

starting of the experiment: 2, 4, 6, 10 and 15 min. Due to restrictions in the use and processing of human blood in the laboratory where this activity has been carried out, all the experiments have been performed on bovine tRBC. However, the goodness of bovine red blood cells as a model for the human ones has been assessed with two comparative capture tests with the same parameters, only changing the RBC source, i.e. human and bovine. In both tests, 4% of the sample volume of the sample volume was composed by RBCs (i.e. mimicking a 4% haematocrit, HT) of which only 1% treated. In Figure 2.8 the capture efficiency, resulting from this study, as a function of time and defined as:

$$\eta = \frac{N_{tRBC}^{captured}}{N_{tRBC}^{captured} + N_{tRBC}^{uncaptured}} \tag{2.15}$$

where $N_{tRBC}^{captured}$ and $N_{tRBC}^{uncaptured}$ indicate the number of tRBCs captured by the Ni pillars and sedimented on the bottom of the sample chamber respectively,is shown. As can be noticed, both the human and bovine curves present the same morphology and their amplitude are almost equal. Thus, bovine RBCs can be considered as an adequate model for humans one,considering a 5% overestimation of the capture efficiency of the human RBCs.

Afterwards, the capture capability differences of the aforementioned pillars geometries and different gasket thickness have been investigated. In these test, only tRBCs were suspended in the solution, with a equivalent HT=0.4%, to have a better optical visualization of the captured cells, as a high presence of not captured RBCs on the bottom of the microfluidic chamber prevents a good light transmission of the light from/to the microscope lens located below the glass slide. Thus, the competition between the ascendant tRBCs and descendants hRBC, as there would be in a real blood sample, it is not considered in this study. In Figure 2.9(A) and (B), the adopted gasket thickness is 20 μm and 40 μm respectively. As it can be seen a more compact geometry, i.e.

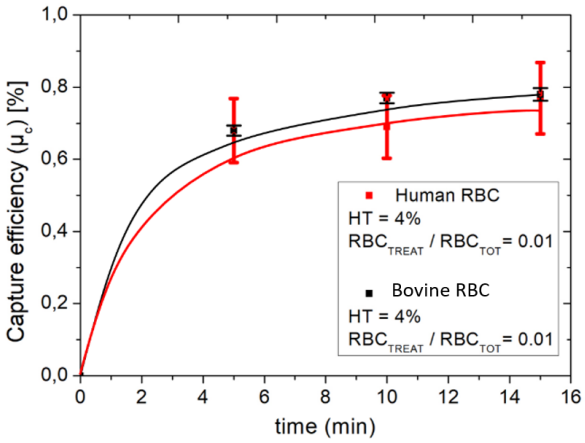

Figure 2.8: *Capture efficiency comparison for human tRBCs (red line) and bovine ones (black line). The markers represent the experimental data while the line their interpolation.*

characterized by a smaller spacing d between the pillars performs better than a less dense one. However, pillars with a larger diameter $2r$ are able to capture particles at a greater depth. This last relationship can be deducted looking at the two graph simultaneously and in particular to $20 - 80$ configuration. With a gasket thickness of 20 μm both the $40 - 80$ and $20 - 80$ are the best performing ones due to their higher pillars density. However, moving to a 40 μm gasket, the smaller pillar diameter configuration (i.e. $20 - 80$) is not able to attract particles at such depth, thus performing worse than a less dense but with larger diameter one, like $40 - 160$.

The experiments in Figure 2.9(B) have been also simulated using COMSOL 5.3a in order to assess the complete understanding of the particles driving forces in play.
The results of these simulations are reported in Figure 2.9(C) showing a good agreement with the experiments and validating the capability of the simulation platform to accurately represent the system and guide the design phase.
For a detailed explanation on the simulation setting and environment please refer to Appendix 6.1.
The choice of the best geometry for the aim of this project, however, should also take into account not only the capture efficiency parameter but also other parameters imposed by the electrical impedance detection requirements. A less dense geometry, despite lowering the capture efficiency, is indeed preferred as it is able to attract the particles in a smaller area also increasing the available space and design flexibility of the electrodes layout. For a deeper focus on these considerations as well for the choice of the optimal configuration please refer to Section 3.3.

Concerning the competition due to the presence of hRBCs together with tRBCs and its effects on the capture efficiency, two main experiments have been carried out. In a first experiment (Figure 2.10(A)) the RBCs HT was 0.4% while in the second (Figure 2.10(B)) increased to 4%, of which only 0.02% of them treated. As it can be noticed, an increase in the number of hRBCs causes a decrease of the capture efficiency. This can be easily explained as the hRBCs which sediment on the bottom of the chamber thwart the rise of tRBCs towards the top, such competition becomes more effective as the quantity of hRBCs increase. Even in this case the considerations, about the geome-

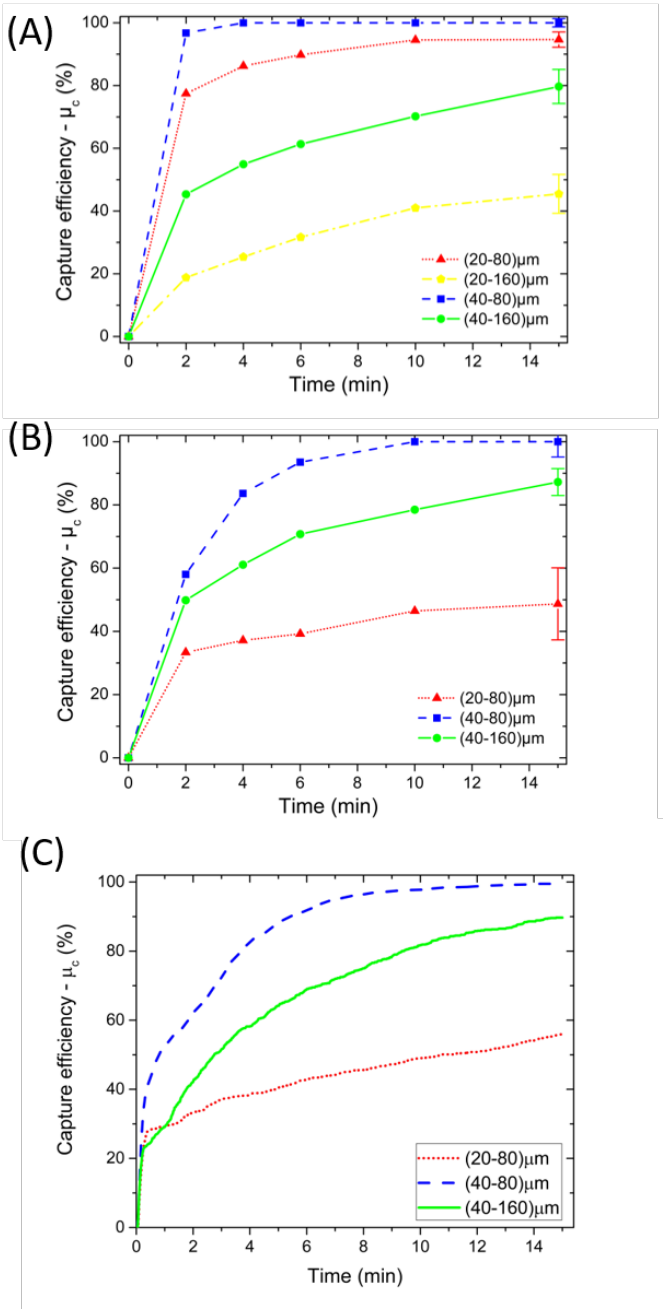

Figure 2.9: *Capture efficiency comparison of different pillars geometry using a (A) 20μm and (B) 40μm gasket. (C) Simulation of the experiments in Subfigure (B) using COMSOL 5.3a*

try parameters, mentioned above apply.
A fundamental aspect for a diagnostic tool is the absence or limited false positive cases. In the device object of this thesis, this translate in not having the attraction of hRBC. In order to assess the capability of the technique to capture only the iRBC without attracting the healthy ones, also the presence of the latter ones on the surface of the chip have been monitored during the experiment reported in Figure 2.10.B. The gray line, indeed, shows the capture efficiency of the system for the hRBCs, which is equal to

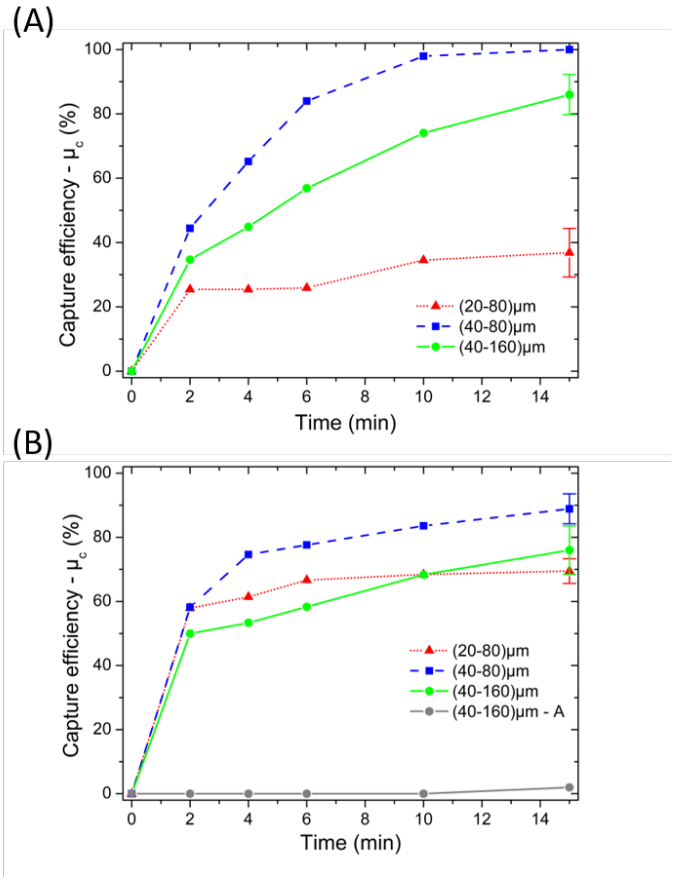

Figure 2.10: *Capture efficiency comparison of different pillars geometry (A) with a hRBCs haematocrit of 0.4% and (B) 4%. In both cases, the concentration of tRBC is 0.02%.*

0% for the first 10 min of the experiment, while it reach 2-3% after 15 min. However, during this experiment an interesting phenomenon, which could explain such unspecific attraction, has been noticed. As a matter of facts, after 10 min from the start of the experiments, the lysis of some tRBCs has been observed thanks to the fluorescence label. Soon after this event some neighbouring hRBC, previously lying on the bottom of the microfluidic chamber, started to ascend to the top. A possible interpretation of this behaviour could lies in the fact that the explosion of a tRBC cause the dispersion of its met-Hb or labelling dye content inside the solution, changing χ_f thus altering $\Delta\chi$ and causing its attraction to the pillars. However, from this experiment, it is possible to deduce a capture efficiency of hRBC of 0% for a test duration below 10 min, thus the false positive ratio due to unspecific attraction null.
Given the peculiar distribution of the external magnetic field gradient provided by the permanent magnet assembly, it is fundamental to measure the capture efficiency as a function of the position in respect to the magnet, in order to efficiently place the pillars. The two permanent magnets perch on the chip on their 20x5 mm^2 face; the 0.2 mm μ-metal sheet is interposed between the two larger faces of the magnets (i.e. 20x20mm) end have their same dimensions. Thus, the μ-metal sheet projects a 20 mm line on the chip plane; this line is, according to simulation, the line where the magnetic field is the highest. Given the obvious invariance of the magnetic field gradient along te direction

parallel to said line, the capture efficiency have been measured as a function of the lateral distance (i.e perpendicular) from the μ-metal sheet line. Figure 2.11 shows the capture efficiency as a function of the distance from the aforementioned line. The black dots represents the experimental data, while the red line the Gaussian fitting of data. As expected the maximum efficiency is along the line, decreasing moving away from it until reaching 0% at a distance of 2 mm. This information is extremely useful for an

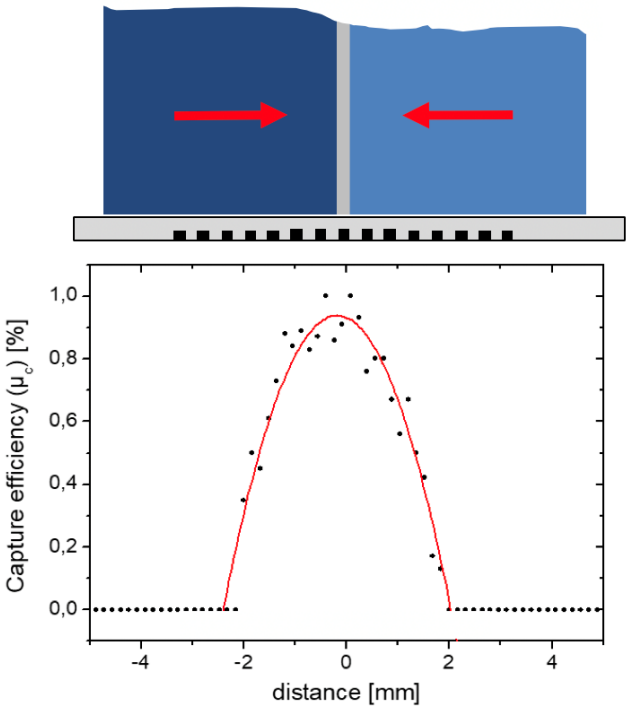

Figure 2.11: *tRBCs capture efficiency as a function of the distance from the μ-metal sheet interposed between the two magnets composing the magnet assembly. On top a schematic representation of the magnet assembly and its position with respect to the chip.*

efficient design of the chip, as the Ni concentrators, and so the detection electrodes, have to be put along the μ-metal line not exceeding a width of 4 mm. A wider region of pillars will be then useless and detrimental for the electrical detection, as the electric signal is proportional to the average number of RBCs captured on each pillar.
In this work the Ni concentration region was decided not to be put where the capture efficiency is lower than 60%, thus making its width equal to 3mm. Concerning the length of the pillars region there are no constraints from a magnetic point of view, unless not to exceed the 20mm of the μ-metal line. Even in this case electrical detection considerations must be done and will be discussed in Section 3.3.
In conclusion the optimal magnetic concentrators geometry found consist in hexagonal matrix of cylindrical pillars 20 μm high, fixed by fabrication constraints. The pillars should be positioned along the μ-metal sheet line and less than 2 mm from it in order to maximize the capture efficiency. The choice of the pillars diameter and spacing as well as their number is postponed to Section 3.3 as it should also take into consideration electrical impedance detection considerations. However the favourite pillars geometries that emerged experimentally are 40-80 and 40-160.

CHAPTER 3

Electrical Detection

3.1 Electrical Impedance spectroscopy in liquid

Electrical impedance spectroscopy (EIS) is an useful technique that allows a complete characterization of the electrical properties of a material or a more complex system as a function of frequency. EIS can be applied to a broad variety of applications: biological, electrical, optical, chemical, etc. [91, 92] From its first use by Nerst in 1894, this technique experienced a wide diffusion mainly because it is easy to use, low cost, fast, label free and allows an analysis of all the electrical parameter of a material, i.e resistance, capacitance and inductance. [92] It involves the application of an external current or voltage sinusoidal signal to the sample or device, whose electrical properties are to be measured, and then recording the induced current or voltage.
EIS requires the use of, at least, two electrodes. One electrode is needed to apply, for example, the bias sinusoidal voltage, $V(j\omega)$ to the device under test (DUT) while the second one to measure the resulting current I(jω). Thus knowing the voltage applied and measuring amplitude and phase of the current, it is possible to obtain both the real and imaginary part of impedance, $Z(j\omega)$ as:

$$Z(j\omega) = \frac{V(j\omega)}{I(j\omega)} = \frac{V}{I}e^{-j\phi} \tag{3.1}$$

where V and I are, respectively, the voltage and current amplitudes and ϕ the phase difference between the two signals. In Tid Mekii, the electrodes are put in contact with a liquid (i.e. PBS or blood plasma) as the liquid itself is the DUT. In fact the presence of a particle, captured between the electrodes, changes the overall electrical properties of the sensed fluid. However, when dealing with electrodes immersed in a fluid some considerations must be taken into account. As a matter of fact, while in materials the conduction of electrical signals is characterized by the movement of electrons, in a

fluid this happens thanks to the movement of ions, whose dynamics are different from their counterpart, giving rise to peculiar trends in the impedance spectrum. In particular, the mobility of ions is much lower than the one of electrons, generally about six order of magnitude lower and approximately 10^{-3}cm^2/(V·s). [93] Moreover it should be pointed out that electrons can not leave the material going into the liquid and vice versa. A charge transfer between the material and the liquid can only occurs if reduction or oxidation reactions take place between the atoms of the material and the ions (or molecules) of the liquid.
An ionic solution or electrolyte, such as PBS and blood plasma, is a liquid containing ions. Said ions, without an external electric field applied are distributed randomly due to the thermal agitation (brownian motion). However, if an electric field is applied to the liquid, a displacement of the ions towards the electrodes takes place, thus, generating a current. The amount of current flowing in the liquid depends on its conductivity, which in turn depends mainly on the concentration of ions in solution. The flow of current, if the external electric field is kept constant, decreases to zero as the ions reach the surface of the electrodes. As mentioned before, no charge can be transferred at the electrode-electrolyte interface, unless reactions between the two occur. For the aim of this thesis, it will be assumed that no redox reactions are allowed at the interface. In this case the ions move to the electrodes, in particular cations to the negatively charged electrode while anions to the positive one. Once reached the electrodes surface, the ions, being unable to pass through or react, remain stuck at the interface until the electric field is applied. A double layer of charges is then created at the electrodes-electrolyte interface, formed by the cations/anions in the liquid and electrons/proton in the material as shown in Figure 3.1. The movement of charges in the liquid continues until the ions completely shield the electric field. Ions are not directly in contact with the surface of the electrode but remain at a distance of 0.3-0.8 nanometers from it due to the polarity of water molecules which surround the ions creating a shell. Thus, two different planes can be identified at the interface: inner Helmholtz plane (IHP) and outer Helmholtz plane (OHP). [95] In the region between the former one and the electrode, only water molecules are present, the latter, that pass through the centres of the ion layer, marks the border between the compact layer and the diffuse layer. [96] As can be noticed a capacitance is formed at the interface as there are two opposite charged layers separated by a dielectric (i.e. water molecules). This capacitance is called double layer capacitance C_{dl}.
The C_{dl}^0 value can be obtained as the series of two capacitive effects: the compact layer capacitance C_H and the diffuse layer capacitance C_D. The former contribute is given by the charge distribution close to the electrodes (below 1 nm) while the second one by the charge distribution in the diffuse layer (1 to 10 nm from the electrodes). The two entities can be obtained as:

$$\begin{aligned} C_H &= \epsilon_{sat}\frac{A}{d} \\ C_D &= \epsilon\frac{A}{L_D}\cdot cosh\left(\frac{zq\phi_0}{2kT}\right) \end{aligned} \tag{3.2}$$

where ϵ and ϵ_{sat} are the unsaturated and saturated dielectric constant of the water respectively, d the distance between the two layers of charges, A the electrode area, L_D the Debye length, ϕ_0 the potential drop across the diffuse layer, k is the Boltzman con-

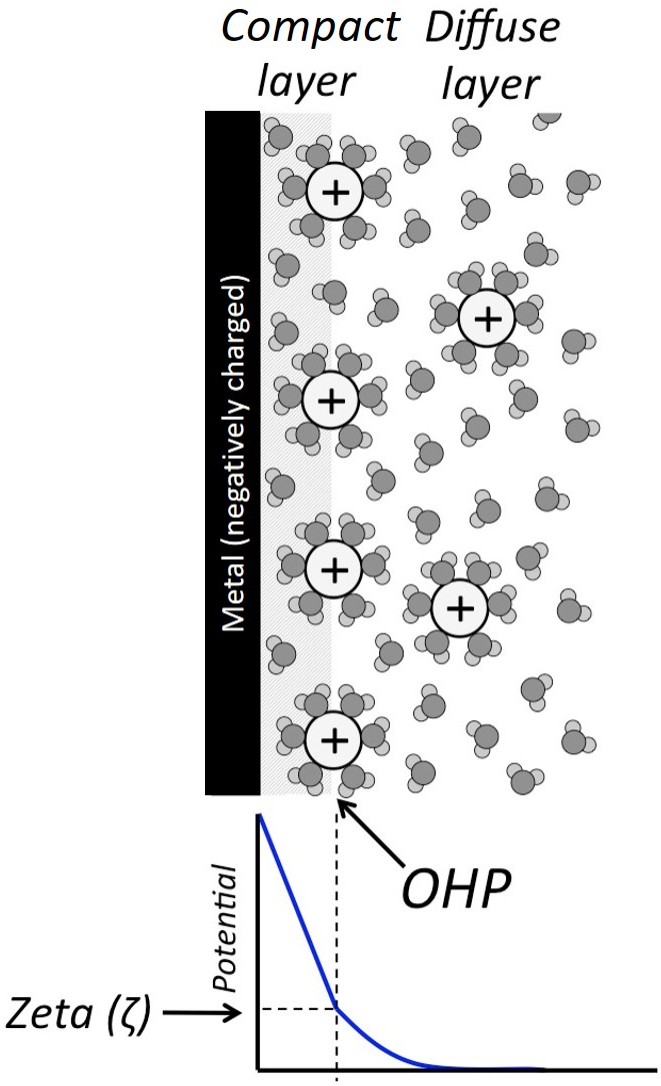

Figure 3.1: *Schematic representation of the positioning of ions at the electrode and electrolyte interface when an electric field is applied. [94]*

stant and T the temperature. Thus C_{dl} depends mainly on the electrodes material and on the solution concentration and type. In this project electrodes are made of gold and they are immersed in a solution of PBS and blood plasma, which both have almost the same ions concentrations. For this combination of electrodes and electrolyte, typical double layer values per unit of area are 10-20 μF/cm^2. [97]
Applying a sinusoidal electric potential, the double layer capacitance effect on the current decreases increasing the frequency of the stimulus, as the ions have no longer time to accumulate at the electrodes interface. Thus the electrode-electrolyte interface phenomena, become less important, leaving the place to bulk transport ones, which depends on the conductivity ρ_f and permeability ϵ_f of the bulk solution.
The aforementioned phenomena give rise to impedance behaviour that can be schematically resumed by the electric equivalent reported in Figure 3.2(A). Each electrode-

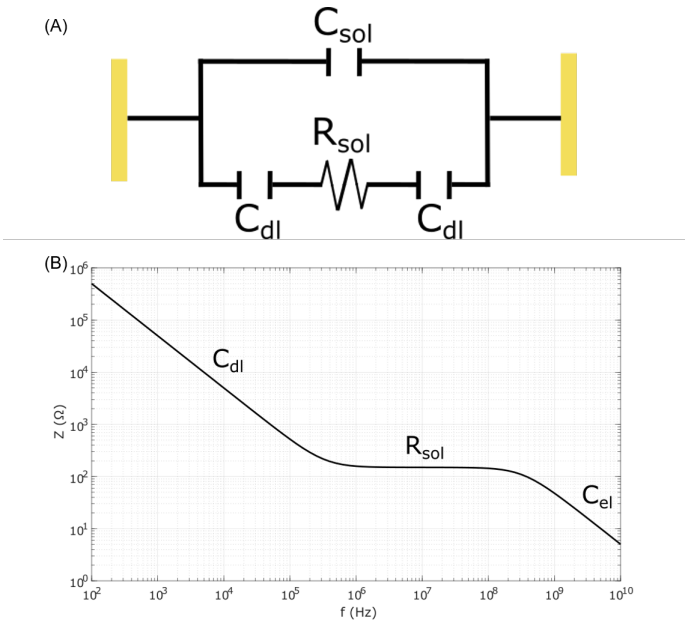

Figure 3.2: *(A) Electric impedance equivalent of the solution seen by two electrodes. [98] (B) Example of a generic electrical impedance spectrum in liquid.*

electrolyte interface cause a double layer capacitance effect, thus, in a two electrodes system there are two C_{dl} contribution that are in series with the solution resistance which mainly depends on the solution conductivity σ_f and the geometrical parameters of the electrodes as their area, A and distance, d. In the case of parallel plate electrodes the solution resistance is given by:

$$R_{sol} = \frac{1}{\sigma_f}\frac{d}{A} \tag{3.3}$$

The series of the two C_{dl} and R_{sol} is in parallel with the capacitance between the electrodes, C_{sol}, which depends on the electrical permittivity of the fluid ϵ_f and the geometrical factors of the electrodes. By considering again the simple case of parallel plate electrodes we have:

$$C_{sol} = \epsilon_f \frac{A}{d} \tag{3.4}$$

The total equivalent impedance is given by:

$$Z_{eq} = \frac{Z_{series}}{1 + j\omega C_{sol} Z_{series}} \tag{3.5}$$

where $Z_{series} = R_{sol} + \frac{2}{j\omega C_{dl}}$.
The model presents one zero and a pole at frequencies where, respectively, the R_{sol} contribution become dominant over C_{dl} and the C_{sol} over R_{sol}. The frequency of the zero, f_z, and the one of the pole, f_p, can be obtained by Equation 3.6 and 3.7 respectively, where C^0_{dl} is the double layer capacitance per area (F/m^2).

$$f_z = \frac{1}{\pi R_{sol} C_{dl}} = \frac{\sigma_f}{\pi d C^0_{dl}} \tag{3.6}$$

$$f_p = \frac{1}{2\pi R_{sol} C_{sol}} = \frac{\sigma_f}{2\pi \epsilon_f} \tag{3.7}$$

The resulting impedance spectrum given by this model is reported in Figure 3.2(B). As can be noticed, the impedance of the double layer capacitance is dominant at frequencies below f_z, and it decrease with frequency. At f_z the double layer impedance becomes equal to the one due to the solution resistance, thus the latter becoming the dominant term in frequencies between f_z and f_p. Above f_p (approximately 300 MHz in case of PBS) the solution capacitance impedance bypass the series of the two former contributions.

3.2 Impedance detection

EIS, besides being a powerful technique for the electrical characterization of a material, it can also be used for detection applications where an event or the analyte of interest causes a change in the electrical parameters of the material itself. As described in the previous Section, three main electrical properties can be measured through EIS in liquid, i.e. C_{dl}, R_{sol} and C_{sol}.
In this project the aim is to detect particles (HCs, iRBCs) that are attracted, magnetophoretically, close to the electrodes. Thus, it is fundamental to understand which of the aforementioned physical quantities, characterising EIS in liquid, are more subject to changes due to the presence of the particles of interest in this thesis.
In this regard, C_{dl} is a property sensitive only to the state of the liquid few nanometers close to the electrodes and to their atomic structure. Thus, C_{dl} is minimally influenced by the presence of particles close or between them, which makes this parameter unsuitable for such kind of detection. On the other hand, R_{sol} and C_{sol} are sensitive to the bulk properties of the fluid, in particular its conductivity and permittivity. Despite they could be both suitable for particle detection, in case that the fluid σ_f and ϵ_f are significantly different from the one of the particles, C_{sol} due to its dominance at frequencies above tens of MHz, sets significant constraints and greatly increase the complexity and resolution of the electronic measurement system. As a result of these considerations, R_{sol} is the most suitable property for impedance detection. At this point it is necessary to ascertain that the electrical conductivity of the particles of interest, σ_p, i.e. HCs and iRBCs, is significantly lower or higher than the one of the fluid, which in our case is PBS and Plasma, both with approximately the same low conductivity σ_f=1.5 S/m. As established in Section 1.1.2, hemozoin is an insulating particle for both DC and AC frequencies up to few MHz, thus its σ_p is negligible compared to σ_f. RBCs, on the other hand, have a more complex structure but their electrical properties are well studied. Cells, thanks to their cellular membrane, which acts as a capacitor, are insulators ($\sigma_p \rightarrow 0$) up to tens of MHz frequencies. [99] Such capacitor is bypassed for frequencies above GHz, making the resistance of the cell cytoplasm, which is characterized by a conductivity equal to the one of PBS and Plasma, the dominant contribution. Thus, electrical impedance detection of cells based on the conductivity changes of the fluid is possible below GHz frequencies. Such frequency interval is completely compatible with the one where R_{sol} contribution is dominant, i.e. between hundreds of kHZ to few tens of MHz. Once assessed that the particles object of this study have a conductivity value significantly different from the one of the fluid, it is necessary to understand how

the latter is influenced by the presence of a particle.
Considering a volume, V_f, containing a fluid, whose conductivity is σ_f, and a particle, the overall conductivity of the fluid-particle mixture, σ_{mix}, can be obtained from the Maxwell's mixture theory [100, 101]:

$$\sigma_{mix} = \sigma_f \left(1 + 3\frac{V_p}{V_f}\frac{\sigma_p - \sigma_f}{\sigma_p + 2\sigma_f}\right) \tag{3.8}$$

where σ_p is the electrical conductivity of the particle. Assuming the particle as an insulator, i.e. $\sigma_p << \sigma_f$, the previous equation can be simplified as:

$$\sigma_{mix} \approx \sigma_f \left(1 - \frac{3}{2}\frac{V_p}{V_f}\right) \tag{3.9}$$

Substituting the obtained conductivity value σ_{mix} to σ_f in Equation 3.3 it is possible to obtain the resistance of the mixture, R_{mix}, which in turn allows to calculate the relative resistance variation caused by the particle, $\Delta R/R_{sol}$, leading to:

$$\frac{\Delta R}{R_{sol}} = \frac{R_{mix} - R_{sol}}{R_{sol}} = \frac{3}{2}\phi = \frac{3}{2}\frac{V_p}{V_f} \tag{3.10}$$

where R_{sol} is the fluid resistance without the particle.
It is now possible to observe that the resistance variation is only proportional to the volume fraction occupied by the particle/s. Thus, in order to maximize the resistance variation it is necessary to reduce the measured fluid volume V_f while increasing the number of particles in said volume, i.e. increasing V_p. This is the main purpose of the magnetophoretic capture and concentration. $\Delta R/R_{sol}$ is in turn the signal that will be measured in Tid Mekii.
When dealing with electrodes it is necessary to define their sensitive volume, which represent V_f in the above Equations. In the case of two opposite side parallel plate electrodes, V_f is simply the volume between the two plates. For coplanar electrodes like the one shown in Figure 3.3, the sensitive volume corresponds to the volume where most of the current density is confined. Hence it corresponds to the electrodes area and the one between them, (i.e $(2W + S) \cdot L$ where W, L, S are, respectively, the width, length of the electrodes and the spacing between them) multiplied by the sensitive height H, which is approximately equal to S. [102] Thus $V_f = (2W + S) \cdot L \cdot H$.
Due to the fact that the raw signal registered from the instrumentation is a current and in particular, given the differential electrodes layout (see Section 3.3), a current difference Δi, many of the results showed in the following Chapters are reported accordingly. It is then necessary to underline how this quantity relates to the aforementioned $\Delta R/R_{sol}$. Starting from the well known Ohm's law I=V/R and denoting the resistance when a particle is present as $R_{sol} + \Delta R$, Δi can be easily obtained as:

$$\Delta i = i_1 - i_0 = \frac{V}{R_{sol} + \Delta R} - \frac{V}{R_{sol}} = -\frac{V\Delta R}{R_{sol}^2 + R_{sol}\Delta R} \tag{3.11}$$

where i_1 and i_0 correspond to the current with and without the particle respectively and V is the voltage bias amplitude applied to one electrode. Making the assumption that $\Delta R << R_{sol}$, Equation 3.11 can be rewritten as:

$$\Delta i = -\frac{V\Delta R}{R_{sol}^2} = -V\frac{1}{R_{sol}}\frac{\Delta R}{R_{sol}} \tag{3.12}$$

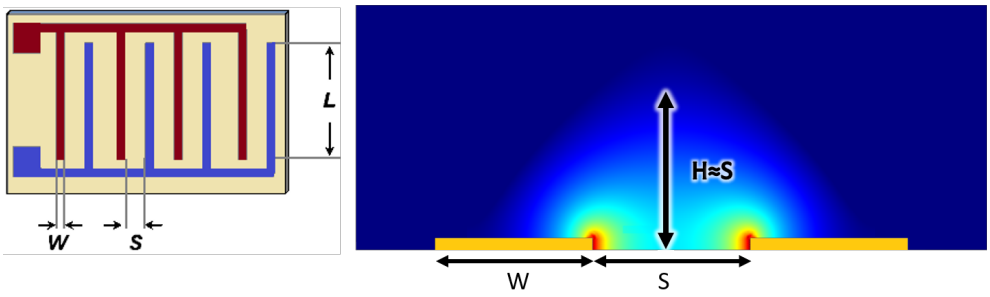

Figure 3.3: *Schematic structure of an interdigitated electrode reporting the main dimensions of such structure. On the left a top view of an interdigitated electrodes, on the right the side view of a couple of coplanar electrodes composing the structure. H is the sensitive height of the electrodes, i.e. the height where th 60% of the current density is confined. The colour plot shows the current density amplitude distribution.*

thus highlighting that Δi is still proportional to $\Delta R/R_{sol}$ divided by R_{sol} itself.
For the sake of completeness, as we are dealing with coplanar interdigitated electrodes, the equation to calculate the resistance of such electrodes configuration is given by: [91, 98]

$$R_{sol} \approx \frac{2}{\sigma_f \cdot (N-1) \cdot L} \cdot \sqrt[3]{\frac{S}{N}} \tag{3.13}$$

where N is the number of 'fingers' or electrodes forming the interdigitated electrode system. Despite this equation gives definitely more accurate results for this kind of electrodes, the discussion made in this Section, carried out using the simpler and more intuitive Equation 3.3 still holds as the dependencies remain the same.

3.2.1 Experimental validation of theoretical equations

The equations obtained. from the theoretical analysis of the resistance variation of the fluid due to the presence of insulating particles, have been verified trough specific and targeted experiments. For this purpose, a couple of interdigitated electrodes (see Figure 3.4(A) composed by 67 fingers 750μm long with 8μm width and spacing have been exploited. The electrodes, made of 30 nm of Cr as adhesion layer and 100 nm of gold on top, have been fabricated on a glass substrate. A confinement chamber, surrounding the electrodes, has been fabricated in Polydimethylsiloxane (PDMS) and bonded on the glass substrate. The confinement ring, in each experiment is filled with 1mL of PBS, thus submerging the electrodes.
The impedance of the electrodes has been monitored in time trough an impedance analyser at 1 MHz (HF2LI Lock-in Amplifier, Zurich Instruments). Subsequently, 10μl of PBS solution containing polystyrene beads, with different concentrations and diameters in each experiment, is added in the confinement chamber with a micro-pipette and the impedance variation caused by the sedimentation of the beads on the electrodes measured.
Using an immersion microscope, the average number of beads in five of its field of view (200x150μm) has been counted manually in order to have a precise estimate of the amount of beads effectively sedimented on the electrodes area. Figure 3.4(B) shows the example of an image of the electrodes, with 8μm diameter beads sedimented on top,

used for the quantification of the number of beads sedimented on the electrodes area.
In Figure 3.5 a sample signal, of the resistance variation ΔR of the electrodes as a

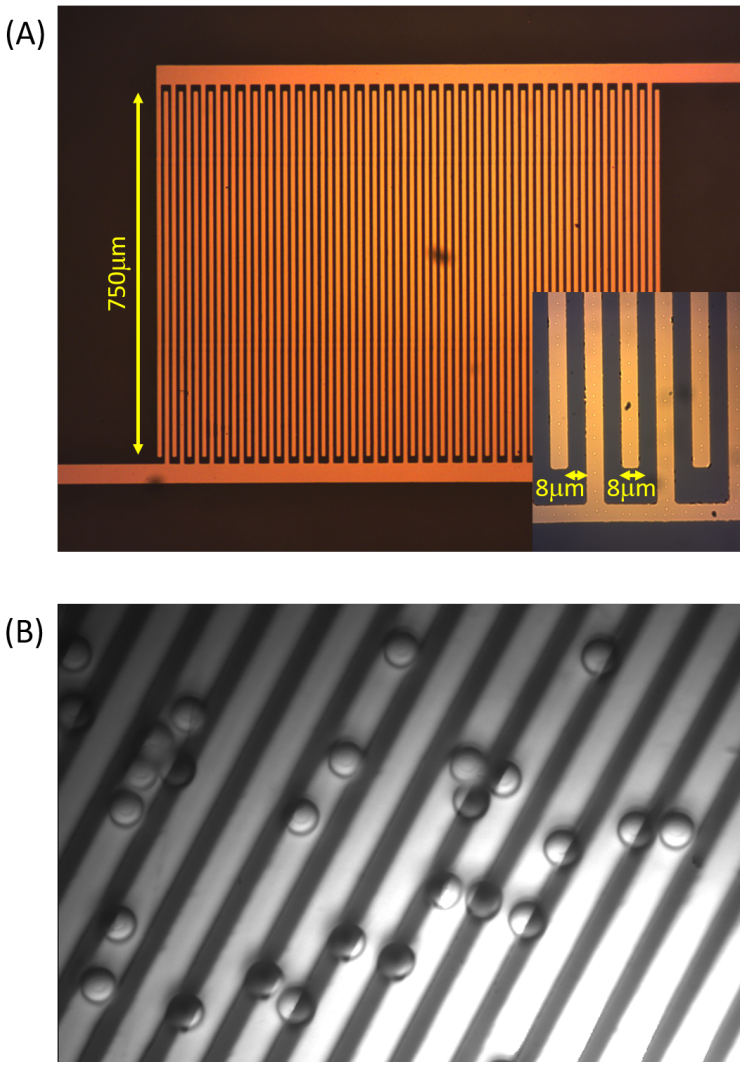

Figure 3.4: *Microscope images of the electrodes used for the validation of the impedance detection equations. (A) Entire structure of the electrodes. (B) Electrodes with 8µm diameter polystyrene beads sedimented on top.*

function of time, obtained from these experiments is reported. The initial value of the resistance, i.e. R_0, has been set to zero in the plot to better appreciate the signal amplitude. In particular R_0 has been measured experimentally to be 22 Ω which is similar to the one obtainable using Equation 3.13 giving a 34 Ω estimation. The total resistance variation, ΔR, is calculated as the difference between the initial resistance of the electrodes R_0, i.e. before the addition of beads to the PBS solution, and the resistance after the beads complete sedimentation. Highlighted by a red ellipse in Figure 3.5 is the spurious signal caused by the insertion of the micropipette in the PBS and consequent beads release in it.
Several experiments have been carried out exploiting different beads concentrations and diameters (10, 8, 1 μm).

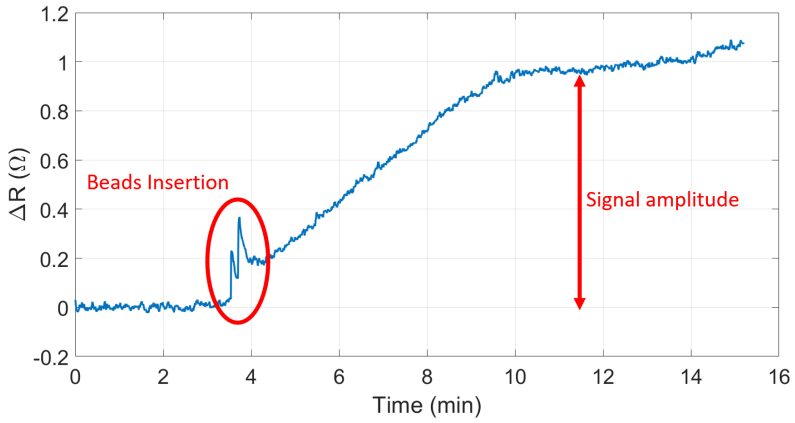

Figure 3.5: *Resistance variation as a function of time obtained from the sedimentation of 8μm diameter beads on the electrodes. The red ellipse highlights the artefact caused by the insertion of the beads using the micro-pipette.*

In Figure 3.6 the results of said experiments are reported. In particular, in Figure 3.6(A) the relative resistance variation, $\Delta R/R_0$, is plotted as a function of the number of beads counted on the electrodes. As can be noticed, the experimental data (markers) are in good agreement with the theoretical estimations given by Equation 3.10 (solid lines). Moreover, $\Delta R/R_0$ linearly increase with the number of particles and it is proportional to the beads volume, V_p as expected.
The latter aspect is further confirmed displaying the previous data as a function of the volume fraction (V_p/V_f) instead of the number of beads, as shown in Figure 3.6(B). In this plane, all the data, independently from the beads diameter, align along a single line, clearly showing that the volume fraction is the only dependence of the resistance variation.

The results of these experiments demonstrate the accuracy and effectiveness of the theoretical equations obtained and their simple applicability in practical experiments.

3.3 Electrodes Layout

The design of the electrodes must take into account both electrical and practical considerations due to the experimental setup (see Section 4.2 for a detailed description of the setup) and it should also adapt to the magnetophoretic needs.
Primarily the design should maximize $\Delta R/R_{sol}$ in order to obtain the maximum resistance variation due to the presence of each particles. This translates into minimizing the volume sensed by the electrodes, i.e. V_f. Thus the electrodes have to be put only where the particles of interest are captured and concentrated by the pillars. For this purpose it can be noticed, in Figure 2.7 in Section 2.5, that tRBCs are not attracted to the centre of the pillars but on their border. This phenomenon is due to the accumulation of magnetic charges, a fictitious equivalent to electric charge, on the edges of a solid. The electrodes should be then be put in correspondence to said borders, leaving the centre of the pillars not sensed. Following this consideration the sensitive geometry of the electrodes have been designed with a ring shape as shown in Figure 3.7(A).
The electrodes thickness and spacing has been chosen to be 3 μm in order both to

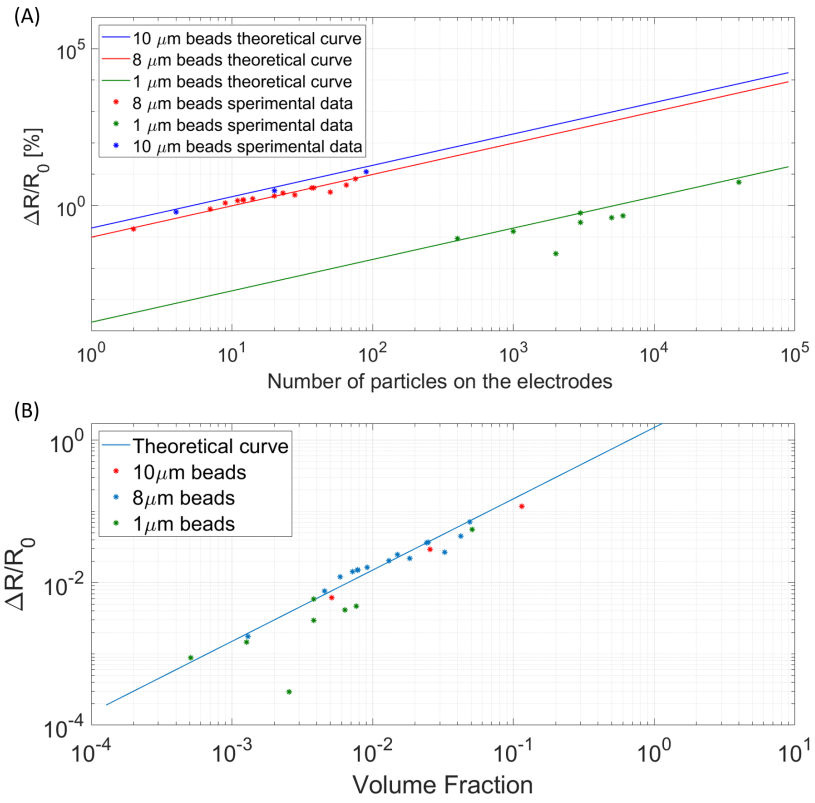

Figure 3.6: *Resistance variation as a function of (A) the total number of beads on the electrodes and (B) the volume fraction occupied by the beads. Beads of 10, 8 and 1 μm have been used in these experiments.*

embrace the entire capture region, i.e. a 9 μm wide annulus, and to be sensitive to a depth slightly higher than the thickness of a RBC (3 μm). The annulus external diameter depends on the pillar diameter. Resuming from the discussion left open in Section 2.5 about the optimal pillars geometry, the two configuration with the highest capture efficiency in a realistic situation (i.e. with the competition of hRBCs) have been considered, that are $40 - 80$ and $40 - 160$. Despite the former performs better in term of capture efficiency, almost around 10-20%, depending on the capture time considered, the latter offers a 50% higher concentration capability, as the pillars are half densely distributed, offering also flexibility for the design of the tracks, not only in terms of path but also width, connecting the sensitive areas of the electrodes. Following these considerations, a pillar diameter of 40 μm and a 160 μm centre-centre spacing has been chosen for the chip layout.

Another discussion left open during the design phase of the magnetic concentrators layout is the length of pillars area, which in turn means choosing the number of sensitive electrodes areas composing each sensor. The choice of this parameter should take into account considerations about the overall resistance of the sensor, the resolution limit achievable from EIS in liquid and the volume of liquid subjected to magnetophoretic capture. Looking at Equation 3.10, the $\Delta R/R_{sol}$ is maximised when the volume sensed by the electrodes is minimum, thus corresponding to a number of electrodes or pillars equal to one. However, doing so, the volume of liquid subjected to magnetophoretic

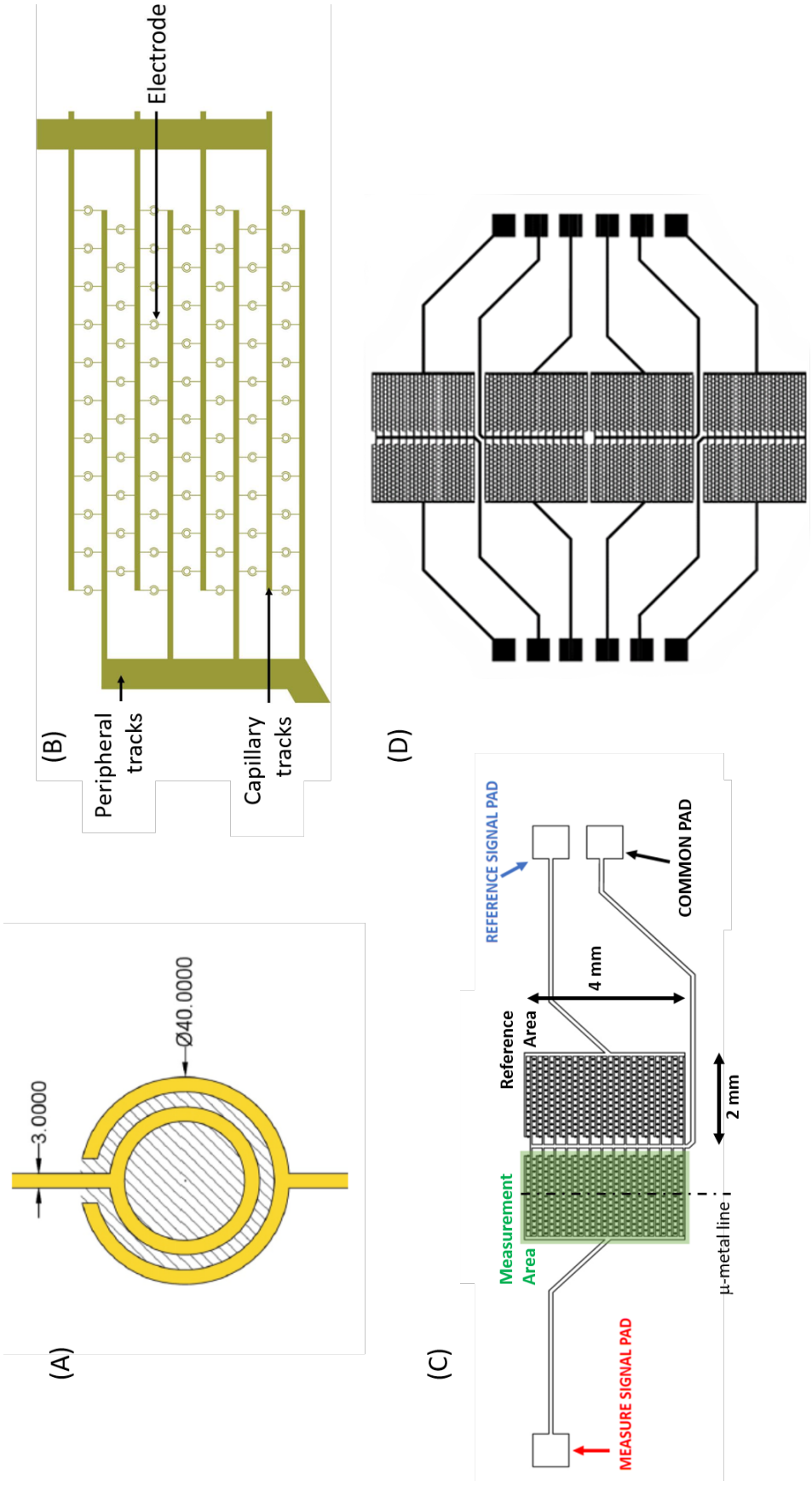

Figure 3.7: *(A) Layout of the sensitive part of one couple of electrodes. (B) Interdigitated placement of the sensing part of the electrodes. (C) Complete sensor layout comprising a measurement and a reference area. (C) Complete layout of the chip comprising 4 independent sensors.*

capture would be approximately 0.01 μl, considering the capture happening in a cylinder with 500 μm height and a base of 160 μm. According to the project specifications, the aim is to obtain a device with the same sensitivity of the gold standard (i.e. microscopy) which is approximately 10 parasites/μl or 10 iRBCs/μl. Hence, it is clear that while having only one pillar/electrode leads to the maximum sensitivity, enabling to detect a single iRBC, on the other hand it is not enough to achieve a reliable diagnosis, as the probability of the device to collect an iRBC, giving a right diagnosis, is 1%. Following this consideration and wanting to provide a more reliable diagnosis based not to only one iRBC but at least ten, the volume of fluid examined should be at least 1μl, leading to a number of electrodes $> 10^2$. However, their number is limited by the resolution, in terms of $\Delta R/R_{sol}$, achievable with standard EIS in liquid which is approximately 10^{-3}, mainly limited by the fluctuation of the fluid due to temperature changes. [103]
Starting from Equation 3.10 it is possible to calculate the maximum number of electrodes allowed in order to detect 10 particles which turns out to be $< 10^2$. Thus, the optimum number of electrodes appears to be 100. However, considering that the capture efficiency is lower than 100%, the number of electrodes should be increased, which is in contrast with the consideration regarding the minimum detectable parasitemia. A possible solution is to lower the $\Delta R/R_{sol}$ resolution, which implies increasing the complexity of the sensor, in order to gain more flexibility for the choice of the number of electrodes.
A way to decrease the $\Delta R/R_{sol}$ resolution, down to approximately 10^{-4}, is to implement a differential measurement in order to partially compensate the resistance variations of the fluid due to temperature fluctuation and reject the common mode noise sources. [103] According to such new resolution value the number of pillars/electrodes could be set between 10^2 and 10^3. According to this interval, their number have been chosen to be 350. Concerning the implementation of a differential sensor, an exact replica of the electrodes has been made, which, unlike the starting ones, does not have a Ni pillar beneath them; thus, they will be unaffected by the magnetophoretic capture of particles and consequently their resistance R_{sol} can be considered constant. The two different electrodes areas, which will be called Measurement and Reference to point out the areas provided and unprovided with pillars respectively, are connected together as schematically depicted in Figure 3.8. The new structure is a tripole in which the two external ends are connected to two counter phase sinusoidal signal with the same amplitude while the central one, which joins the measurement and reference areas together, to ground connecting it to the inverting input of a trans-impedance amplifier (TIA) which measure the current coming inside/going outside of said node. Thanks to this architecture, as far as the two areas have the same resistance (Figure 3.8(A)) the current flowing in one area equals the other one and no current flows in the TIA feedback resistor. However, if the two resistors resistance are not matched, as it happens when particles are attracted by the measurement area only, the current difference flowing in the two branches flows in the TIA feedback loop. In the same way, only noise contributions that affects only one or both areas differently are sensed by the amplifier, while the common mode noises are cancelled out.
As all the electrodes will be connected in parallel, a growing number of electrodes implies a proportional decrease in the overall resistance of the electrode. R_{sol} is the

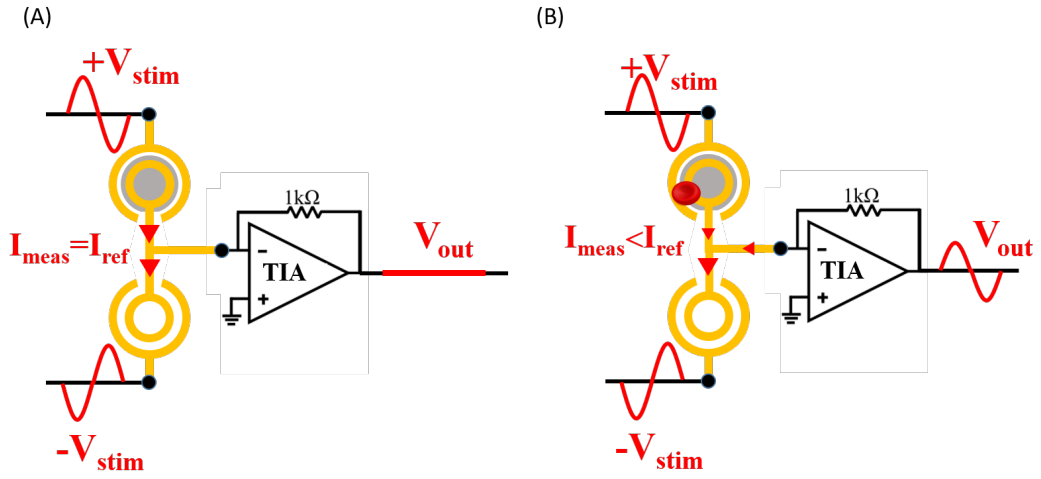

Figure 3.8: *Schematic representation of the working principle of the differential measurement implemented in Tid Mekii.*

resistance of the sensitive part of the electrodes only, but other resistance contributions take place in the overall sensor resistance like the resistance of the gold tracks connecting the sensitive areas and the contact resistance arising when connecting the chip to the measurement system. Those additive contributions to the overall resistance negatively affects the resolution as they increase the denominator of $\Delta R/R_{sensor}$, where $R_{sensor} = R_{sol} + R_{tracks} + R_{contact}$. Despite all these contributions can be minimized with a careful design of the chip layout and measurement setup, they are usually in the order of 10^1 Ω. Thus, it is important to verify that the resistance of interest, R_{sol} is higher than the others. The resistance value can be easily obtained from Equation 3.13 or more accurately through FEM simulations using COMSOL. The latter give a resistance estimate for the single electrode of 21 kΩ. The sensor resistance can be then calculated by simply dividing the obtained resistance value by the number of electrodes composing the measurement or reference area, i.e. 350. A resistance of the sensor of approximately 60 Ω is then obtained which is in the order of the other unwanted contributions.
Following all the above mentioned design constraints and guidelines it has been possible to completely design the sensor layout, reported in Figure 3.7(C). As it can be noticed, of the two identical areas composing the sensor, only the measurement area presents pillars beneath the electrodes and will be centred with the projection of the μ-metal sheet. Each area is 2x4 mm^2 and contains 350 electrodes connected in parallel by gold tracks as shown in Figure 3.7.B. Every chip contains 4 identical and independent sensors in order to obtain a more reliable diagnosis based on four parallel measurements. The final chip layout is reported in Figure 3.7(D). The overall chip dimension is 22x18 mm^2.

3.4 Electronic board design

A custom printed circuit board for the readout and digitalization of the signals coming from the sensor, as well as generating the sinusoidal signal stimuli, has been designed

and tested. In particular an impedance analyser has been implemented to perform EIS at a single frequency or over span of frequencies from 1 kHz to 10 MHz. In Figure

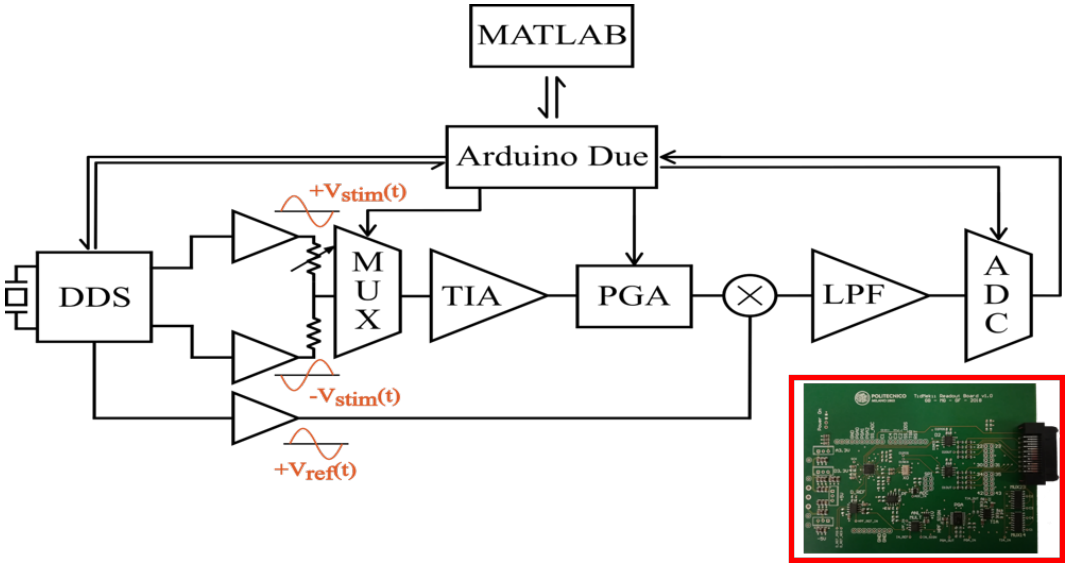

Figure 3.9: *Block diagram of the electronic system designed for Tid Mekii*

3.9, the schematic block diagram of the complete system is shown. Starting from left, a Direct Digital Synthesizer (DDS) generates the counter-phase sinusoidal signals for the reference and measurement areas of the sensor, as well as the reference signal for the analog multiplier, which is part of the lock-in amplifier (LIA) implemented for the signal demodulation. At the DDS outputs, three amplifier stages amplify and convert the differential current outputs of the DDS into voltage. The central nodes of each of the four sensors on the chip are connected to a multiplexer which select them sequentially, thus connecting one by one the sensors to the inverting input of a transimpedance amplifier (TIA). The input current coming from the sensor is amplified and converted to a voltage by the TIA, which output is further amplified by a preamplifier and a programmable gain amplifier (PGA).
The amplified sinusoidal signal coming from the sensor can be now be demodulated by a lock-in amplifier (LIA) consisting of an analog multiplexer and a low pass filter. As the device is meant to be used in endemic countries with limited economical resources, an analog LIA implementation has been preferred in respect to a digital one due to its reduced economic and time cost. The multiplier multiplies the PGA output, $V_a(t)$, to a reference sinusoid, $V_r(t)$, generated by the DDS, whose frequency is the same of the other sinusoidal signals generated by it. The result of this operation, $V_{out}(t)$, is:

$$V_{out}(t) = V_a(t) \cdot V_r(t) = V_a sin(\omega_0 + \phi) \cdot V_r sin(\omega_0) = V_a V_r \frac{cos(2\omega_0 + \phi)}{2} + V_a V_r \frac{cos(\phi)}{2} \tag{3.14}$$

where ω_0 is the frequency of the sinusoids and ϕ is the phase difference between the two. As it can be noticed two terms appear: the first term is twice the frequency in respect to the starting ones, while the second term is constant and depends both on the amplitudes of the starting sinusoids and on their phase difference. The purpose of the following low-pass filter (LPF) is to attenuate and make negligible the first term. Thus

a DC signal is obtained at the output of the LPF which is then digitalized by an ADC. It is important to point out that signals with a different frequency from ω_0, like noise and disturbs, are rejected by the LIA. The ADC conversion result is sent to a microcontroller, like Arduino Due, which performs a first processing of the data and then sends them, through USB communication, to a PC for a further processing and visualization. The microcontroller is also responsible to read/write the DDS registers, switch the multiplexer input and set the PGA gain.
Now that a general overlook of the entire system has been presented, each block of the circuit will be explained below.

Signal generation. In order to generate the sinusoidal signals for the measurement and reference areas of the sensor as well as for the reference signal, an AD9106 (Analog Devices) integrated circuit has been adopted. It is a quad DAC integrating a DDS that allows to generate 4 different programmable sinusoidal signals or waveforms with a 12bit resolution DACs. In particular, concerning the sinusoidal signal functionality, that is of particular interest for the aim of this project, the DDS can generate 4 different sinusoids with the same frequency but different, and programmable,phase and amplitude. The registers, thus the different settings and parameters of the integrated circuit, can be programmed using a Serial Peripheral Interface (SPI) trough a microcontroller. A 24 bit register allows to set the tuning word of the DDS, which defines the output frequency of the sinusoids, with a resolution $\Delta f = \frac{f_{clk}}{2^{24}}$, where f_{clk} is the clock frequency,which is 80 MHz, leading to a Δf= 4.7 Hz. The clock source is an external 80 MHz crystal oscillator (540BAA80M0000BAG, Silicon Labs) which is AC-coupled to the differential clock inputs of the DDS with a Low-voltage differential signalling (LVDS) standard as shown on the left of Figure 3.10. The outputs of the integrated

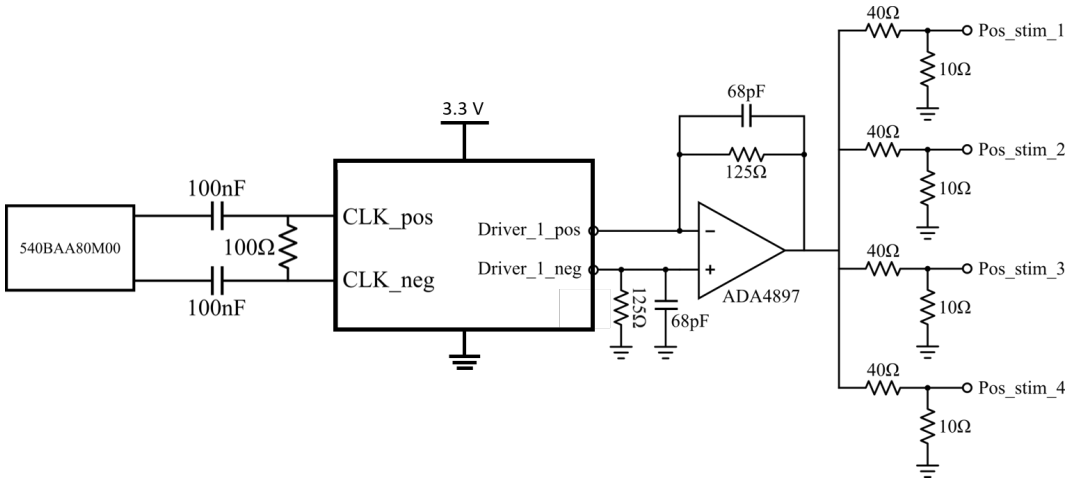

Figure 3.10: *Block diagram of the signal generation circuit.*

circuit are differential current signals (*Driver_1_pos* and *Driver_1_neg* in Figure 3.10) setted to have a 4 mA amplitude. Before applying said signals to the chip, they must be converted into single ended voltage signals and amplified. This is achieved by means of a TIA, implemented using an ADA4897 (Analog Devices), whose output is equal to: $V_{out} = 125\Omega \cdot (Driver\_1\_pos + Driver\_1\_neg)$. For clarity, said TIA will be addressed to as ItoV-TIA to distinguish it from the one used to measure the current

coming from the sensor.
As mentioned before the DDS signal amplitude is 4 mA which, multiplied by the amplifier gain of 125 V/Ω, generates a 500 mV voltage at the ItoV-TIA output.
Considering the possibility of having a short circuit due to fabrication errors of the sensor or fluid leakages on the contact pads, the output of the ItoV-TIA is not directly connected to the sensor but through four ideally independent resistive voltage dividers which decrease by a factor of five the sinusoidal voltage and ensure a minimum of 40Ω load at the output of the ItoV-TIA. Thus the final signal amplitude applied to the sensor is 100 mV, which is low enough to avoid red-ox reactions to occur at the electrodes surface. The ItoV-TIA and voltage divider circuit are replicated two times: one supplies all the measurement area simultaneously while the other all the reference areas; the two circuits are connected to different DAC outputs which generate two counter-phase sinusoids with the same frequency and tunable amplitude.
Note that an alternative viable option is to convert the differential current into a differential voltage and then applying one end to the measurement area and the other to the reference one, hence only using only one DDS output for both areas. In order to have the possibility to independently adjust and tune the voltages on the two areas, we decided to convert the differential current of each DDS output in a single ended voltage, hence exploiting two different outputs of the DDS for the two areas.
A third DDS output generates a signal identical to the one for the measurement area, which is amplified by a ItoV-TIA stage similar to the aforementioned one but with double gain. Thus, a 1 V amplitude signal is applied to the reference input of the multiplier.
All the three aforementioned ItoV-TIA have been designed in order to have a bandwidth greater than 20MHz.

Multiplexer. The central node of each of the four sensors is connected to a multiplexer. The choice of the most appropriate switch should be taken carefully for this application where the node to be switched is in contact with the liquid and therefore the switching may cause voltage transients due to the capacitances of the electrode-electrolyte system.
Single-pole double-throw switches are to be preferred as the inputs are not simply connected or not (floating) to the output, but each input can be connected to two different outputs.
Using this architecture the central node of the sensor can either be connected to the inverting input of the TIA, which is a virtual ground, or to ground when that sensor is not measured. Thus, the sensor is kept to same potential avoiding voltage transients during the scan of the sensors.
MAX4622 analog switches have been used for this purpose. Each IC contains two switches, allowing only two over the four sensors to be connected; thus two MAX4622 have been deployed on the board. The two ICs are easily controlled by two digital pins of Arduino Due.
Due to the slow varying signal expected, as the magnetophoretic capture of HCs, which are the particles with the highest $\Delta\chi$ considered in this study, takes place with a time constant in the order of 10^1 s, each sensor is sampled at 1 Hz frequency; thus the switches commutes every 250 ms.
Two important parameters in choosing the multiplexers are the *On-state resistance*, R_{on}

and the *On-state capacitance*, C_{on}. The former should be as low as possible in order not to increase significantly the total resistance, R_{tot} which would be detrimental for the resolution $\Delta R/R_{tot}$. The latter should also be minimized as every additional capacitance placed at the input of the TIA significantly affects its noise performances mostly at high frequency.
Unfortunately, decreasing one parameter increases the other. In addition to minimize the TIA noise given by C_{on}, we have selected switch with a C_{on} of the same order of magnitude (10^2 pF) of the sensor capacitance. The MAX4622 satisfies our requirement offering a R_{on} of only 3 Ω and a C_{on} of 150 pF.

Transimpedance amplifier. The output of the multiplexer is connected to the inverting input of a transimpedance amplifier which converts the input current, I_{in} coming from or to the sensor into a proportional voltage $V_{out} = I_{in} \cdot R_f$, where R_f is the feedback resistor of the TIA.
Thanks to its feedback, the non-inverting input is at virtual ground potential, thus the central node of the sensor connected to it is in turn at virtual ground.
Figure 3.11 shows the schematic of the TIA implemented using the AD8099, Analog Devices, ultralow noise Op-Amp. The two main aspects that have been taken into

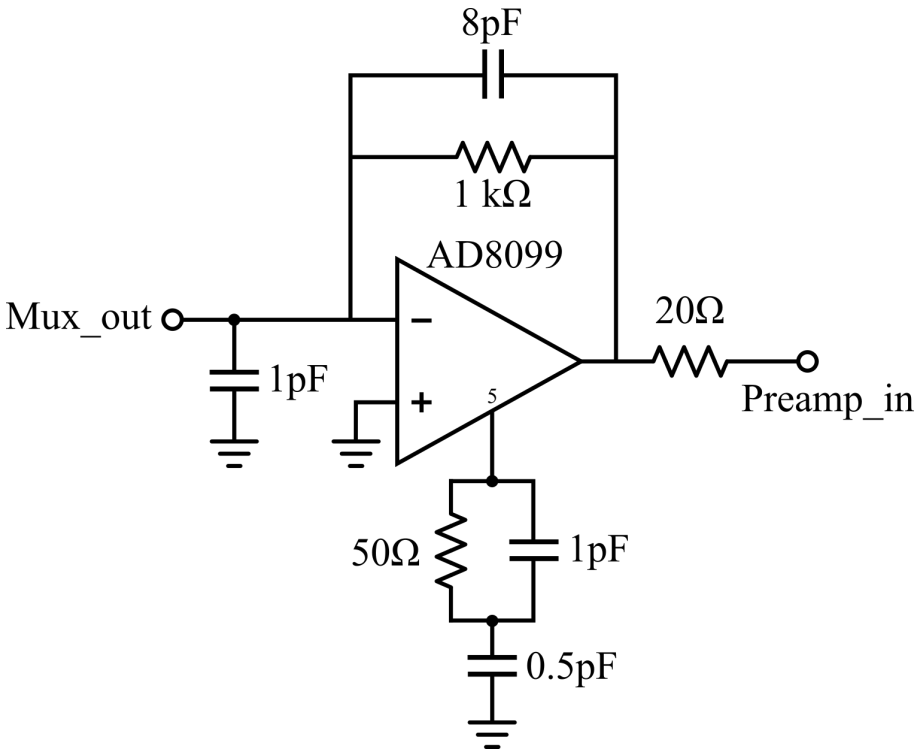

Figure 3.11: *Schematic implementation of the transimpedance amplifier and sizing of the components.*

account during the design and choice of the component for this stage are noise and stability.
Concerning the former, it should be lower than the unavoidable one given by the thermal noise of the sensor resistance itself, R_{sens}.
This resistance is given by the parallel of the two resistances representing the measurement and reference area, which, as discussed in the previous Section 3.3 are equal to

60 Ω. Thus the thermal noise given by the sensor is: $\frac{4KT}{R_{sensor}/2} = (23\frac{pA}{\sqrt{Hz}})^2$. Therefore the condition that must be satisfied by an appropriate choice of the Op-Amp and sizing of the components is

$$S_{(I,sensor)} > S_{I,OA} + \frac{4KT}{R_f} + \frac{S_{V,OA}}{(|Z_{eq}|)^2} \tag{3.15}$$

where $S_{(I,sensor)}$, $S_{I,OA}$, $S_{V,OA}$ are respectively the current noise introduced by the sensor, the one introduced by the Op-Amp and its voltage noise. Z_{eq} is the equivalent impedance seen by the virtual ground and, looking at the circuit in Figure 3.11, is given by Equation 3.16.

$$Z_{eq} = \frac{R_{sens}//R_f}{1 + s \cdot (C_{in} + C_f)(R_{sens}//R_f)} \tag{3.16}$$

C_{in} is the total capacitance at TIA input which includes several contributions:

- 150 pF of the on capacitance of the one multiplexer channel,
- 100 pF of the off capacitance of the three remaining multiplexer channels,
- 100 pF, approximately, the capacitance given by the sensor
- 1 pF the input capacitance of the Op-amp,
- approximately 10^1 pF given by the length connection path connecting the TIA input to the sensor,

for a total of 350-400 pF.
As can be noticed, the input capacitance of the chosen Op-Amp is negligible compared to the other contributions. Hence, the total TIA input capacitance is fixed by the sensor design ad multiplexer.
The sizing of the feedback resistor, R_f=1 kΩ, and capacitor, C_f = 8 pF, have been chosen in order to guarantee a 20 MHz bandwidth. In particular C_f has been chosen to be the lowest possible to increase the loop gain and the phase margin while R_f the highest in order to satisfy the bandwidth requirement, as their values affect the time constant of the pole $\tau_p = R_f C_f$.
Moreover, while their values does not affect the last noise term in Equation 3.15, an high value of R_f should be preferred in order to minimize the second-last one. Given the aforementioned values, it is possible to verify that the condition in Equation 3.15 is fulfilled as: $(23\frac{pA}{\sqrt{Hz}})^2 > (7.8\frac{pA}{\sqrt{Hz}})^2$.
A critical aspect is the stability of the TIA. For this extent, the reciprocal of the transfer function between the output of the Op-Amp and its input, through the feedback network, $1/\beta$, is given by:

$$1/\beta = \frac{R_{sensor} + R_f}{R_{sensor}} \cdot \frac{1 + s(C_{in} + C_f)(R_{sensor}//R_f)}{1 + sC_f R_f} \tag{3.17}$$

The $1/\beta$ gain shows a DC gain $G_{DC} = \frac{R_{sensor}+R_f}{R_{sensor}} \approx 0.1$ and an high frequency gain $G_{HF} \approx \frac{C_{in}+C_f}{C_f} \approx 38$. Thus, it shows a pole $f_p = \frac{1}{2\pi f C_f R_f} \approx 20$ MHz, and a zero $f_p \approx \frac{1}{2\pi f C_{in} R_{sensor}} = 4.5$ MHz.

The chosen Op-Amp have a GBWP= 3.8 GHz and a DC gain of 85 dB, thus the first pole is at $f_{p1,OA} = 213$ kHz and a second pole, which can be deduced from the datasheet of the component, at $f_{p1,OA} = 400$ MHz. The frequency at which the $1/\beta$ loop crosses the open loop gain of the Op-Amp is approximately f_x= 84 MHz. The phase margin can be assessed by:

$$\Phi_m \approx 90 - tg^{-1}(\frac{f_x}{f_z}) + tg^{-1}(\frac{f_x}{f_p}) - tg^{-1}(\frac{f_x}{f_{p2,OA}}) \tag{3.18}$$

which leads to a $\Phi_m \approx 65°$, thus assessing the stability of the feedback loop.
A 20 Ω resistor is also added to ensure the stability of the TIA for any capacitive loads it will be connected to.
The net realized for the compensation pin 5 of the AD8099, as shown in Figure 3.11, allows to slightly improve phase margin, thus the stability, decreasing the open-loop gain at high frequency.
In Figure 3.12 the experimental transfer function of the TIA, directly measured on the final board with E5061B Network Analyzer (Agilent Technologies), is shown. The stimulating signal has been applied to a 100Ω resistor (representing the 60 Ω sensor resistance and accounting for an extra 40 Ω given by the length of the gold tracks), which on the other end is connected to TIA input.
The in-band gain is approximately 6 V/V (15 dB), given by the 1 kΩ TIA feedback resistor divided by 150 Ω, which is the aforementioned resistor plus an additional 50 Ω given by the output of the Network analyzer.
Both the 20 MHz bandwidth and stability are satisfied.

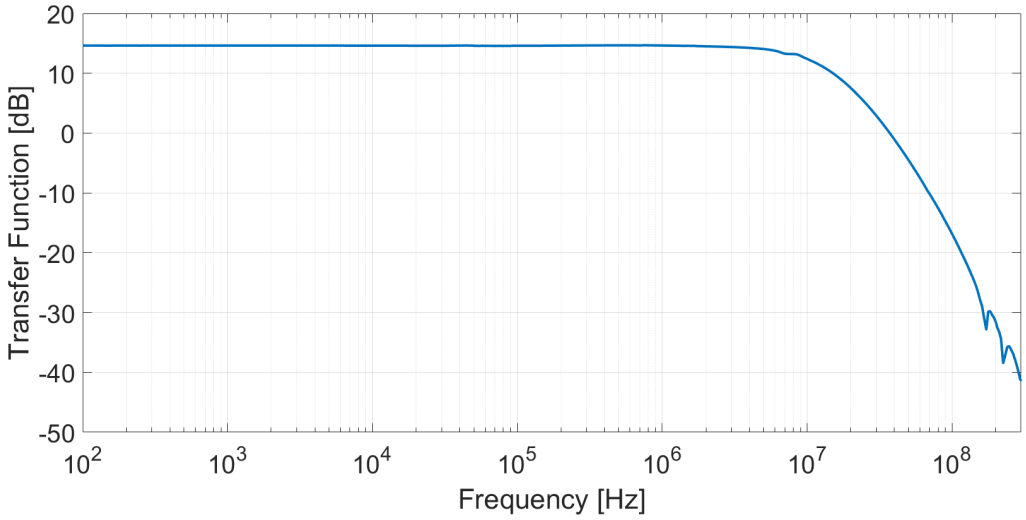

Figure 3.12: *Experimental transfer function of the TIA.*

Programmable gain amplifier. After the TIA, the signal is further amplified to compensate for the relevant noise contribution of the following analog multiplier (50 nV/$\sqrt{Hz}$). For this purpose a variable gain amplifier (PGA) has been preferred to maintain a certain degree of flexibility of the system, allowing to change the gain of the amplifier through digital pins driven by the microcontroller. However, this kind of ICs

usually show a worst noise performance, in respect to a fixed gain option.
The noise contribution of the PGA, commonly in the range of 10^1-10^2 nV/$\sqrt{Hz}$, should be compared with the 23 nV/$\sqrt{Hz}$ at the output of the TIA.
Thus, THS7001 by Texas Instruments, has been chosen for this purpose as it provides both a low noise preamplifier and a PGA (with selectable gain from 0.08 to 10V/V). In particular the preamplifier exhibit a 1.7 nV/$\sqrt{Hz}$ at its input, which is negligible in respect to the one already present at the TIA output, and its gain can be setted through external resistors.
A gain of 5 has been setted for the preamplifier, thus the noise at the output of preamplifier is 115 nV/$\sqrt{Hz}$, which is now enough to be dominant in respect to the one of the PGA. The latter indeed shows a noise of 10 nV/$\sqrt{Hz}$ for the maximum gain (10 V/V) and 500 nV/$\sqrt{Hz}$ for the minimum one (0.08 V/V).
However, as attenuation will not be used, the minimum gain to consider is 1.26 V/V which shows a noise equal to 50 nV/$\sqrt{Hz}$. Thus, even in the worst case scenario, i.e. minimum amplifying PGA gain, the dominant noise source is the one due to the sensor. Hence, the total noise, only considering the thermal contribution of R_{sensor}, at the output of this amplification stage is comprised between 140 and 1150 nV/$\sqrt{Hz}$ depending on the gain.
Concerning the bandwidth, the preamplifier, considering its GBWP = 100 MHz and 5 V/V gain, ensures a 20 MHz bandwidth for all the PGA gains, according to the THS7001 datasheet. In order to deal with DC non idealities arising from all the amplifiers offsets of the measurement chain, a CR highpass filter has been implemented at the output of the PGA. Due to the 20 Ω output resistance of the PGA, to ensure an appropriate impedance matching between the two stages, a 200 Ω resistor has been chosen for the filter while C has been set to 1 μF.
The transfer function of all the measurement chain up to this point (i.e from TIA input to the HPF output) have been measured directly on the final board with E5061B Network Analyzer (Agilent Technologies), connecting, as previously, a 100 Ω resistor between the output of the instrument and TIA input.
The results are shown in Figure 3.13 in which the different curves represent the transfer function at different PGA gains. At low frequency it is clearly visible the filtering effect of the HPF defining a pole at 800 kHz according to the time constant defined by the CR= 1μF·200Ω. At higher frequencies the gains reflect the expected ones as well as the bandwidth of 20 MHz.
Also the noise power spectral density has been measured experimentally on the board with N9020A MXA Signal Analyzer (Agilent Technologies).
The results are reported in Figure 3.14 for both the maximum PGA gain (10 V/V, blue line) and the minimum one (1.26 V/V, red line). The white noise around the frequencies of interest (i.e. around 1 MHz, the frequency at which both the stimulus signal and the demodulation take place) is approximately equal to 1600 nV/$\sqrt{Hz}$ for the maximum PGA gain and 200 nV/$\sqrt{Hz}$ fo the minimum one. These values are slightly higher than the one obtained, and declared previously in this Section, only considering the dominant thermal noise of the sensor resistance, which were between 140 and 1150 nV/$\sqrt{Hz}$ for the minimum and maximum PGA gain respectively. This small increment is, however, in line with the neglected noise sources and can still be considered acceptable.

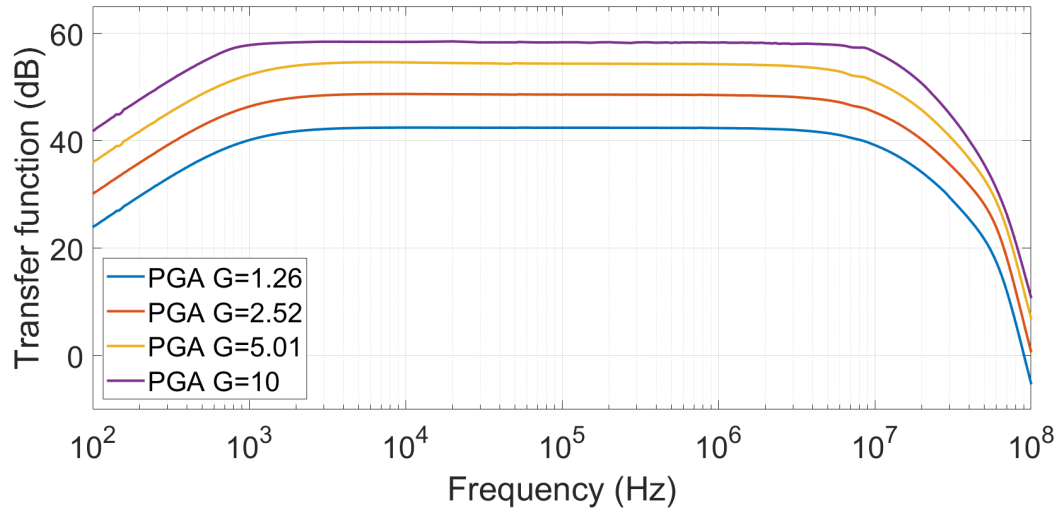

Figure 3.13: *Experimental transfer function of the measurement chain from TIA input to HPF output as a function of the PGA gain.*

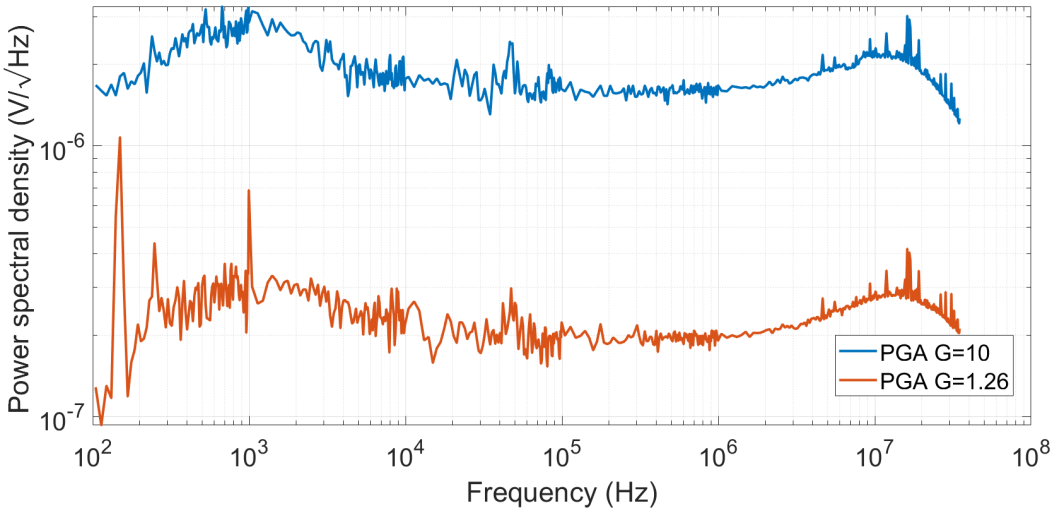

Figure 3.14: *Noise spectral density of the measurement chain from TIA input to HPF output as a function of the PGA gain.*

Analog multiplier. In order to perform the analog multiplication an AD835 by Analog Devices has been chosen. Thanks to the preamplifier and the PGA stage the signal noise is also dominant in respect to the 50 nV/$\sqrt{Hz}$ introduced by the multiplier.
AD835 multiplies the signal coming from the sensor by the 1V reference sinusoid generated by the DDS; the result of this operation is given by Equation 3.14.
A third input can be used to sum a voltage to the multiplication outcome. This option is very useful to adapt the output range of the multiplier to the one of the ADC. As a matter of facts, the input range of the multiplier is ± 1 V, thus a maximum signal amplitude of 1 V resulting from the multiplication operation can be obtained at its output.

However the output range of the AD835 is ±2 V.Connecting the summing input of the multiplier to a 1 V voltage reference (ADR130, Analog Devices) the output signal is shifted up by 1 V covering the range 0-2 V.
From a noise point of view, the multiplication operation halve the noise, as the white noise have random phase, thus its power split between in phase and quadrature. However the signal is halved in amplitude accordingly to Equation 3.14, thus in the end the signal to noise ratio is worsened by a factor $\sqrt{2}$.

Lowpass filter. A lowpass filter is now needed to remove the twice frequency component of the signal, which arises from the multiplication, as well as all the noise contributions outside a certain frequency window centered around DC, where the useful signal lies.
The 3^{rd} order active Sellen-Key cell [104], implementing a Chebyshev filter, shown in Figure 3.15 has been adopted for this purpose. The configuration and component

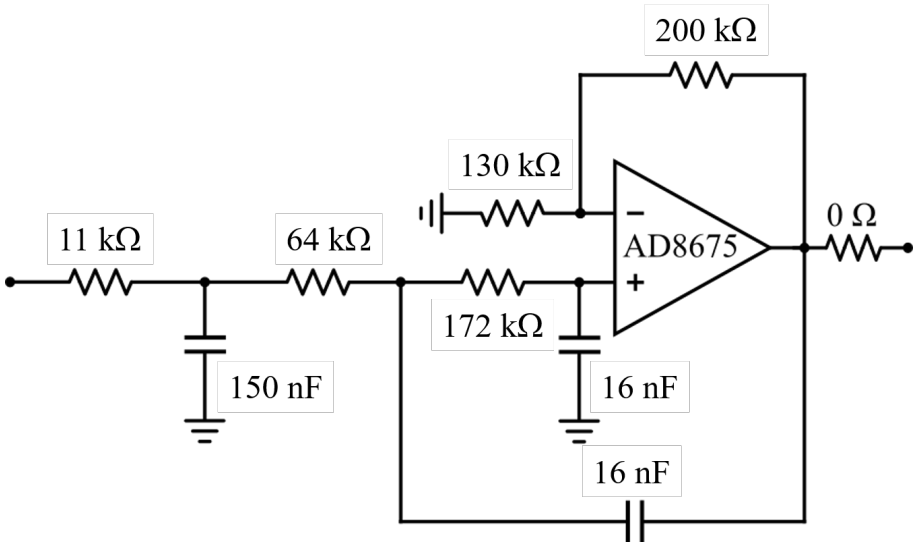

Figure 3.15: *Schematic implementation of the 3^{r}d order Sallen-Key cell implementing the lowpass filter.*

sizing reported in Figure 3.15 sets the pole of the filter at 100 Hz, obtaining a -160 dB attenuation in the MHz range, which is the frequency of the stimulus and its harmonics. The transfer function of this configuration has been simulated and the result is shown in Figure 3.16.
As can be noticed, the high frequency attenuation of the filter stops at -160 dB due to the output resistance of the operational amplifier. The filter is also used to amplify the input signal by a factor of 2.5. In this way, the 2 V signal range coming from the multiplier is expanded to 5 V in order to completely cover the following ADC input dynamic range.

ADC. At last, in order to convert the analog signal into a digital one, an AD7680 (Analog Devices) 16 bit SAR ADC has been used. First of all it is necessary to asses the adequacy of the number of bits for our purposes. To do so, lets consider the current signal ΔI at the input of the TIA due to a $\Delta R/R_{sens}$=10^{-4}, which correspond to the resolution limit of EIS in liquid. From Equation 3.12 it is possible to obtain this quan-

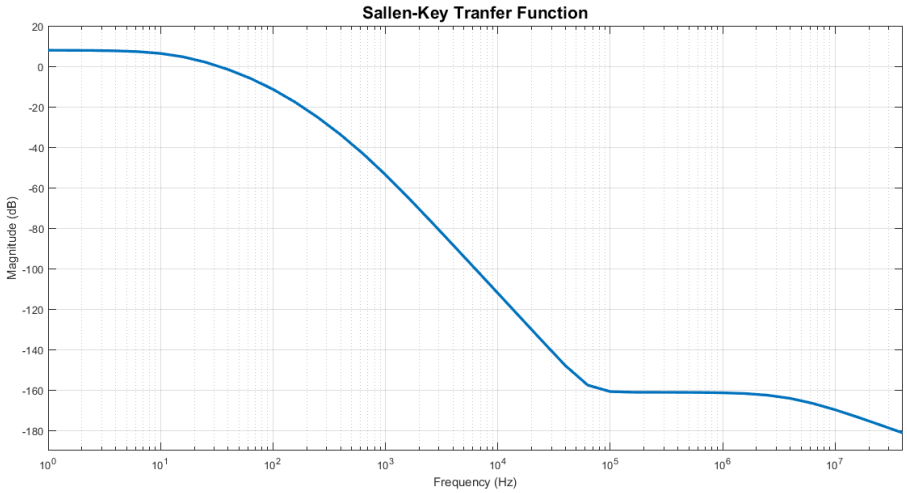

Figure 3.16: *Simulated transfer function of the 3^{r}d order Sallen-Key cell.*

tity which is 0.1 μA. Now, the corresponding voltage at the ADC input can be deduced multiplying the ΔI by the gains of the TIA, Preamp, PGA (minimum gain) and LPF.
The minimum signal that the ADC should be properly digitalize is 1.5 mV which is more than one order of magnitude higher than the LSB=76 μV.
The result of the conversion can be easily read by the Arduino microcontroller trough SPI communication protocol. The chosen ADC performs the conversion on demand, which means that the microcontroller is responsible to start the conversion. The maximum throughput rate of the ADC is 100 kSamples per seconds, which looks oversized given the aforementioned switching frequency of the multiplexer equal to 4 Hz where every sensor is sampled once per second. The reason behind the relatively high throughput rate resides in oversampling. Multiple samples will be acquired between each sensor commuting and then they will be averaged in order to obtain one single sample. In this way it is possible to improve the SNR by a factor $\sqrt{N}$, which depends on the sampling frequency, f_s and the frequency content of the signal f_{signal} according to the relation $N = \frac{f_s}{2f_{signal}}$.
Considering the signal frequency of 100 Hz, due to the lowpass filter, and to sample the signal at 10 kHz, it follows that N= 50 thus the signal to noise ratio increases by a factor 7.
Thanks to oversampling also the resolution of the conversion increases by n bits according to $n = log_2(n_{samples})/2$ where $n_{samples}$ is the number of samples that are averaged to create each sample. Thus, averaging 2000 samples the resolution of the conversion can be increased by 5 bits.

Microcontroller. The digitized data are then transferred to a microcontroller (Arduino Due) trough SPI communication.
Arduino Due is a microcontroller board featuring an 84 MHz 32-bit ARM core (Atmel SAM3X8E ARM Cortex-M3). It offers 54 digital input/output pins, 12 analog input and 2 analog output at 12 bit; it can be supplied with 7-12 V while it operates at 3.3 V. The available memory is composed by 512 KB of flash memory and 96 KB of SRAM.

Besides reading the sampled data from the ADC it is also responsible for transferring them to a PC trough USB communication as well as programming the DDS registers, managing the switching timing of the multiplexers and setting the PGA gain.
Arduino Due is a 101x53 mm^2 board that will be mounted beneath the electronic board by means of trough hole pins.
For a detailed description of the firmware of the microcontroller, as well as the custom software running on the PC receiving the data, see Section 4.4.

Power supply. The board is supplied by an external AC-DC transformer (HAA15-0.8-AG, Bel Power Solution), connected to the 240 V 50 Hz mains supply, which supplies the board with a $\pm$ 12 V and a current of 1 A for the positive supply and 0.4 A for the negative one.
The voltage coming from the transformer is then regulated on the board by linear voltage regulators (see Figure 3.17) in order to obtain $\pm$5 V and two separated 3.3 V voltages for the digital part of the circuit and the analog part.
All the regulators, as well as the power supply, have been chosen linear as they offer better noise performances in respect to their switching counterparts. Moreover, the TO220 package has been selected for all the on-board regulators in order to guarantee a good heat dissipation avoiding to overheat them especially as the board is meant to work in medium high temperature environments like Africa.
MC7805 and MC7905 linear voltage regulators by On Semiconductor have been exploited to generate respectively the positive and negative 5 V, while two separated UA78M33 by Texas Instruments to regulate the 3.3 V that supply the digital circuity and the one for the analog part.

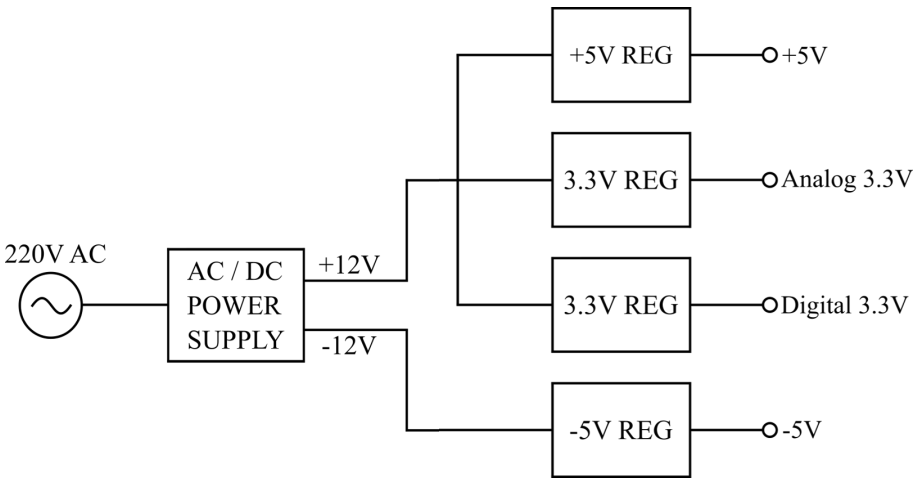

Figure 3.17: *Scheme of the power supply voltages.*

Board fabrication. The board has been fabricated by Millennium Dataware srl. on a 1.6 mm thick 4 layer FR4 Panasonic substrate 120x100 mm.
In Figure 3.18(A to D) the layout, from the top layer to the bottom one, of the 4 layers PCB designed using Altium Designer software are shown.
In particular they mainly contain, (A) the analog connections, (B) the ground plane, (C) the power planes and (D) the digital lines and the connection from/to the microcon-

troller. In Figure 3.18(E) a photo of the board is shown.
In order to connect the board to the chip, the former can be connected to an external

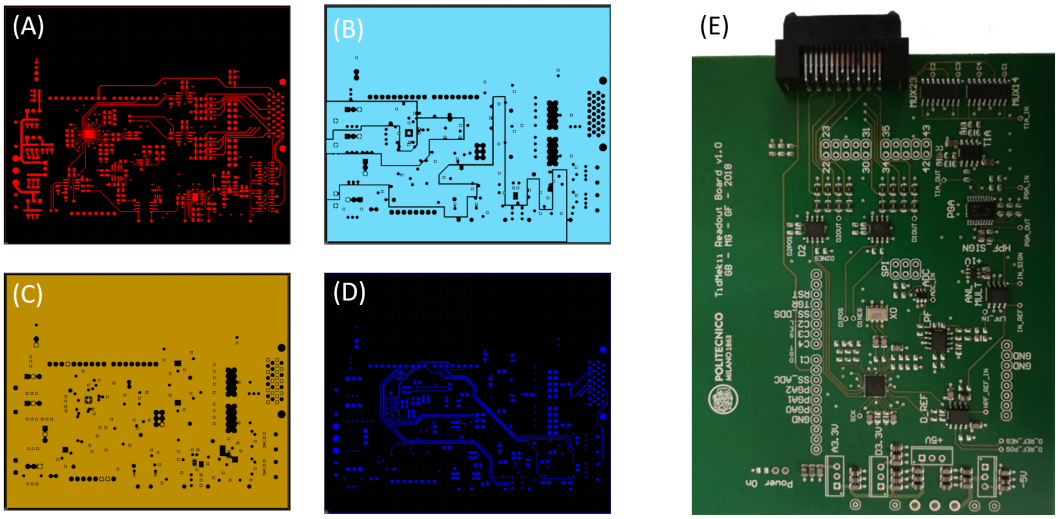

Figure 3.18: *Layout images of the board. (A) Top layer containing the analog connections, (B) Top-mid layer containing the ground plane, (C) Bottom-mid layer containing the power planes and (D) Bottom layer containing the digital lines and the connection from/to the microcontroller. (E) Photograph of the fabricated board.*

PCB, which, by means of spring contacts, is in turn connected to the latter, trough a board-to-board connector (TX25-30P-LT-H1E on the electronic PCB side and TX24-30R-LT-H1E on the chip PCB side).
A Further description about this topic and the chip PCB is provided in Section 4.2.

CHAPTER 4

Fabrication, protocols and practical considerations

4.1 Chip Fabrication

The chip has been fabricated in PoliFab, the centre for micro- and nano-fabrication of the Politecnico di Milano, a 370 m^2 ISO-06 clean-room.
The fabrication process, as well as the chip structure, can be divided in two parts/layers: the so-called magnetic layer, in which the Ni pillars are embedded into the silicon substrate and, on top of that, the electric layer, in which the gold electrodes are fabricated onto the substrate surface.
The process flow of both layers is schematically represented in Figure 4.1.
In order to fabricate the first layer, a 500 μm thick heavily p-doped silicon substrate (P+/Boron - 0.005-0.025 Ω·cm, 4" wafer from Si-Mat) is used.
Before the use, the wafer is cleaned for 5 minutes by means of ultrasonic cleaning bath in acetone at 52 kHz. Then it is rinsed in Isopropyl alcohol for few seconds, dried with N_2 gas and baked on an hot plate at 120°C for 10 min to completely dry the surface.
A first photolithographic step is needed to create the mask, made with photoresist, for the following etching of cylindrical cavities in the substrate where the Ni pillars will be fabricated. As soon as the wafer cool down to ambient temperature, it is coated with a 20 μm thick positive photoresist (AZ40XT, MicroChemicals) through spin coating technique. A Karl Süss RC8 spin coater has been setted to spin at the target speed of 2700 rpm for 45 s, reached with an acceleration of 500 rpm/s.
A thick photoresist, as it will be shown below, is needed as it will be partially etched during the Reactive Ion Etching step, in which holes in the substrate will be etched, and the remaining layer of photoresist should be thick enough to act as a mask for a the consequent Ni deposition step.

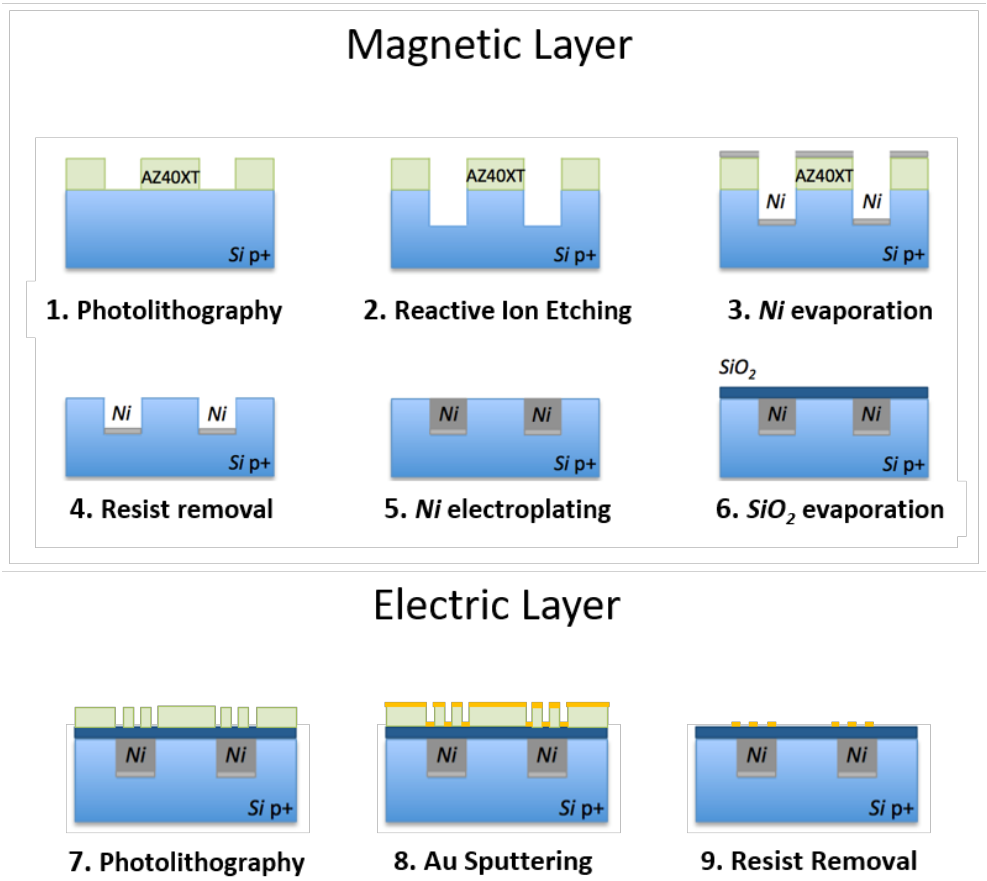

Figure 4.1: *Scheme of the process workflow for the device fabrication.*

Subsequently the substrate is put on a hot plate in order to evaporate the solvent part of the photoresist. Due to the high thickness of the photoresist, the hot plate temperature is linearly ramped up from 40°C to 120°C for 5 minutes and then kept at the final temperature for 2 minutes, in order to allow the solvent from the lower layers of the photoresist to evaporate without remaining stuck by the external ones that solidifies quicker if exposed to a sufficiently high temperature. An inappropriate baking of this photoresist leads to the formation of foam, caused by the evaporation of the solvent from the lower layers which, being unable to leave the material, expand, creating bubbles.
After letting to dry the substrate at room temperature, the photoresist is ready to be exposed. The pattern of the pillars is transferred to the photosensitive material using a laser writer (Heidelberg MLA 100) provided with a LED UV source at 365 nm wavelength. Starting from the CAD drawings, due to the positive nature of the photoresist, only the areas of the pillars are exposed by the laser writer with a 320 mJ/cm^2 dose.
After the exposure, the substrate is baked at 105°C for 100 s and then is let to cool down slowly at room temperature for 15 min in order to avoid creation of internal stresses in the photoresist which would cause it to crack.
The wafer is then developed rinsing it into the developer (AZ726MIF MicroChemicals) for 120 sec and, after, in pure water for few seconds. The former step allows to remove only the photoresist areas exposed to UV lights, thus 40 μm diamater and 20 μm deep

cylindrical holes are obtained on the photoresist in the areas where the Ni pillars will be fabricated.
The photoresist can be then seen as a physical mask for the following step in which 20 μm deep cavities are etched in silicon, which will host the Ni pillars, where its surface is uncovered by the photoresist.
In order to etch said holes inside the substrate with steep side walls, Reactive Ion Etching (RIE) process has been used. In particular a Bosch-like process using both SF_6 and C_4F_8 gasses has been exploited on a Oxford Plasmalab 100 inductively coupled plasma RIE (ICP-RIE).
A Bosch process consists in alternating etching and passivation phases. During the former, the substrate is etched mainly in the direction perpendicular to the substrate but also in other directions in a lesser extent; this step is performed using SF_6 gas (see Figure 4.2(A)). The passivation phase, on the other hand, is used to create a fluorocarbon film inside the etched cavities which protects the side walls of the cavities during the following etch step; this step is performed using C_4F_8 gas. Thanks to the multiple repetition of these two steps, high aspect ratio vertical walls can be achieved. In order to etch 20 μm deep cavities, 12 s of etching phase and 7 s of passivation phase have been repeated 160 times using a 2.4 MHz RF power at 2500 W.
In Figure 4.2(B), a Scanning Electron Microscope (SEM) image of a cylindrical hole etched with this process is shown.

A 20μm thick photoresist has been chosen as a mask for this process to take into account the not ideal selectivity of the etching which cause a partial etching of the photoresist itself. Moreover, the same photoresist mask is used to deposit a thin layer of Nickel only on the bottom of the cavities, which will be d as seed layer for their complete filling with Ni through electroplating technique. A 30 nm thick Ni layer is deposited on the substrate by means of evaporation (Evatec BAK640 E-beam Evaporator) with a vacuum pressure of 10^{-5} Pa and 0.1 nm/s deposition rate.
Following the deposition, a lift-off step is carried out in order to remove the photoresist mask and the Ni deposited on top while leaving it only in the holes bottom. For the lift-off process, the wafer is rinsed in acetone in a 52 kHz ultrasonic bath for 10 min and then rinsed and dried in isopropyl alcohol and N_2 respectively.
Once obtained the holes, they can be filled with Nickel, thus forming the magnetic Ni pillars. The only technique available to deposit metals with a 20 μm thickness is electroplating.
Electroplating is an electric field driven deposition technique in which the metal ions, solved in a solution, are driven to deposit on the sample (cathode), and are replenished into the solution by an anode made of the same material of the one deposited.
A potential difference between the anode and cathode is applied. In particular, being nickel ions positives (Ni^+), an higher voltage is applied to the Nichel electrode and a lower one to the sample. A current flow is generated due to the displacement of said ions in the solution. The deposition takes place on the sample surface and the rate of deposition depends on the local potential and distance from the anode. In order to apply an uniform electric potential directly to the sample, an highly p-doped silicon wafer, thus with low resistivity, has been used as the chip substrate. Moreover, the thin Ni layer deposited in the bottom of the cylindrical holes act as a seed layer for the deposition to occur preferably starting in and from their bottom. The deposition outside

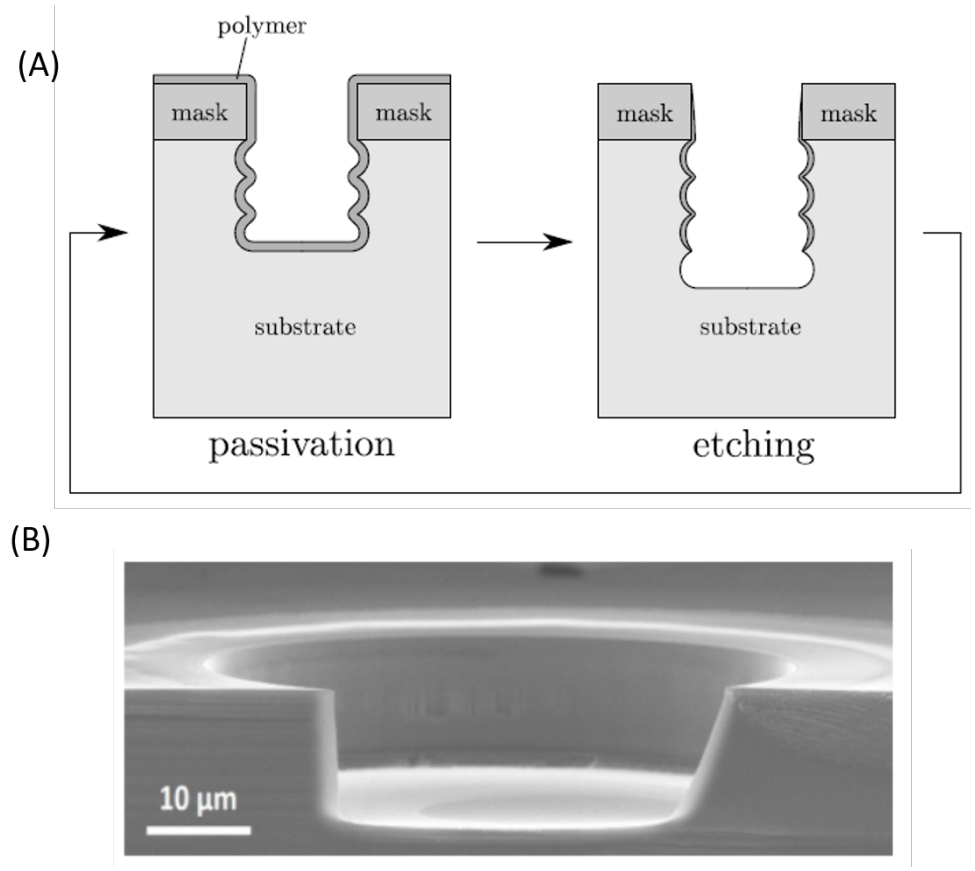

Figure 4.2: *(A) Schematic working principle and effects of a Bosch process. (B) SEM image of the 20 µm deep cavities etched through Bosch process.*

the cavities, i.e. on the silicon surface, is prevented by the insulating native oxide layer (SiO_2) formed on its surface, acting as an electric shielding.
The potential is applied to the sample trough a metal ring in contact to the periphery of the substrate. The wafer is held in a 4" wafer holder made in PMMA that covers the back of the substrate as well as the metal ring.
The substrate holder is part of the electroplating kit *B-92-WF-PPM1-T01 20L Overflow Plating Set* furnished by Yamamoto MS. The solution used for the electroplating is Nickel Sulfamate from Atotech which is kept at a constant temperature of 50°C during the deposition. Both cathode and anode are connected to an external current generator (Agilent-6614C) which imposes a constant current density of 8 mA/cm^2 to flow between the two. The current density value has been extracted from the datasheet of the solution. The deposition rate, T/t (μm/h), can be either deduced from the datasheet or by:

$$T/t = \frac{w}{n\rho F} j \tag{4.1}$$

where w, n, ρ are, respectively, the atomic weight, oxidation number and density of the material to be deposited; F the Faraday constant and j the current density.
For Nickel w=58.7 g/mol, n=2 eq/mol and ρ=8.9 g/cm^3 a deposition rate of 9.7 μm/h can be obtained from the Equation 4.1 considering the aforementioned current density. Thus, the deposition is continued for more than 2 hours.

As can be seen from Figure 4.3(A,B) an even filling of the cavities is difficult to be obtained as the filling of each hole depends on many factors like the quality of the seed layer, the presence of air bubbles trapped in the cavities and fabrication non idealities.
Thus, the deposition is protracted until a 3-8 μm excess of Ni is deposited creating a

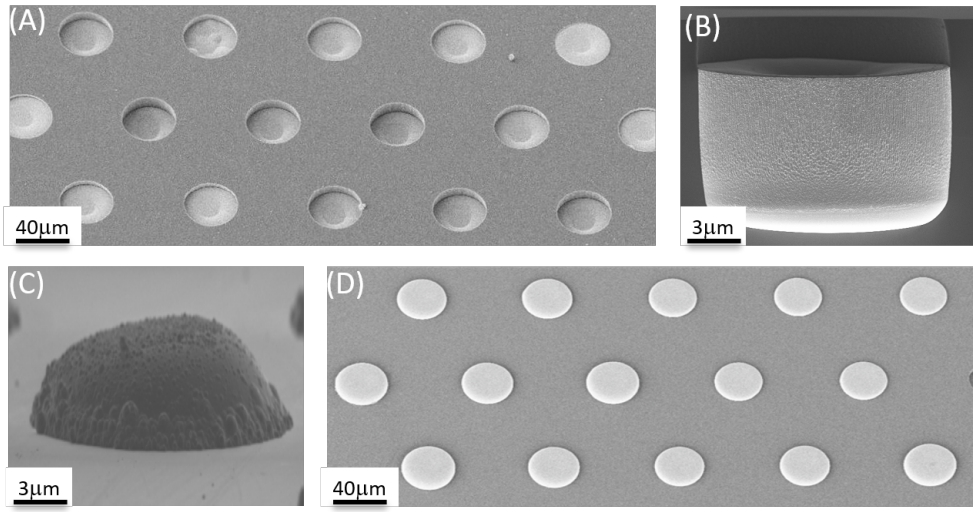

Figure 4.3: *SEM images of the Ni pillars electroplated inside the silicon cavities. (A) Top view of the pillars showing an uneven filling of the cavities. (B) Sectioned side view of a pillar inside its cavity. (C-D) Side and top view, respectively, showing the result of excess Ni deposition.*

"cupcake" like structure as shown in Figure 4.3(C). The excess of Ni is then polished to obtain a flat surface which is required by the electrical layer.
In order to polish the surface, a *Seikoh Giken sfp-550 optic polisher* has been exploited. A 3 μm roughness sandpaper is used for 30 minutes using water as lubricant followed by 10 min using a polishing cloth with a 0.25 μm diamond suspension and finally 10 min with 0.1 μ diamond suspension.
The obtained surface presents a 50-100 nm roughness, which is low enough for the fabrication of the electrical layer, also considering that a SiO_2 layer will be deposited on top of said surface lowering its overall roughness. A 3 μm thick silicon dioxide layer is then deposited on the sample in order to electrically insulate the magnetic layer from the electrical layer and thick enough to significantly reduce the induction of currents trough the substrate.
The deposition of this layer is achieved in two steps: a first 50 nm silicon dioxide layer is deposited trough evaporation and the following 3 μm using plasma enhanced chemical vapor deposition (PECVD) using a STS Muliplex. The former step is required as PECVD deposition depends on the local properties of the surface, thus given the different materials composing it (i.e. silicon and Nickel), the resulting deposited layer would be uneven.
The first layer, the magnetic one, is therefore complete and it is possible to proceed with the electric one.
In order to fabricate the electrodes, a first optical lithography step is required to define the electrodes pattern on a photoresist which will act as a mask for the deposition of the electrodes material, i.e. gold.

Before depositing the photoresist, the substrate is coated with a Ti-Prime layer (MicroChemicals), acting as adhesion promoter, through spin coating at 6000 rpm for 60s, and then baked for 120 s at 120°C. After this intermediate step a 1.6 μm thick image reversal photoresist (AZ5214E, MicroChemicals) is spin coated at 6000 rpm for 60s with an acceleration of 500 rpm/s.
AZ5214E is an image reversal photoresist which means that it can be used both as a positive or negative one. Its behaviour depends on the process steps it is subjected to. For the purpose of this fabrication step a negative photoresist is to prefer due to the undercut profile that can be obtained, which is recommended for the subsequent lift-off step. Thus, the AZ5214E process steps here reported are the one needed to obtain a negative behaviour of the photoresist.
After spin coating, the substrate is baked at 110 °C for 90 s and then the areas outside the electrodes are exposed with 35 mJ/cm^2 UV light using laser writer.
Another bake step is required, after the exposure, at 115°C for 90 s.
Finally all the substrate surface should be exposed to 250 mJ/cm^2 UV light. This step has been performed using Karl Süss Mask Aligner MA6. It is now possible to proceed with the development, rinsing the substrate into the developer AZ726MIF for 20 s and then into water for few seconds. During this last step, all the unexposed areas of the photoresist are removed, thus the substrate is left uncovered by it only in the areas where the electrodes will be.
The sample is now ready for the deposition of gold.
Before of that, the sample is etched for a 10 min with a plasma at 200 Watt in order to remove and clean the surface from an eventual nanometric residual layer of undeveloped photoresist.
The gold deposition is performed using a magnetron sputtering (Leybold LH Z400).
In order to promote the gold adhesion to the substrate, a 30 nm Cr layer, used as adhesion layer, is deposited before the 200 nm Au layer. The Cr deposition takes place at vacuum pressure of $2{\cdot}10^{-2}$ mbar, Ar gas flow of 70 Standard Centimeters Cube per Minute (SCCM), a 50 W power between the anode and cathode and a deposition rate of 26 nm/min.
The Au deposition, which starts immediately after the previous, as the sputtering system has both the Au and Cr targets inside the chambers, is performed at $1.8{\cdot}10^{-2}$ mbar, 100W and a deposition rate of 28.5 nm/min.
In the end a lift-off process, like the one used for the AZ40XT, allows to remove the photoresist and the metal deposited on top of it, leaving only the metal constituting the electrodes.
Figure 4.4 shows (A) the image of the complete chip and in (B) and (C) respectively the measurement ad reference electrodes.

4.2 Setup

In order to perform the experiments in the most reproducible and automated way possible, a mechanical and electronic setup has been designed. Moreover, as the final goal of the project is to test and use the device in the hospitals, where then the final user is a clinician, the entire setup system has been designed in order to be easy of use and user friendly.

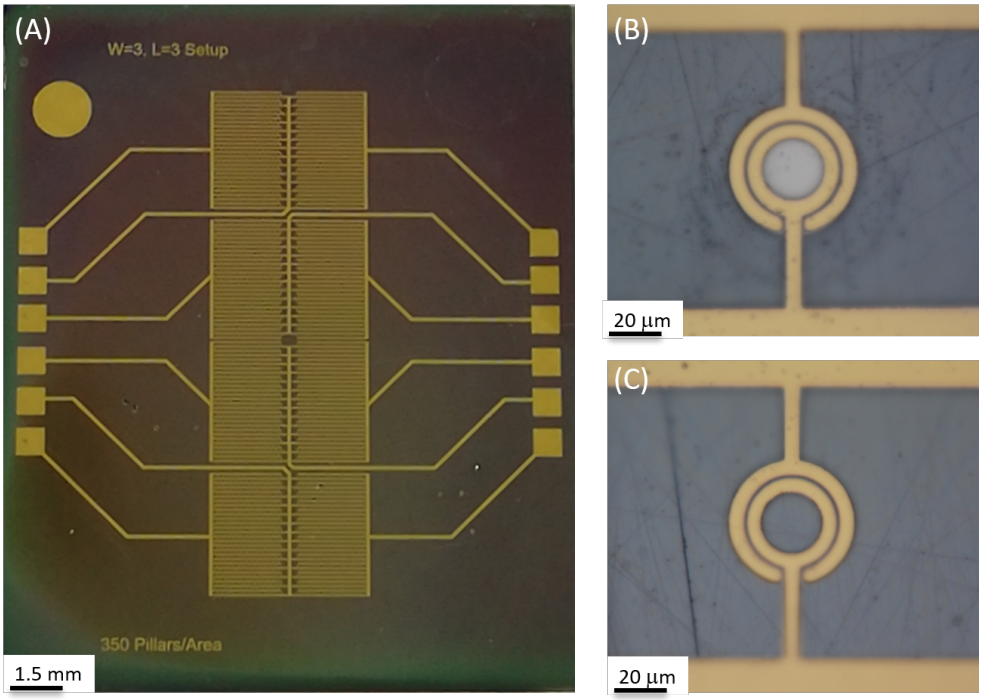

Figure 4.4: *Images of the fabricated chip. (A) Photo of the entire chip, (B) and (C) Microscope images of one sensing electrode of the measurement and reference area respectively.*

The setup is composed by a cartridge, where the chip and the glass slide and the gasket are placed, the electronic board, a stepper motor to move the magnet assembly and a mechanical structure to keep all the aforementioned parts in the right position in respect to each other and finally a portable power supply and a PC.

Cartridge. The cartridge performs several important and fundamental functions. It allows to easily place and keep in position both the chip and the glass slide, on top of which a confinement ring is fabricated. It also makes the electrical connections to the chip and bring them to the electronic board. Moreover, it allows to put in contact, in a practical way, the chip with the glass slide, on which the blood sample to analyse is poured, creating the chip-gasket-glass slide assembly and thus defining the microfluidic chamber.
An image of the cartridge is given in Figure 4.5, in which all the main components that are going to be described are highlighted.
The cartridge is composed by two parts, a plastic mechanical structure and a PCB. The former, designed using AutoCAD and fabricated by 3D printing, has a lid where the chip can be inserted and placed in the correct position thanks to two lateral rails and an end run stop. The lid support only the sides of the chip, leaving its back uncovered, in order to allow the magnet to be positioned in close contact to the chip backplane.
A thin U-shaped copper foil is put between the lid and the chip where they are in contact. The copper foil, connected to ground, is used to connect the backplane of the chip, where a 100 nm of gold have been deposited, to ground. In this way the substrate of the chip is connected to ground and some parasitic current paths in the substrate are redirected to ground instead of being read by the TIA.

The lid is connected to the cartridge base trough a pivot on one of his side, allowing its rotation around said side, as shown by the curved arrow in Figure 4.5. The base has a recess for the positioning of the glass slide and a hole beneath it, which is used to assess the correct positioning and presence of bubbles in the fluid after the sealing between the chip and the glass slide has been done.
Two narrow rectangular holes, next to the glass slide housing, allow the passage of the spring contacts trough the base. Beneath the base there is a PCB, kept together to the

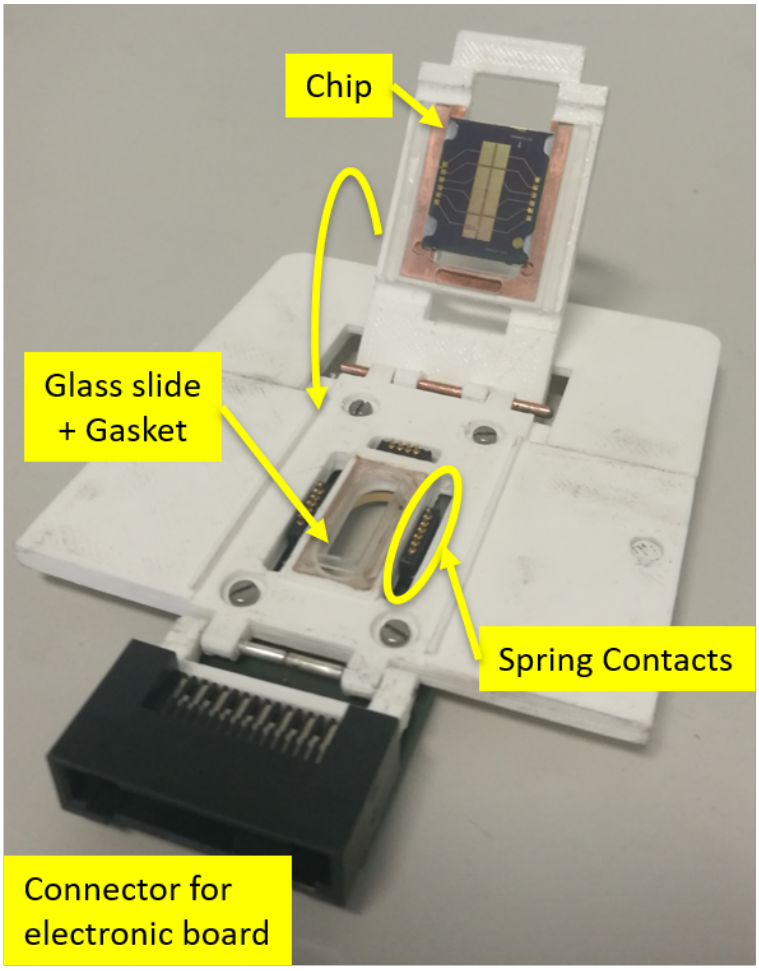

Figure 4.5: *Photo of the cartridge with main parts highlighted.*

former by means of four M2 bolts.
The PCB has been fabricated by Millennium Dataware on a 4 layers FR4 substrate. In Figure 4.6 the layout of all the layers of the board (A) and its 3D representation (B) are shown.
Two sets of six spring contacts (Mill-Max 854-22-006-10) and a board-to-board connector (TX25-30P-LT-H1E, JAE Electronics) are soldered on the board. The formers allow to link the pads on the chip to the cartridge PCB, where several tracks bring the connection to the board-to-board connector, which in turn can be connected to its complementary socket soldered on the electronic board.
The tracks bringing the signals from the chip to the connector, and vice versa, travels

only in the two internal layers, while external ones are ground plane thus shielding the signals from interferences like a Faraday's cage. A third set of four spring contacts is used to bring the ground contact to the copper foil.

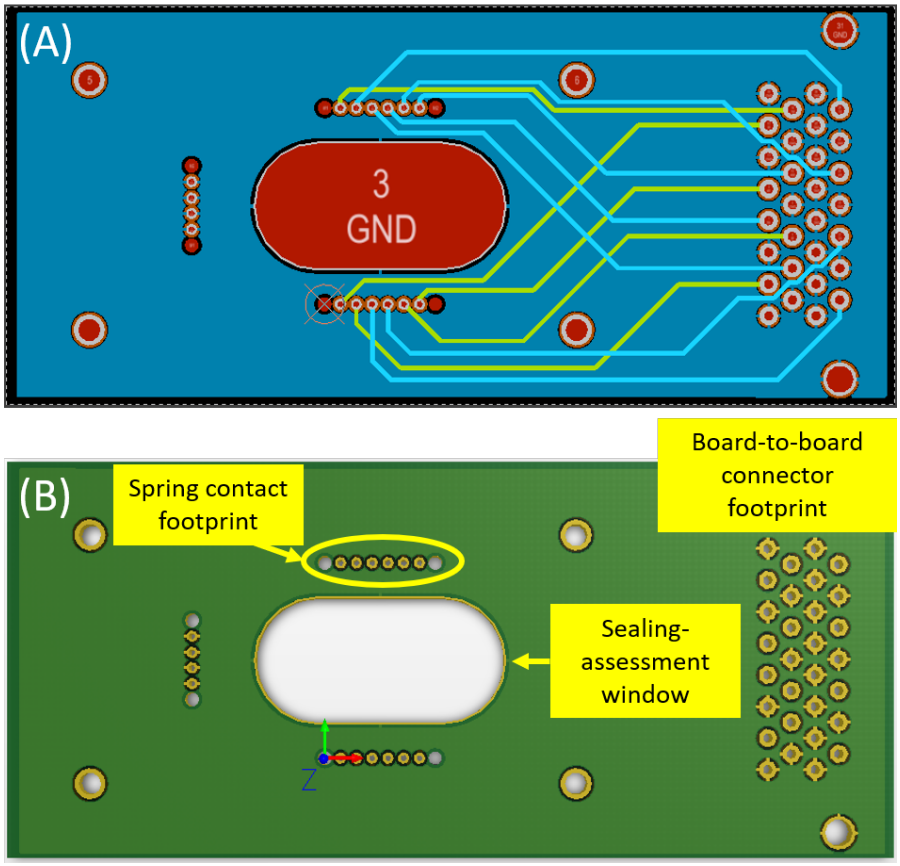

Figure 4.6: *Images of the cartridge PCB. (A) Top view of all the PCB layers, blue plane is the top layer, blue tracks are in the intermediate-top, light blue ones in the intermediate-bottom while the bottom layer, being identical to the top layer is not visible as completely covered by it. (B) 3D view of the PCB*

Electronic board. The electronic board, as described in Section 3.4, provides the stimuli to the sensor and performs the low noise readout and amplification of the analog signal coming from it, digitalizes, processes and sends the data to a PC.
The electronic board and the Arduino Due, mounted beneath it, are inserted in a 120x100x53 mm^3 aluminium box (1455N1201, Hammond Manufacturing), which is connected to the ground, thus acting as a Faraday's cage shielding its content from environmental noise and disturbances.
The board communicates to the outside and vice versa trough three connectors: a 3 poles DIN, a micro-usb and a board-to-board connectors. The former is used to connect the board to the external power supply, the second one to program or communicate with Arduino Due through PC and the latter to plug in the cartridge.

Stepper motor and magnet assembly. A stepper motor is used to precisely bring the magnet close to the back of the chip or away from it. For this purpose an L406-

20SD00L stepper motor by Physik Instrumente with single axis movement and 5.2 cm travel range has been deployed.
The motor features 200 nm resolution allowing a fine and precise positioning of the magnet assembly close, but not in contact, with the chip, in order to maximize the macroscopic magnetic field gradient inside the microfluidic chamber.
The motor is oversized for this application, given its flexibility and resolution, however it has been used as already available in the laboratory, thus allowing a faster prototyping.
The magnet assembly, as described in Section 2.3, is composed by two N42 NdFeB permanent magnets by K&J Magnetics, Inc. with parallelepiped shape of dimensions 20x20x5 mm^3. The two largest faces of the magnets with opposite magnetization direction, are brought closer to each other, almost in contact, interposing a μ-metal sheet between them. Due to the opposite magnetization, the two magnets are strongly repelled from each other, thus to bring and keep them together a stainless steel mechanical press has been exploited.
As shown in Figure 4.7, two stainless steel blocks, with a milled socked for magnets positioning, are brought closer tightening two M4 bolts and nuts. The magnet assembly is fixed to the motor stage. The motor is controlled by the PC trough USB communication.

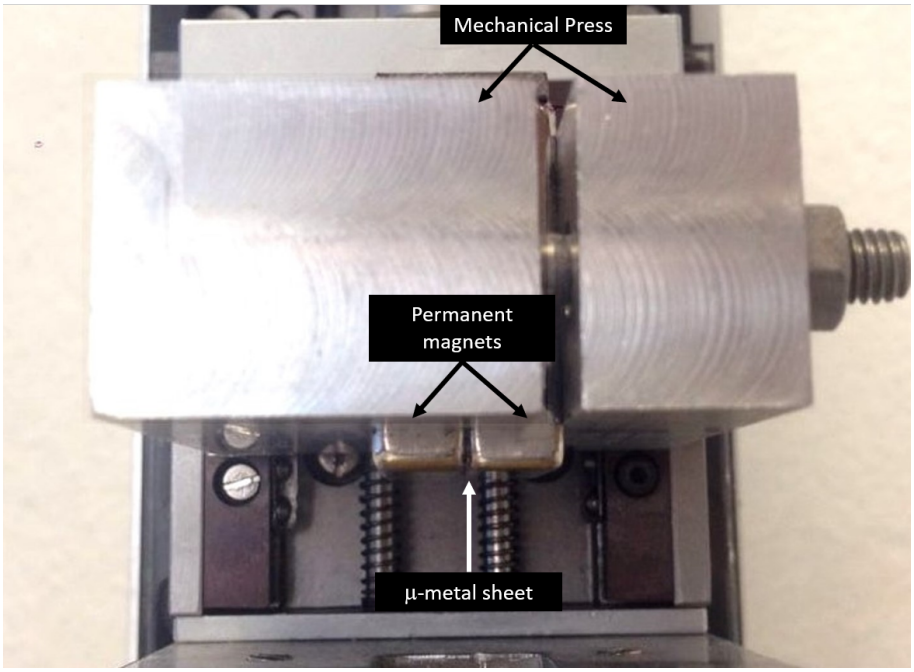

Figure 4.7: *Photo of the permanent magnets assembly.*

Mechanical setup. The mechanical setup, shown in Figure 4.8, hold the electronic board, stepper motor, magnet assembly and the cartridge in a fixed position in respect to each other.
Two rails, milled in a PMMA structure, allow to plug and unplug the cartridge from the electronic board, which is also fixed to said structure, and also set the height position of the cartridge. A second stainless steel structure, connected to the aforementioned one,

keeps the motor, and the magnet assembly linked to it in a vertical position.
The magnet assembly and the cartridge are in a mutual position such that the magnet, when brought close to the chip backplane, fits the aperture on the cartridge lid without touching its borders. Thanks to the rails, the cartridge can be positioned always at the same distance from the magnet, thus the travel range that the motor should make, once calibrated, remain constant.

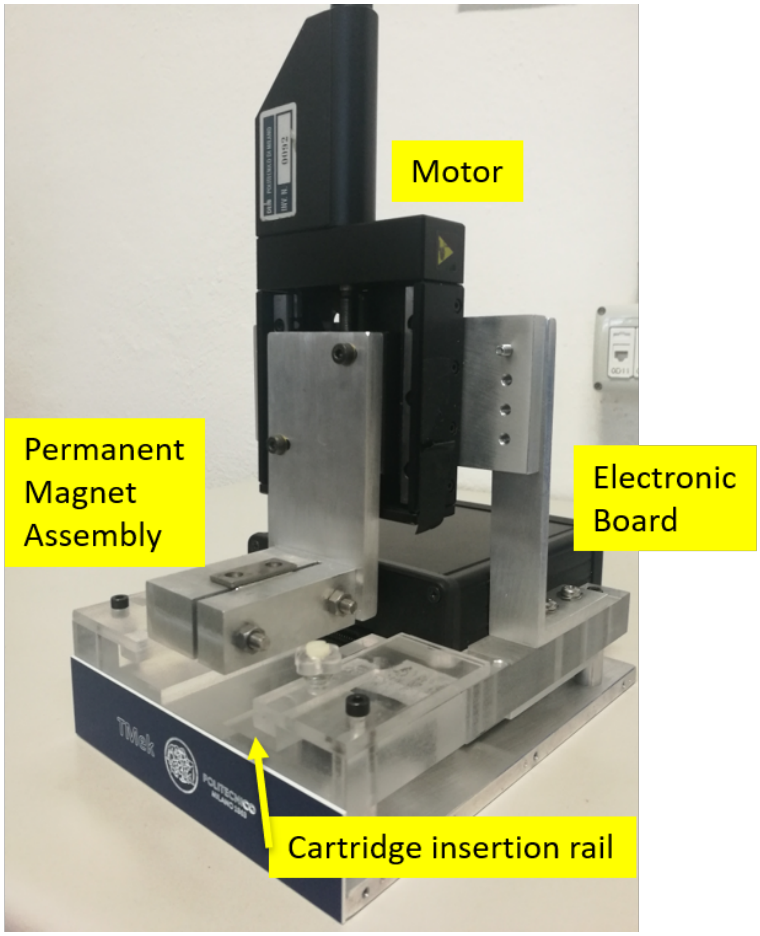

Figure 4.8: *Photo of the mechanical setup with the motor and electronic board placed in position.*

PC. A PC is mainly responsible to communicate with the microcontroller, receive the measurement data from it, control the motor set the test parameters and display its results.
The computer is connected to both the motor and the microcontroller trough USB.
A Graphical User Interface (GUI), implemented using Matlab 2016 App Designer, allows to set the measurement parameters, display the signals coming from the four sensor as well as its state in real-time, to save and elaborate the data.
A detailed description of the software, together with the microcontroller firmware, is given in Section 4.4.

Power Supply. The power supply module for the electronic board, the transformer

and the controller module for the motor are put together inside an aluminium box connected to ground to avoid their noise and disturbances to spread in the environment affecting the chip and the measurement noise performances.
The box uses a C13 power plug to connect it to the mains power supply. A 3-poles DIN cable allows to transfer the ± 12 V from the power supply module to the electronic board.

4.3 Measurement protocol

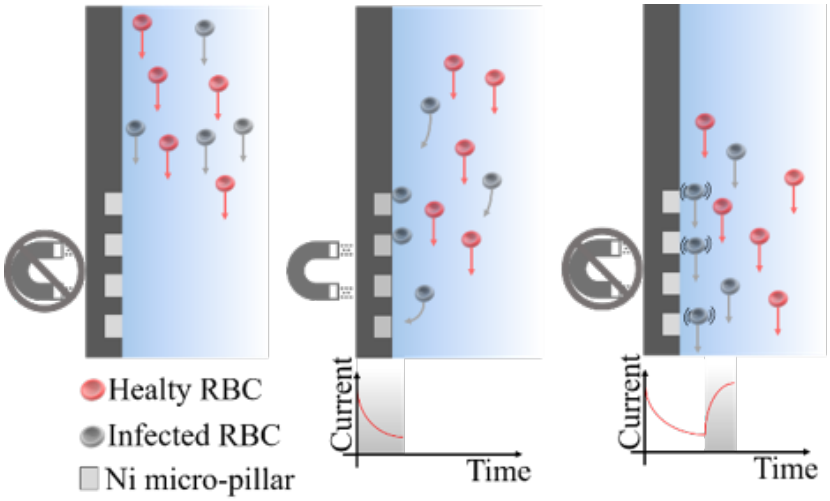

Figure 4.9: *Measurement protocol and working principle of the vertical configuration and signal obtained.*

The measurement protocol mainly defines the movements of the magnet in respect to the chip and the relative timing during the experiments.
In order to better understand the role of each parameter, a schematic representation of the motion dynamics of the particles (i.e. iRBCs and HCs) upon the application of the permanent magnet and the expected electric signal is shown in Figure 4.9. The configuration reported is the so called vertical one, in which the chip is positioned perpendicular to the ground. This is the most used configuration in the experiments as it allows a more efficient capture of the particle in respect to the horizontal one due to the fact that, in the vertical one, the magnetophoretic force does not have to counteract the gravity force. However, the particle dynamic and the expected signal are similar and the differences between the configuration easily deductible from this example.
Looking at Figure 4.9 from left to right, when the magnetic field is not applied, i.e. the permanent magnets are not placed in close proximity to the back of the chip, both the iRBC and hRBC sediment due to gravity force, moving parallel to the chip surface. In this phase there is no change to the registered current.
Upon the application of the magnetic field, only iRBCs are attracted towards the surface of the chip by the magnetophoretic force while hRBCs are not. In particular, the particles of interest are attracted to the pillars where the sensing electrodes are also present. Due to their electrical insulating properties an almost exponential decrease in the cur-

rent flowing between them is registered as more particles approach the electrodes.
The time constant of the exponential signal is in the order of 10^2 s. This signal is superimposed to a slow, almost linear drift of the current due to multiple possible factors like temperature change of the fluid, evaporation and leakages. Due to the variability of the drift and its not negligible amplitude over 10^2 s compared to the signal of interest, it is not possible to accurately quantify the level of parasitaemia. Thus, a faster signal is required in order to reduce the quantification uncertainty caused by the variable relevance of the drift.
Upon the removal of the permanent magnet the magnetophoretic force on iRBCs ceases and the particles are released by the pillars moving parallel to the surface as previously. In this phase an exponential return of the current to the initial value is registered as the particles moves away from the electrodes. The time constant of the exponential in this phase is in the low 10^1 s, one order of magnitude lower than the one of the previous phase.
This is the signal that will be used for the parasitaemia level quantification.
The application and removal of the permanent magnets can be performed several times, obtaining a multiple measurement of the number of particles of interest in the sample until a complete sedimentation of the particles outside the capture region of the chip occurs.
Thus, the main parameters of the measurement protocol, with reference to the graph in Figure 4.10, where an example of signal from tRBCs is given, are:

- *Initial capture time*: the duration of the first application of the magnet corresponding to the time interval of the first capture.

- *Up time*: the time interval in which the magnet is removed and the release of the capture particles takes place.

- *Down time*: the time interval in which the magnet is applied again and the particles are captured anew.

- *Up and down repetitions*: the number of times the applicanion and removal of the magnet are repeated.

It is possible to notice that the *Initial capture time* and *Down time* are differentiated even if they both imply a phase in which the magnet is applied and the capture takes place. Indeed, the initial capture takes place with a longer time constant as the particles are at any distance, allowed by the microfluidic chamber, from the chip surface, while in the subsequent capture phases the particles are already close to the chip surface, thus the signal time constant will be lower.
All the aforementioned parameters can be setted by the user trough the GUI developed.
The signal features of interest for the diagnosis are the amplitude of the exponentials, A, and their time constants. In particular the former feature is proportional to the number of particles captured according to Equation 3.12, thus allowing a quantification of parasitaemia. The latter instead depends on the magnetic property of the particle, i.e $\Delta\chi$, enabling to identify the kind of particle captured.

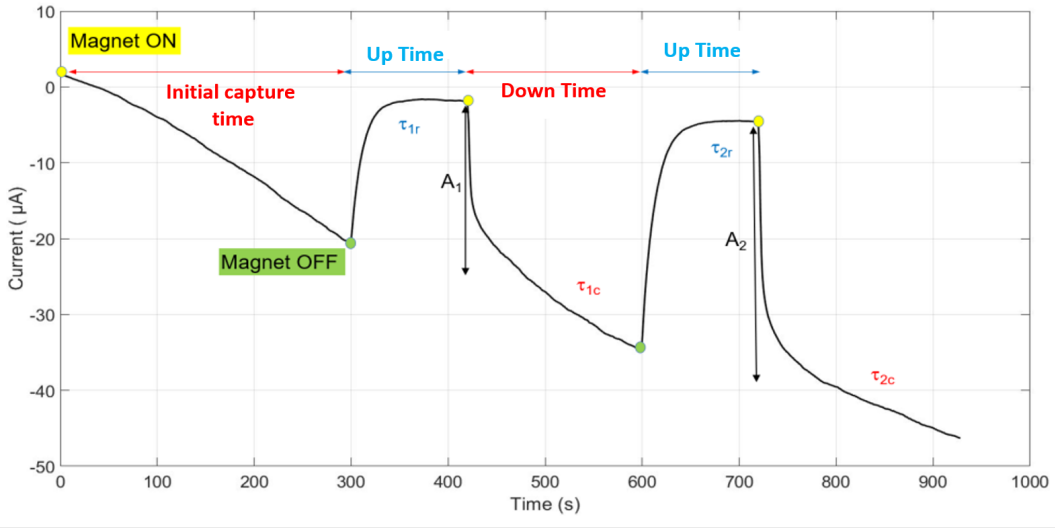

Figure 4.10: *Example of a signal obtained from tRBCs in which the test parameter and the main signal features are highlighted.*

4.4 Firmware and Software

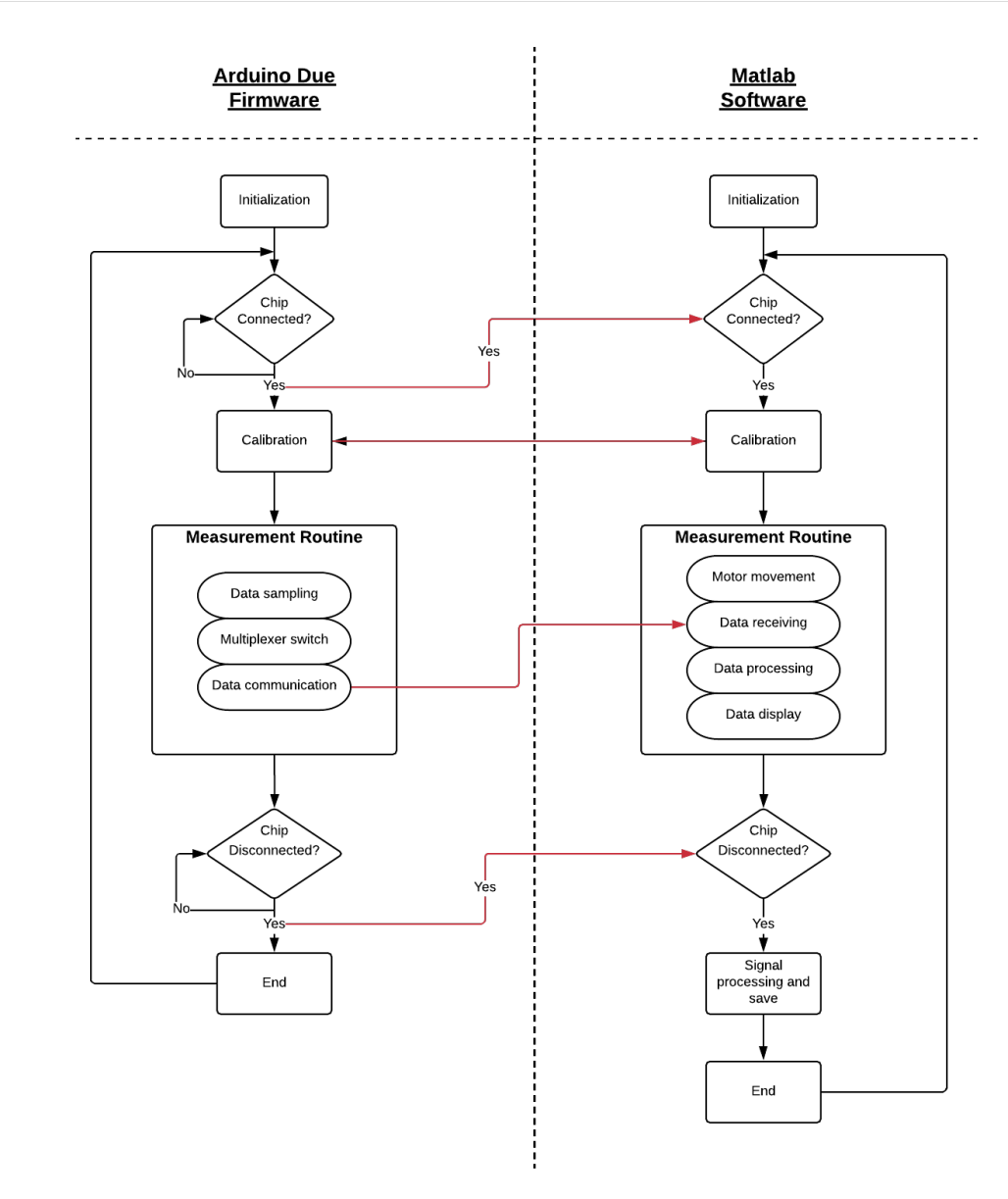

Figure 4.11: *Microcontroller firmware and Matlab custom GUI workflow.*

The firmware for the microcontroller, developed in Arduino IDE, and a GUI for a PC, developed using the App Designer utility in MATLAB 2016, have been designed to automatically perform the experiments, manage, process and display the signal in real time. The two codes communicate and depend on each other. Thus, in this Section they will both be described simultaneously.
In Figure 4.11 the block diagram of the two codes workflow is presented.
In a first initialization phase both programs initialize the variables and Arduino sets the

ICs registers and parameters on the board while the GUI initialize the motor.
A waiting for the insertion of the cartridge follows. During this phase the user can set the parameters of the experiments like: the initial and final position of the motor, the initial capture time, the time in which the motor is kept distant and close to the chip and how many times the up and down of the magnet is repeated.
The interface also allows the user to save said settings with a name in order to select and load a previously saved configuration simply using a drop down menu.
The insertion of the cartridge is automatically detected by the microcontroller as one of its digital input, connected to +3.3 V trough a pull-up resistor, is set to ground by the connection with the cartridge. Once the voltage on its digital input pin changes, it refers the information to the PC through USB and both the programs proceed to the next phase.
During the calibration phase the status of the chip is checked, in particular the resistance value of the measurement and reference areas of all the four sensors on chip.
As the two resistance are not perfectly equal due to fabrication tolerances, this information is useful to adapt the amplitude of the bias stimuli applied to the two areas in order to have an approximately null initial current read by the TIA. To do so a small sinusoid is applied by the DDS, for example, to the measurement area while the reference one is zero. The current flowing in the measurement area is processed by the measurement chain, digitalized and read by the microcontroller which, knowing the applied signal and extracting the current value from the signal coming from the ADC, calculates the resistance value simply using Ohm's law.
This operation is repeated for the reference area and for all the four sensors.
The resistance value is then used to set the voltages on the areas in order to satisfy the relation $V_{measure}/V_{reference} = R_{measure}/R_{reference}$ keeping the maximum voltage to 100 mV and decreasing the other. The obtained voltage amplitudes are applied to the sensors and further finely tuned iteratively, if needed, until the current registered fall beneath a certain threshold.
The voltages amplitudes and resistance values are then sent to the PC, which immediately display them, in order for the user to assess the correct behaviour of the sensor.
The PC then sends the test parameters, set by the user, to the microcontroller. Subsequently the test starts.
The microcontroller samples the data from the ADC at a frequency of 10 kHz and commute sensor every 250 ms, thus returning to each sensor every 1 s. After each commuting, Arduino Due discard the first 50 ms of data in order to get rid of an eventual transient peak arising from the switching.
Once it gathered the samples from all the four sensors, thus each second, it communicates them to the PC trough USB communication.
The software on the PC collects all the data, average them in order to obtain one single sample from each sensor. It converts the binary voltage data into the corresponding current at the input of the TIA and display them updating the plots with the previous samples.
The software is also responsible to move the magnet at specific instants of time defined by the user through the test parameters.
The measurement routine is repeated several times until the total test time is reached.
Subsequently both the microcontroller and the PC wait for the disconnection of the car-

tridge, sensed by the former in the same way as it happened for the connection. Once the cartridge has been disconnected the information is sent to the PC.
The firmware code restarts from the cartridge connection wait, ready for the next experiment to start. On the other hand the GUI allows the user to insert information about the tests like patient/test ID, cartridge and chip used, vertical or horizontal configuration. Then the software processes the raw signal extracting the time constants and amplitudes from it and then saves both the raw data and the processing output as well as plots of the raw and processed signal in a database.
A detailed explanation of the signal processing performed and its outcomes are described in the next Subsection 4.4.1.
The software then waits for the signal of cartridge insertion coming from the microcontroller to start the cycle anew.

4.4.1 Signal processing

At the end of an experiment, the software process the signal in order to extract quantities and features of interests.
As shown previously directly on the graph in Figure 4.10, the relevant features in the signal are: the amplitude of the exponentials and the time constant of both the capture phases (τ_c) and release ones (τ_r). The amplitude is directly proportional to the number of particles captured. The capture time constant gives information about the magnetic properties of the attracted particle, namely a particle with higher $\Delta\chi$ give rise to a lower τ_c than iRBCs. The release time constant depends mainly by the particle volume, density and its ability to adhere to the surface of electrodes.
To clean the first exponential of the signal from the drift, a straight line passing trough

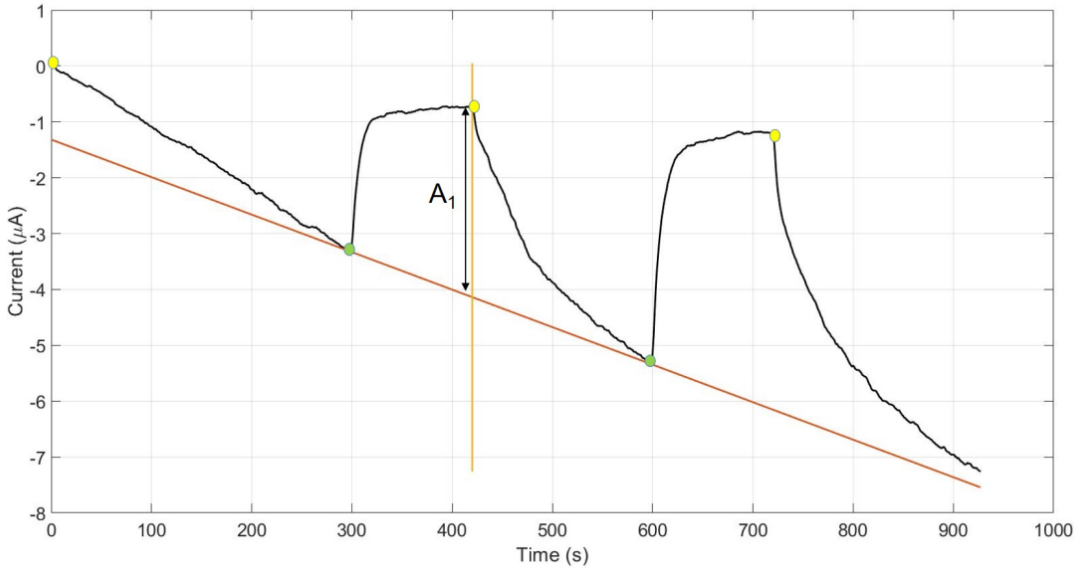

Figure 4.12: *Sample signal of tRBC showing the straight line used to subtract the drift and extract the exponentials from the data.*

the lowest points of the *Up time* and *down time* of the signal, as shown in Figure 4.12, is subtracted to the curve. The straight line represents the drift.

After subtraction the exponentials of the *Up time* and *Down time* are processed separately but in the same way. They are both fitted with an exponential law $y = A \cdot e^{Bx/\tau}$ where A and τ are respectively the amplitude and time constant of the exponential. The 95% confidence bounds of the exponential fitting and the variance of the signal noise fluctuations are considered to compute the amplitude and time constant error.
The process is repeated for every *Up and Down time*, i.e. for every magnet application-removal cycle.
Once the signal processing is complete all the parameters of the experiment, the extracted features and errors are automatically saved in an Excell database, while the raw data, raw and processed plots are also automatically stored in a specific folder named with a code representing the patient ID, the chip and configuration used.

4.5 Red blod cells treatment protocol

Red blood cells can be chemically treated to change their magnetic susceptibility becoming very similar to the one measured on malaria infected red blood cells. In particular, the treatment aims to transform the haemoglobin contained in the RBC from oxyhaemoglobin (oxy-Hb), which is diamagnetic, to methaemoglobin (met-Hb), which is paramagnetic.
Methaemoglobin is a form of haemoglobin in which the bond to oxygen is prevented, thus, differently from deoxyhaemoglobin, which is the de-oxygenated form of haemoglobin, it can not turn into oxyhemoglobin. The magnetic susceptibility change is due to the transformation of the iron atoms in the haemoglobin molecule from Fe^{2+} to Fe^{3+} like it happens during the formation of hemozoin (see Section 1.1.2). Due to the paramagnetic property of methaemoglobin, the RBCs containing it acquires similar properties as shown in Section 2.2.
In order to cause this transformation, RBCs must be exposed to oxidising drugs, like $NaNO_2$.
In this thesis the below protocol has been used.
Firstly, the whole blood sample treated with 100 units of heparin is centrifuged in order to separate RBCs from both the plasma and buffy coat. The isolated red blood cells are resuspended in 1x Dulbecco's PBS (Sigma-Aldrich). The resulting suspension is then oxygenated for 30 min using a peristaltic pump at 8 ml/min at room temperature. The oxygenated RBCs suspension is then centrifugate and resuspended in PBS.
This step is performed in order to remove RBCs that have been haemolized during the oxygenation process.
$NaNO_2$ is added to the RBC suspension in order to obtain a concentration of 840μg/ml. The so obtained suspension is then rocker-incubated for 30 min at room temperature and then centrifugated and resuspended in PBS at a 40% Haematocrit.
This is the starting solution from which further dilution are taken to perform the experiments reported in Section 2.5 and Chapter5.
In the experiments, when noted, a certain amount of plasma is added to the solution in order to mimic a whole blood dilution. For example in a 1:10 dilution of the starting solution 1:10 of the volume is substituted with plasma.
As can be seen from Figure 4.13, the treatment, thus the modification of haemoglobin, cause a colour change in RBC, similar to what happens naturally for venous and arterial

blood. In particular, in Subfigure (A) and (B), images of, respectively, the normal and treated blood sample are shown.
This difference in colour caused by the presence of oxyhemoglobin or methemoglobin

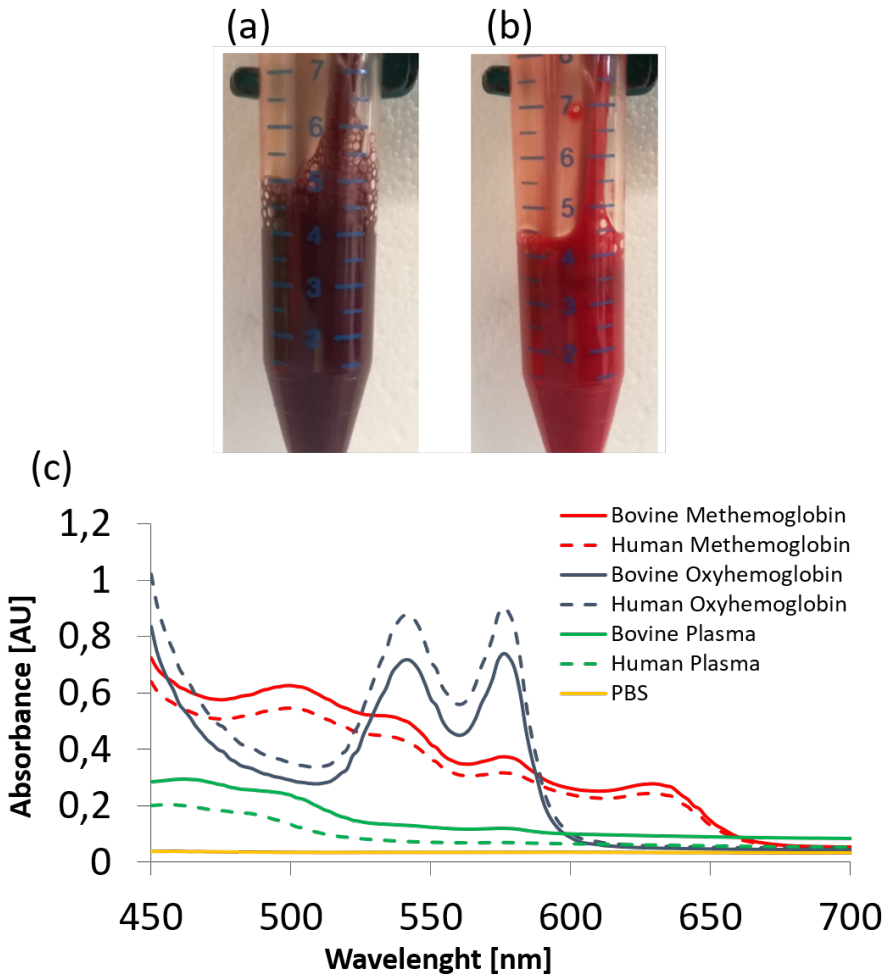

Figure 4.13: *Photographs showing the colour difference between (A) a normal venous blood sample and (B) $NaNO_2$ treated one. (C) Absorbance spectra of several blood samples.*

can be exploited to verify the success of the treatment and quantify the average methemoglobin content of RBCs. This has been quantitatively assessed evaluating the absorbance spectra of the treated and untreated samples trough spectrophotometry carried out using Infinite 200Pro spectrophotometer by Tecan Trading AG.
The relative concentration of metHb (C_{met-Hb}) and oxy-Hb (C_{oxy-Hb}) can be estimated trough Equation 4.2 and 4.3 respectively. [105, 106]

$$C_{met-Hb} = \frac{A_{met-Hb}}{A_{met-Hb} + A_{oxy-Hb}} \tag{4.2}$$

$$C_{oxy-Hb} = \frac{A_{oxy-Hb}}{A_{met-Hb} + A_{oxy-Hb}} \tag{4.3}$$

where $A_{met-Hb} = 279\epsilon^{630} - 3\epsilon^{577}$ and $A_{oxy-Hb} = 66\epsilon^{577} - 80\epsilon^{630}$ are the absorbance fraction of met-hb and oxy-Hb respectively, while ϵ^x is the absorbance measured at the

x nm wavelength.
Using the aforementioned equations, a percentage around 85-97% of oxy-Hb converted into meth-Hb has been estimated. In Figure 4.13(C) the absorbance spectra of oxy-Hb and met-Hb for both human and bovine RBC, measured on the samples treated as previously described, are shown.

CHAPTER 5

Results

In this chapter the results obtained using the complete Tid Mekii system are presented. Experimental results, on specific topics have been already shown in the previous chapters and here briefly summarized..
In particular, a study concerning both the electrical and magnetic properties of hemozoin crystals have been discussed in Section 2.4. In this study the magnetic susceptibility of HCs has been measured trough a Vibrating Sample Magnetometer, obtaining a resulting $\chi = 410 \cdot 10^{-6}$, thus showing a paramagnetic behaviour of these particles. The correctness of the aforementioned measurement has been indirectly assessed comparing the magnetophoretic attraction speed of superparamagnetic beads ($\chi = 1$) with HCs. The capture times obtained clearly showed a longer capture time for hemozoin than for the beads, highlighting that the former susceptibility is lower than 1, hence disproving the superparamagnetic nature of HCs.
Also their electrical properties of HCs have been investigated in order to determine whether their are to be considered insulating or conductive particles. The conductivity has been measured, in DC, trough Current Sensing AFM, while in AC by means of electrical impedance spectroscopy. In both cases an insulating behaviour has been noticed.
Moreover, a study on the capture efficiency of different magnetic concentrators geometries has been shown in Section 2.5. The aim of the study was to provide, in addition to numerical simulations, guidelines for a proper design of the magnetic layout. Different pillars geometries, as well as gasket thicknesses have been compared using tRBCs as particles. The selectivity of the technique has been also verified, i.e. the ability to attract only tRBCs and not hRBCs magnetophoretically.
Finally, the measurements assessing the performances of the designed and fabricated electronic board have been reported in Section 3.4.

Following in this chapters the different results are divided depending on the particles studied and a separated section is reserved to the experiment campaign carried out at Hopital Saint Luc, a local hospital of Mbalmayo, Cameroon, Africa, where malaria is endemic.
In particular the results involving HCs are reported in Section 5.1, the ones concerning both cultured and malaria infected RBC are reported in Section 5.2 while the outcome of the test campaign carried out in Africa in Section 5.3.

5.1 Results on hemozoin crystals

The experiments involving hemozoin have been carried out using synthetic crystals supplied by Invivogen.
The synthetic version has been proven to be very similar to its natural counterpart both in the chemical structure, crystal dimension and magnetic properties. [89, 90]
Hemozoin is the particle, considered in this work of thesis, which is attracted the most by magnetic field as its magnetic susceptibility is at least two order of magnitude higher than the one of iRBC at any stage of the disease.
However, from a detection point of view, being the volume of a single crystal three order of magnitude lower than the one of a red blood cell, it generates a signal of the same orders of magnitude lower. However, it should be pointed out that from a diagnostic point of view, more than the number of HCs or RBCs that can be detected, the important parameter is the level of parasitaemia, id est the number of malaria parasites per μl of blood. As every parasite infects one RBC and creates almost 20 HCs, the detection capability to detect one of the former particles should be compared with twenty of the latter. Even considering that HCs quantity is twenty times higher, RBCs are still two order of magnitude easier to detect thanks to their volume 1000 times larger than the HCs.
In other words the minimum detectable parasitaemia would be one hundreds times lower if the detection is based on HCs detection, which can be performed for example causing the cell lysis of all the RBCs in the sample, thus releasing HCs from their hosts.
Although the RBC detection was selected as the main target of the sensor, in normal conditions, i.e. when the blood of the patient is not haemolyzed, a certain amount of hemozoin crystals can be found free in blood, contributing to the overall signal. Thus, the capture and detection capability of the system concerning HCs have been investigated.
In Figure 5.1 the signal obtained from hemozoin using the chip in (A) horizontal configuration and (B) vertical configuration is reported; the inset in (A) shows a microscope image of the hemozoin crystal captured and concentrated by the pillar on the electrodes.
The concentration of hemozoin used in this experiment is 300 ng/μl (10^4 HCs/μl or 500parasites/μl).
It is possible to notice that in both cases a signal is obtained, meaning that the system is able to capture HCs in both configurations. In particular the amplitudes of the two signals are approximately equal, giving rise to an amplitude of about 0.4 μA. However, it can be also noticed that the horizontal is characterised by slower rising and falling exponentials with a $\tau \approx 8 - 15$ s while the vertical by steeper ones with a $\tau \approx 3 - 6$ s. This difference is in agreement to what expected looking at balance of forces.

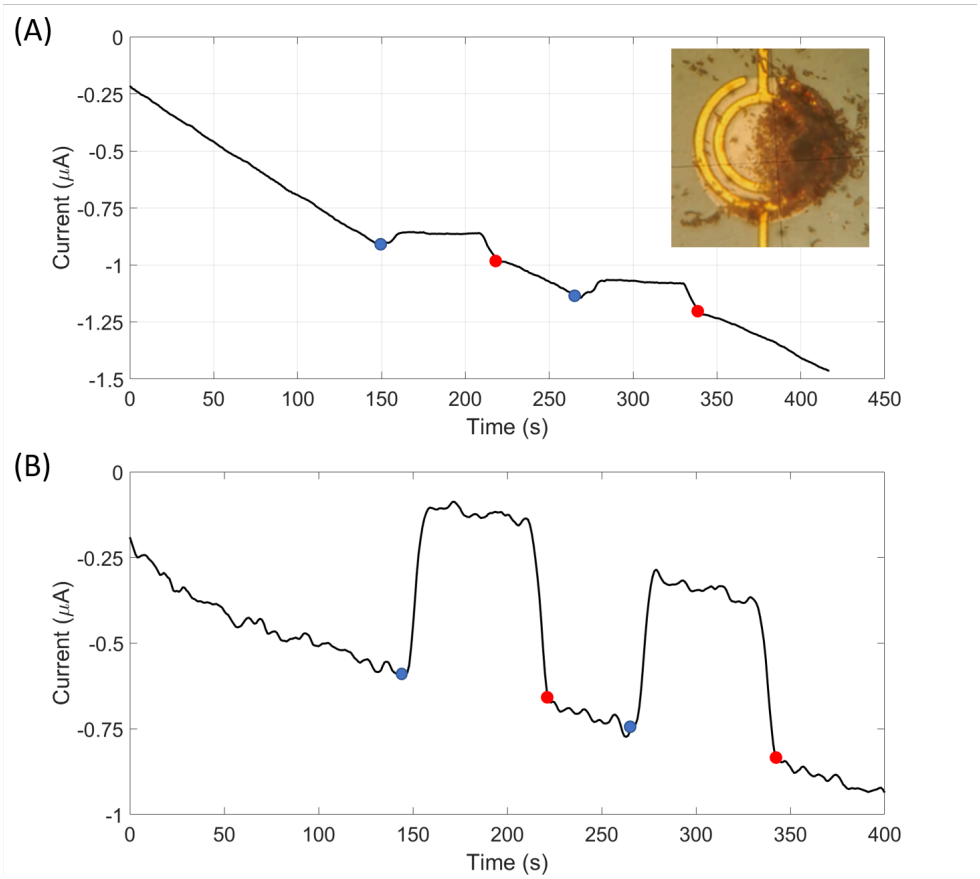

Figure 5.1: *Impedimetric signal obtained from HCs using (A) horizontal configuration and (B) vertical one.*

As a matter of facts in the horizontal configuration the magnetophoretic force should counteract completely the gravity force, while in the vertical one the two forces act on two perpendicular directions.
It is also important to notice the presence of a slow and almost linear drift in the current measurement. The origins of the drift are not completely understood yet. It could be caused by a leaky sealing of the microfluidic chamber which causes the evaporation of the liquid, causing a variation in the salts concentration solved in the fluid, thus causing a conductivity variation of the latter. Another hypothesis is that the drift is caused by the mechanical relaxation of the spring contacts which shift on the electrodes pads, consequently varying the contact resistance between them.
The drift slope and direction change at each experiment, thus a processing of the signal to remove it is necessary, as explained in Section 4.4.1.
As it can be deduced from Equation 3.12, the difference between the current flowing in the measurement area and the reference one (Δi) is linearly proportional to the particles volume, then on their quantity. Thus, in order to verify the linearity and steepness of the sensor response, experiment at different HCs concentrations have been carried out and the resulting signal amplitudes are reported in Figure 5.2.
The red dots in figure represent the experimental data while the black line is the expected theoretical trend obtained from Equation 3.12. A linear response and a good

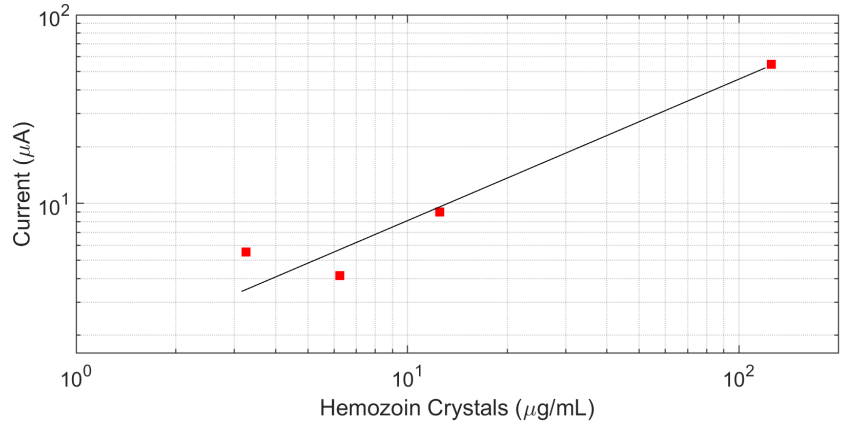

Figure 5.2: *Calibration curve of HCs current signal as a function of its concentration.*

agreement between the experiments and theoretical expectations can be observed. At low HCs levels, below 10^1 μg/ml, the experimental data drift from the straight line as the noise and disturbances in the measurement prevent an accurate quantification of the signal amplitude.
The graph proves the possibility of quantifying the HCs concentration (down to 10^4 HCs/μl or 500parasites/μl), thus the parasitaemia level, based on the signal amplitude.

5.2 Results on red blood cells

Red blood cells are the main particles of interest on which Tid Mekii diagnosis is based. However, due to their large volume and low magnetic susceptibility in respect to hemozoin, they represents the major challenge for the magnetophoretic attraction.
Indeed, as it is possible to notice in Figure 5.3, an highly different signal amplitude is obtained between experiments performed in horizontal (A) and vertical (B) configurations for RBCs.
The inset in (B) shows a microscopy image of the tRBCs captured by the pillars close to the electrodes.
In these experiments bovine tRBCs have been used with a concentration of 1000 tRBCs/μl corresponding to a parasitaemia of 1000 parasites/μl.
The amplitude of the signal in horizontal configuration is approximately 200 nA for both Up and Down cycles, while in vertical configuration the amplitudes of the two Up and Down cycles are different, 1μA the first one and 1.5μA the second. Observing the signal amplitudes it is possible to deduce that the system is able to capture only tRBCs that are close to the chip surface in horizontal configuration, while it is capable to reach higher depths in vertical configuration thus collecting more tRBCs and consequently more signal.
The difference between the amplitude of the first Up and Down cycle and the second one highlights the slowness of the capture process for tRBCs. Indeed, during the second application of the magnets assembly to the chip, an higher amount of tRBCs are attracted and sensed than the one registered after the initial capture phase.
The time constants of the exponentials differs from those of hemozoin, remarking the magnetic susceptibility difference between the two particles. In particular the exponen-

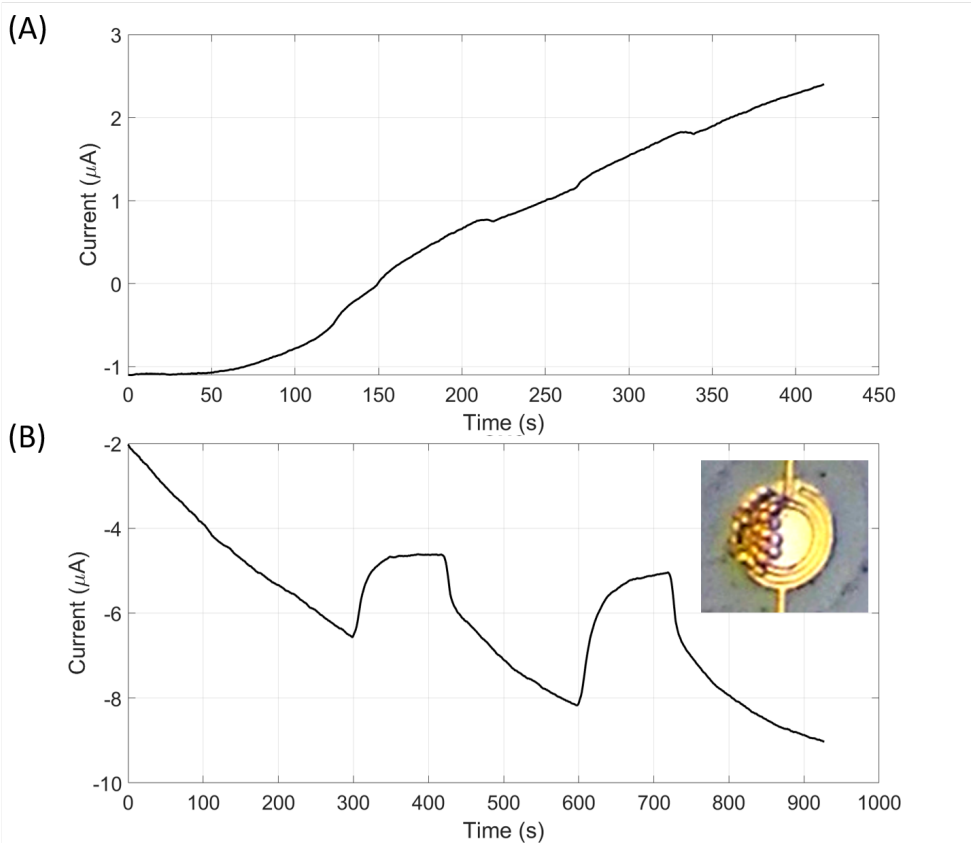

Figure 5.3: *Impedimetric signal obtained from tRBCs using (A) horizontal configuration and (B) vertical one.*

tials linked to the release of tRBCs (i.e. the rising exponential) have a time constant $\tau \approx 18 - 25$ s while the ones caused by their capture have a $\tau \approx 29 - 35$ s.
The difference between the HCs and tRBCs time constants can be useful to distinguish the two kind of particles in the signal, being then able to separately quantify them.
Another exploitable gimmick for this purpose is to perform the measurements both in horizontal and vertical configuration as in the former almost solely HCs are attracted thus their contribution can be separated from the total one obtained in the vertical configuration.
Noteworthy is, again, the entity of the drift, which amplitude and sign can change between experiments.
Several experiments have been performed at Sacco Hospital on treated tRBCs from human blood sample withdrew from volunteers, in order to obtain a calibration curve and assess the parasitaemia limit of detection of the system.
Whole blood samples have been diluted in PBS 1:10 in order to obtain an haematocrit of 4%.
In Figure 5.4(A) the results of this study are shown.
The black markers report the experimental data, the red ones the theoretical values obtained from Equation 3.12 while the black line the linear regression of the experimental data below $4{\cdot}10^4$ tRBCs/μl.
Three experiments for every tRBCs concentration have been carried out and the error

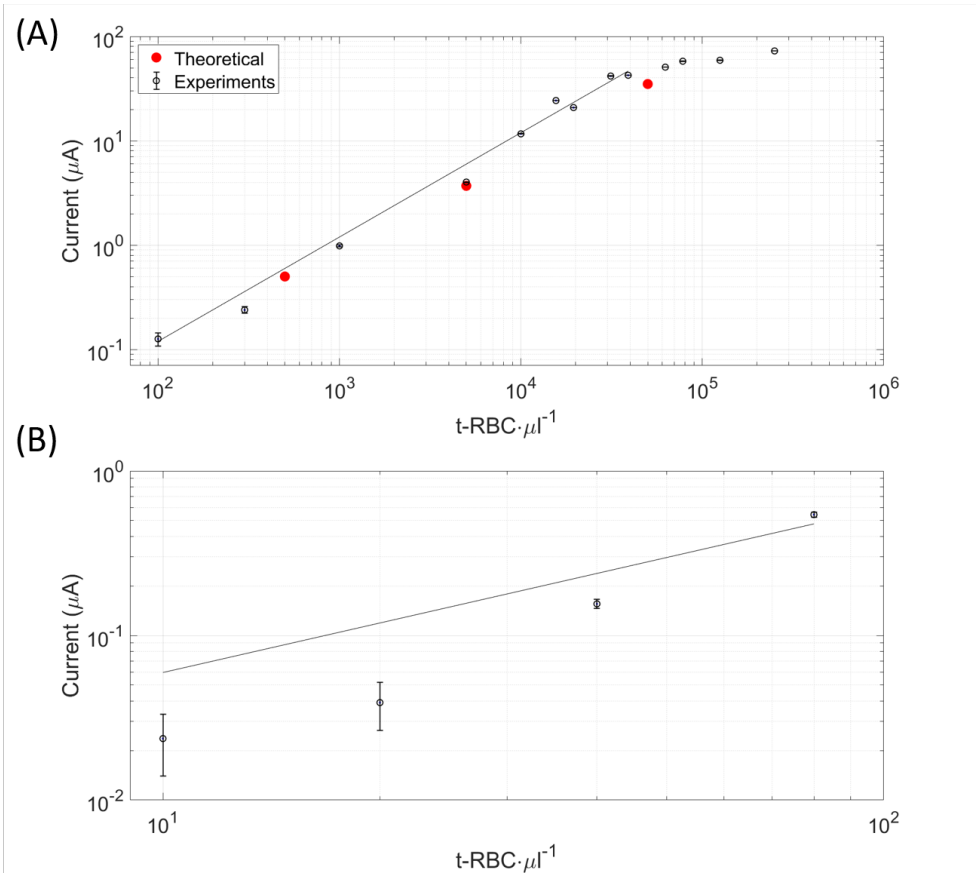

Figure 5.4: *Calibration curve of human tRBCs current signal as a function of its concentration. (A) Current signal calibration curve for tRBCs concentrations until 10^2 tRBCs/μl obtained using an initial capture time of 300s. (B) Current signal calibration curve for tRBCs concentrations between 10^1 and 10^2 tRBCs/μl obtained using an initial capture time of 600s.*

bars on the experimental markers represent the span between them.
The experimental data are in good agreement with the theoretical expectation, deviating from it by a 20% maximum, and showing a linear trend. A deviation from said trend is observed at tRBCs concentrations above $4{\cdot}10^4$ tRBCs/μl which is caused by the saturation of the PGA output.
In (B) the calibration curve for tRBCs concentrations below 10^2 tRBCs/μl, in which data have been obtained exploiting an initial capture time of 600 s instead of 300 s as previously done, is reported.
The increased capture time allows to attract more tRBCs, then gathering more signal at the same parasitaemia.
The capture time previously chosen will be kept for all the next experiments as it provides a good compromise between signal amplitude and diagnosis time, which is an important project specification.
A limit of detection of 10 tRBCs have been obtained which is the same of the microscopy examination, the gold standard for malaria diagnosis.
As the amount of iRBCs in the blood stream increases with the advancing of the disease and their number rapidly decreases as the plasmodium is vanquished by the immune

system or by antimalarials, a follow up of the disease can be performed testing blood samples withdrew from a malaria infected patient at different time moments after the administration of antimalarials. A decrease of the signal is thus expected as the disease regresses.
In order to assess this important feature, three blood samples, withdrew 24h apart from each other from the same patient affected by malaria (P. vivax), have been analysed. The bood samples have been provided by Sacco Hospital after approval by ethics committee.
In Figure 5.5 the top graph reports the signal obtained from the sample gathered when the patient has been hospitalized and the first diagnosis has been made, detecting a P. vivax infection with $8{\cdot}10^4$ iRBCs/μl parasitaemia.
Immediately after, antimalarials drugs have been administered to the patient.

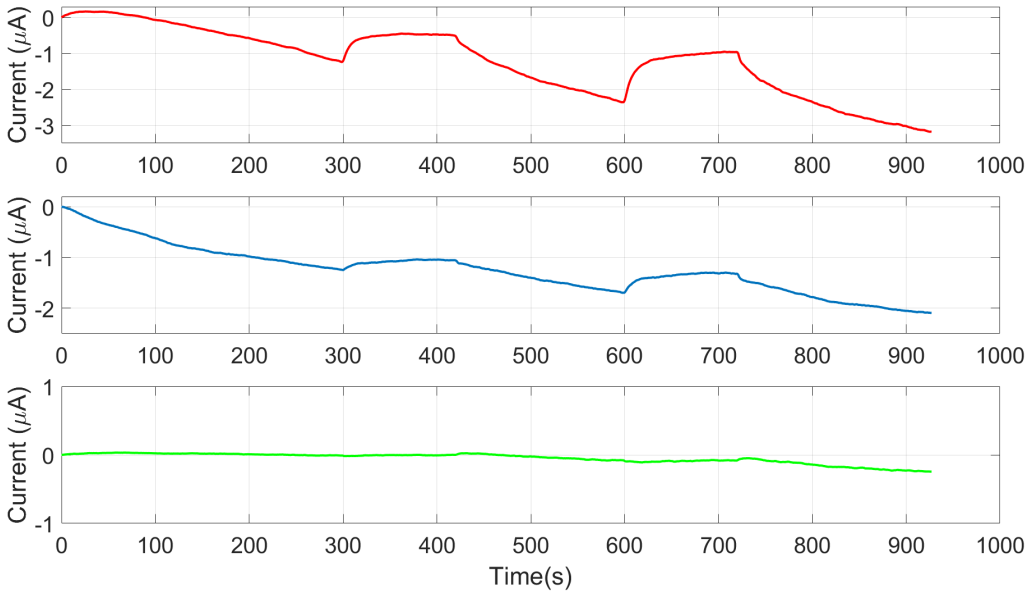

Figure 5.5: *Follow Up of the treatment of a P. Vivax infected patient. From top to bottom, signal obtained brom the samples withdrew respectively 0, 24 and 48 hours after the treatment.*

The central and bottom graphs show the signals coming from samples withdrew, respectively, 24 and 48h after the treatment.
As can be seen the amplitude of the signal decreases over time until it almost vanishes in the third sample, when also the hospital diagnosis, performed using PCR, assessed the successful healing from the disease. In particular the amplitude goes from 1.2μA for the top graph to 0.4μA and 0μA for, respectively, the central and bottom graph.
Hence, this study proves the potential use of Tid Mekii for the treatment follow up. Such feature represent a relevant advantage in respect to RDTs, which can not perform such analysis due to the persistence of antibodies, on which they base the diagnosis, in the blood stream for several weeks after the complete healing from the disease.
Another capability of the instrument that have been explored is to distinguish the different stages of Plasmodium on the signal shape and morphology.
This activity has been carried out at Istituto Superiore di Sanitá (ISS) in Rome on

malaria infected red blood cells at different stages of the disease cultured by Prof. Pietro Alano's group.
In Figure 5.6 are shown, from top to bottom, the signal obtained from ring, trophozoite and gametocytes stage RBCs, all in a concentration of 5000 RBCs/μl and suspended in PBS 1:10.
It is clearly noticeable the different morphology of the signal.

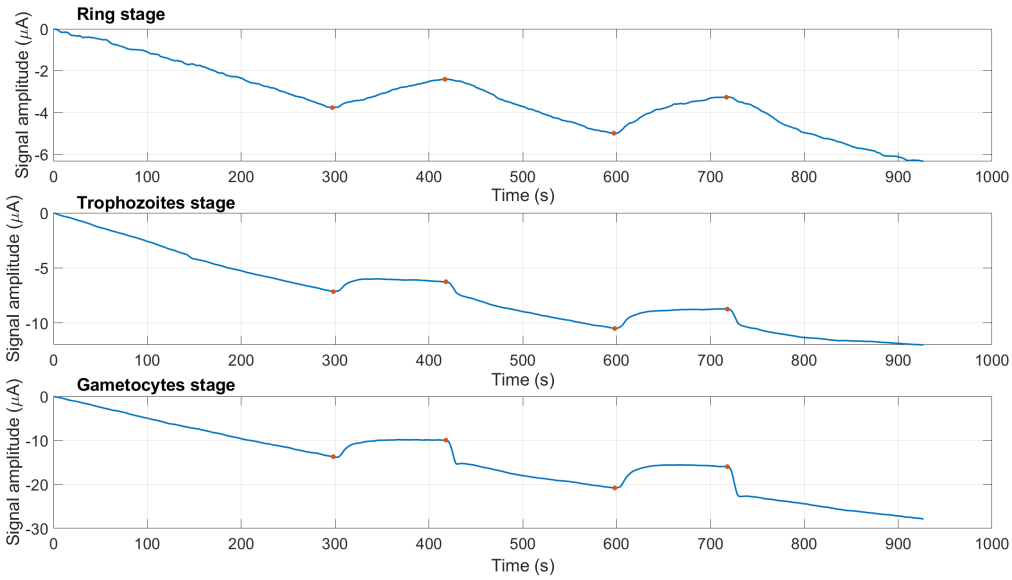

Figure 5.6: *Signal morphology comparison of different iRBCs stages. Top graph: ring stage. Central graph: Trophozoite stage. Bottom: Gametocytes stage.*

The ring stage represent an early infection of the RBC by the Plasmodium, thus the amount of HCs produced is low and consequently the magnetic attraction of the cell weak. This is verifiable by the higher time constant of the capture and release phase which, despite the signal does not come to a steady state, is higher than 50 s.
Trophozoite RBCs instead corresponds to a more advanced stage of the Plasmodium, thus their HCs contents is higher than the previous. The signal shows a morphology similar to the one obtained with iRBCs with time constants slightly lower for both the release ($\tau \approx 14 - 19$ s) and capture ($\tau \approx 26 - 31$ s) phase.
The last particles taken into account in this study, the gametocytes, show the fastest capture signal. Moreover, peculiar is the small peak during the release phase which cause has not been identified yet. The exponential in the capture phase has a time constant $\tau = 5 - 9$ s.
These preliminary experiments prove the possibility of the device to distinguish the different particles.
Further studies and signal processing methodologies should be carried out and developed for being able to separate and quantify the different contribution when the signal is caused by a mixture of different particles, i.e. rings, trophozoites, gametocytes RBCs and HCs.

5.3 Preliminary clinical validation

In April 2019 we carried out a 15 days test campaign, with the approval of ethic committee, at Hopital Saint Luc, an African hospital in a small city named Mbalmayo, Cameroon, where malaria is endemic.
The aim of this study was to validate the system on a statistically relevant sample of patients in order to assess the key performance indices (KPI) of the test (i.e. Sensitivity, Specificity, Positive predictive value and Negative predictive value) comparing Tid Mekii diagnosis with the more established diagnostic techniques (microscopy and RDT) as well as receiving feedbacks about the perceived easy of use and possible improvements from the clinicians, who directly performed the tests using Tid Mekii.
After a first day of disclosure and training of the medical staff about Tid Mekii principle and features, sample preparation and loading, handling of the cartridge and its insertion in the reader (i.e. the experimental setup comprising mechanical structure, electronic board, motor and magnet assembly), the testing phase has begun.
During the campaign, 108 blood samples, from patients suspected of being affected by malaria after a first medical consultation and who signed voluntarily an informed consent, have been analysed.
For each subject adhering to the initiative, a document containing personal informations (i.e. age, sex, pregnancy, fever, symptoms, medical history), diagnosis performed by the clinician, and blood count (i.e. number of platelets, white blood cells, red blood cells, haematocrit etc..) has been filled. Each blood sample has been taken and processed anonymously as well as all the relative documentation and data of the patient.
Also samples taken at Hopital Central and Hopital Cass of Yaoundé, capital of Cameroon, and delivered to Hopital Saint Luc have been analysed and processed like the one coming from the former hospital itself.
Each blood sample in this study has been analysed locally, for diagnosis reference purposes, with two of the main diagnostic techniques for malaria: thick blood smear microscopy examination and RDT, (SD Bioline Malaria Ag P.F/PAN by Abbot). Moreover, the thick blood smear glass slides have been collected and taken to Italy for a second analysis performed by three microbiologists at Sacco Hospital.
Venous blood samples of about 2-3 ml have been withdrawn from the patients and collected, as common use, in test tubes with EDTA anticoagulant on the bottom.
A fraction of the same sample has been used for the diagnosis with the reference techniques while just 8 μl has been used for Tid Mekii. The 8 μl whole blood samples have been diluted, by the clinicians, in 72μl of PBS with 1000 units of heparin in order to obtain a blood dilution of 10.
The Tid Mekii chip have been inserted in the cartridge, as well as the glass slide with the gasket on top; a 70μl of the resulting solution has been poured on the glass slide, by means of a micropipette, and the cartridge closed and plugged into the reader.
All the above mentioned operations have been carried out by the clinicians under our supervision.
All the tests have been carried out using the following measurement parameters:

- *Initial capture time*: 300 s,
- *Up time*: 120 s,

- *Down time*: 180 s,
- *Up and down repetitions*: 2 for the experiments of the first 9 days, 1 for the last four days (change made in order to perform more test each day).

Among the 108 samples analysed with Tid Mekii, 33 have been discarded due to an inappropriate storage of the sample (as some sample delivered from external hospitals have been frozen), or if the time interval between the withdrew and the test has been longer than 16 hours or if the signal shows anomalies that lead to a possible fault in the measurement.
The two former cases, as experienced during experiments performed in the lab, cause hemolysis of the RBCs which alter the $\Delta\chi$ of the sample leading to false positives. In the latter case, instead, signals have been discarded if one ore more of the followings features is observed: change in the drift slope 50 s before the application of the magnet or its removal, signals with opposite direction in respect to the expected ones, large signal fluctuations higher than 2 μA that are not correlated with the signal of interest.
To make uniform the diagnosis, only the first up and down cycle has been considered, as the second one has not been performed for a small portion of samples in order to reduce the diagnosis time.
The sample has been considered positive if its amplitude respect the following condition:

$$A_{signal} - A_{motor} > err \tag{5.1}$$

where A_{signal} is the amplitude of the release exponential, the amplitude of the signal caused by the magnet movement and err is the peak-to peak amplitude of the noise and A_{motor} fluctuations.
In particular A_{motor} is a square-shaped signal, which amplitude is in the order of 20-100 nA, that arises by the application and removal of the magnet assembly to the back of the chip. It is superimposed to the signal of interest generating a certain degree of uncertainty in establishing the signal amplitude, especially at low parasitaemia levels. This signal amplitude is greater the closer is the magnet to the chip, and it has been hypothesized to be caused by the force exerted by the magnets onto the pillars on the chip that causes a displacement of the chip in respect to the spring contacts.
In order to measure A_{motor} and the relative fluctuations, several measurements have been performed in Cameroon, every day, using only PBS as sample, in order to isolate the signal contribution caused by the magnets.
A further condition has been applied to the time constants which should be between 6 s and 25 s.
Following this protocol for an automatic analysis and taking as a reference the diagnosis performed by three microbiologist of Sacco Hospital based on the thick blood smear, collected in Cameroon and brought to Italy, and on the blood count reports, the Key performance indices have been extracted.
The obtained results are reported in Table 5.1 and are compared to the RDTs results performed in Cameroon, using, also in this case, the diagnosis performed at Sacco Hospital as a reference.

During the test campaign no false negatives (FN) have been registered, leading to a 100% sensitivity with a 95% confidence interval between 90.3% and 100%. This means that, if further confirmed by more extensive validation on a larger set of patients, no pa-

Table 5.1: *Key performance indices comparison between Tid Mekii and RDTs. The numbers in parentheses for the last four indices represent the 95% confidence intervals boundaries.*

Index	Tid Mekii	RDT
True positive	46	45
False positive	10	5
False negative	0	1
True negative	19	24
Sensitivity (%)	100 (90.3; 100)	97.8 (87; 99.8)
Specificity (%)	65.5(45.5; 81.4)	82.7 (63.5; 93.4)
Negative predictive value (%)	100 (79; 100)	96 (77.6- 99.7)
Positive Predictive value (%)	82.1 (69.1; 90)	90 (77.4; 96.2)

tients are diagnosed negatives to malaria while having it, thus not receiving a proper treatment.
However, 10 samples resulted to be false positives (FP) leading to a specificity of 65% (with 95% confidence interval between 45.5% and 81.4%). Despite it is less severe than a FN diagnosis as it leads to the treatment of patients not having malaria, an extensive use of antimalarial drugs causes, in the long run, a resistance of the Plasmodium to them and also brings unnecessary risks to patients health due to drugs side effects. The FP occurrence can be possibly linked to an haemolysis of the sample or to patients affected by thalassaemia, i.e. with an high amount of iron in haemoglobin, which can possibly cause a change of the magnetic susceptibility of the RBCs. However, a further and dedicated study should be carried out to confirm this hypothesis.
In Figure 5.7 the amplitude of the signal as a function of the parasitaemia level, which has been estimated by the microbiologists of Sacco Hospital following the thick blood smears analysis, is shown.
Only true positive samples taken directly by Hopital Saint Luc, on which hence we are more confident on the treatment performed and the elapsed time between the withdrawal and test, have been considered in this analysis.
The red and black dots represents the experimental data while the black line the linear regression of the data marked in red. In particular in samples marked in black, and highlighted with a blue ellipse, a large amount of gametocytes and/or hemozoin crystals have been noticed at Sacco Hospital. Given the higher magnetic susceptibility value of such particles it is plausible that their signal is higher than the one of iRBCs at the same level of parasitaemia.
As can be noticed the data spread around the linear regression line is 5 to 10 times higher than the one registered for tRBCs (see Figure 5.4 in Section 5.2) thus not allowing an adequate and accurate quantification. This is possibly due, on the one hand, to the quantification error of the microscopy analysis; on the other hand, and probably mostly, to the natural inter-person differences in the blood properties, like RBC volume, density, haemoglobin content, haematocrit and plasma viscosity.
All these properties significantly influence the RBCs dynamics in the fluid and, consequently, the signal, as the system relies on their dynamic to isolate and concentrate said

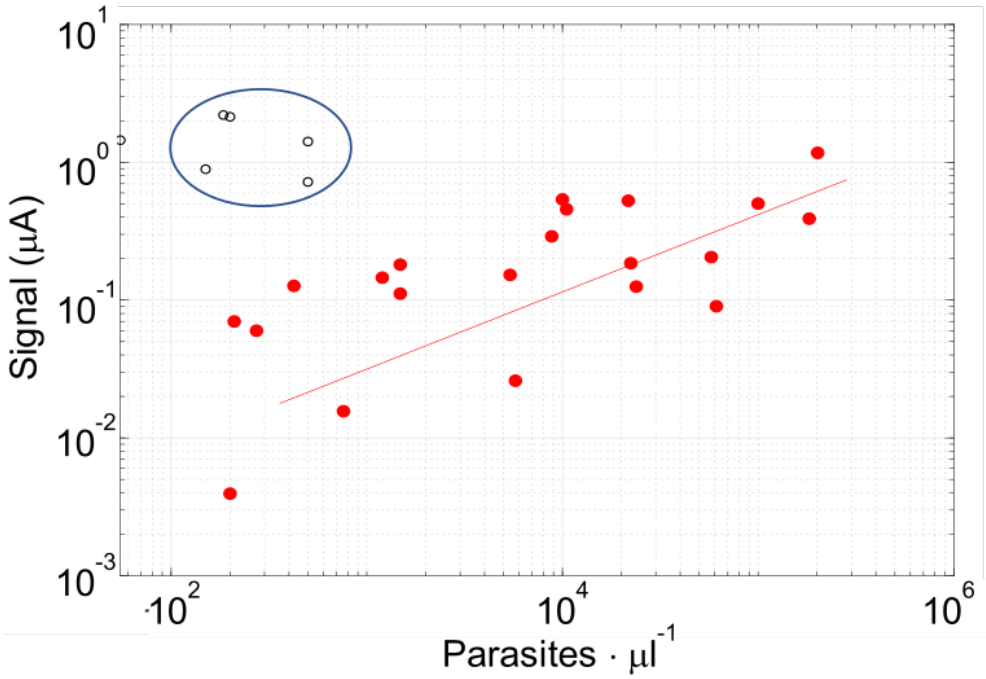

Figure 5.7: *Calibration curve of the signal amplitude as a function of the parasitaemia level estimated at Sacco Hospital from the thick blood smears. The black circles (highlighted by a blue ellipse) represent blood samples in which an high amount of gametocytes and/or free HCs have been observed. The red markers, together with the black ones, represent the experimental data. The red line is their linear regression.*

particles on the chip. The variability in the aforementioned RBCs properties, especially their volume and haematocrit, also affects the impedance variation directly.
In Figure 5.8 photos taken during the test campaign are shown.

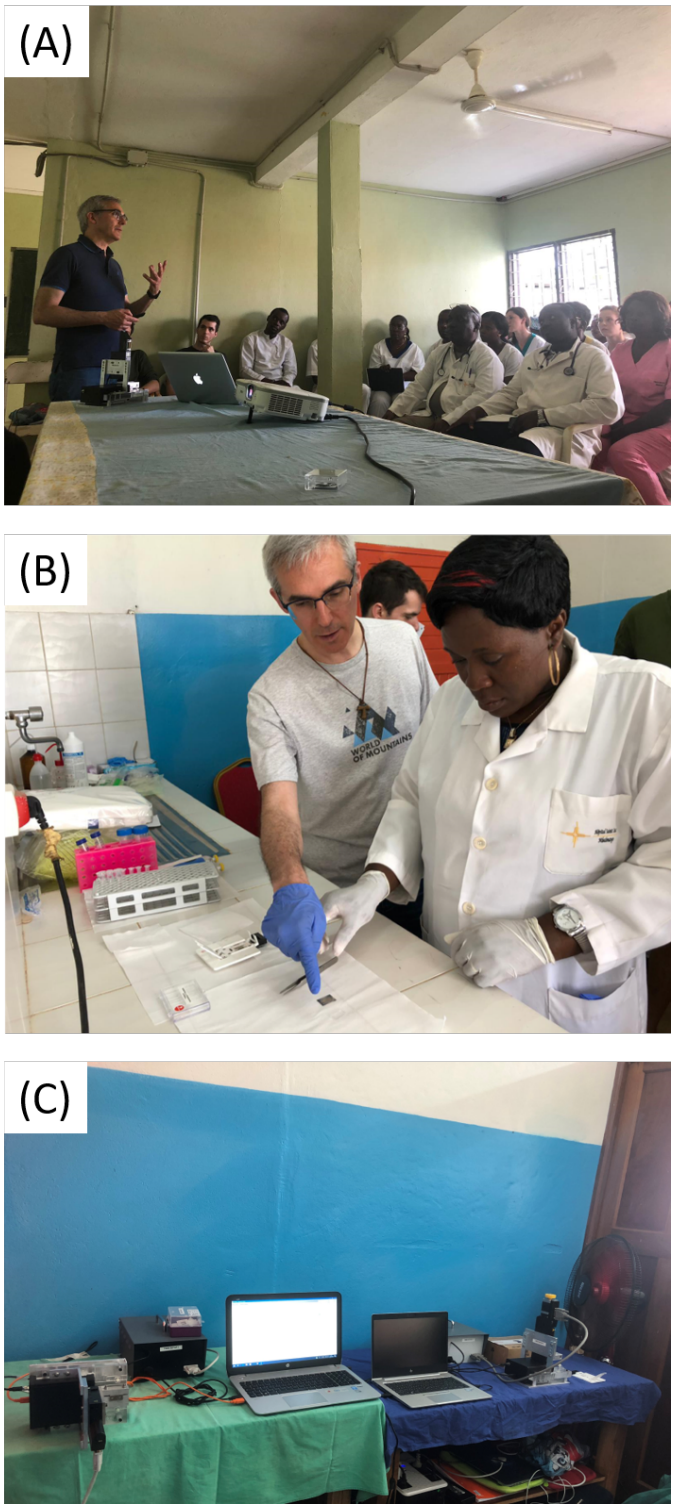

Figure 5.8: *Photos taken during the test campaign at Hopital Saint Luc of Mbalmayo, Cameroon, Africa. (A) Prof. Riccardo Bertacco, coordinator of the project, giving a disclosure speech on how to use Tid Mekii to the medical staff at Hopital Saint Luc. (B) Clinician of Hopital Saint Luc preparing a test with Tid Mekii system under the supervision of Prof. Bertacco. (C) Installation and placement of two Tid Mekii systems at Hopital Saint Luc.*

CHAPTER 6

Conclusions

In this work of thesis a complete system for malaria diagnosis, based on the selective magnetophoretic capture and electrical impedance detection of malaria infected red blood cells, have been designed, fabricated and tested. In particular the Tid Mekii system is an easy to use diagnostic tool able to diagnose and quantify the malaria parasite presence in less than 10 minutes with a limit of detection of 10 parasites/μl, which is the same of the gold standard for malaria diagnosis.
The system comprises a silicon microchip, a custom electronic board, microcontroller firmware, GUI software and a portable and automated experimental setup.
The core of the system is the silicon chip that is composed by two layers which perform different functions. A first layer, thanks to magnetic micro-concentrators made of Ni, selectively attracts and focuses iRBCs and HCs in specific areas of the chip while the second layer, thanks to gold electrodes positioned in said areas, senses the presence of the cells allowing for their quantification.
The two layers have been designed and optimized in order to increase the capture efficiency and the resistance variation associated to the capture of iRBCs. Moreover, the chip implements a differential measurement to reject the spurious conductivity fluctuations of the solution, for example given by a temperature variation. This has enabled a 10^{-4} resolution in the resistance variation measurement.
Thanks to the presence of four identical but independent sensors on the same chip, four parallel measurements on the same sample can be performed simultaneously, increasing the test reliability.
A preliminary study on the attraction capabilities of the designed first layer highlighted a 100% capture efficiency of iRBCs after 3 minutes for some design variants, while a 80% is obtained after 10 min with the final configuration adopted in this thesis.
The fabrication process of the chip has been carried out and optimized at Polifab, the

micro- and nano- technology center of Politecnico di Milano.
The custom electronic board has been designed for an ultra low noise and low cost electrical impedance spectroscopy with a maximum frequency of 20 MHz. The output noise given by the electronics never exceeds 10 μV_{RMS}, which is negligible in respect to the resistance fluctuation of the sensor itself (400μV_{RMS}), that sets the minimum detectable current signal to 20 nA.
The firmware of the microcontroller, which controls the electronic board, together with the software and the experimental setup have been designed and developed to allow a repeatable, easy, and almost completely automated execution of the tests.
A preliminary study has been carried out, aimed to shed light on the not well reported magnetic and electrical properties of hemozoin crystals. During the study, a paramagnetic behaviour with a magnetic susceptibility value $\chi \approx 4.1 \cdot 10^{-4}$ has been obtained while an electrical insulating behaviour, from DC up to MHz frequencies, has been demonstrated experimentally for HCs.
A first session of capture and detection experiments performed on HCs and treated RBCs showed a limit of detection of 3 ng/μl (approximately 10^4 HCs/μl) for the formers and 10^1 for tRBCs as expected from theoretical analysis. In both cases a linear relationship between the electric signals and the particles concentration and a good agreement with the theory has been observed. Hence proving the possibility of the measurement principle to quantify the level of parasitaemia, at least in controlled conditions with an infected red blood cells model.
Subsequently a further investigation carried out at Sacco Hospital on three blood sample, withdrew 0, 24 and 48 hours after the treatment from the same malaria infected patient, demonstrated the possibility to use the quantitative nature of the measurement to also perform a follow up of the status of the disease before and after the treatment.
Moreover, the signal morphology, which depends on the specific properties of the particles analysed, allows to distinguish the different particles in the samples thus the stage of the disease. This feature has been demonstrated through experiments performed at Istituto Superiore di Sanitá in Rome on cultured red blood cells infected by different stages of Plasmodium.
Finally, a preclinical validation campaign have been conducted on 108 patients at Hopital Saint Luc of Mbalmayo in Cameroon, an African region where malaria is endemic. A sensitivity of 100% (95% confidence interval: 90.3% - 100%) and specificity of 65.5% (95% confidence interval: 45.5% - 81.4%) attested the potential of Tid Mekii system to become a successful tool for malaria diagnosis. However a reliable and accurate quantification of the parasitaemia level based on the signal amplitude has not been possible due to the wide inter-patient blood physical properties differences.
Nevertheless further improvements and developments should be put in place to improve its reliability, quantification capability in real blood cases and decrease the number of false positives.
Moreover, the performance indices obtained during the first preclinical campaign should be confirmed by a more extensive future study.

6.1 Future perspectives

During the experimental activities carried out in this thesis, several features of the systems have been highlighted. Some of them like the follow up possibility and Plasmodium stage recognition require further investigation through focused and extensive test campaigns.
The system itself should be optimized, following the experience and knowledge gained, in order to improve the stability and limit of detection of the measurement as well as reducing its cost in view of a possible future commercialization.
In particular a major problem affecting both the stability and the limit of detection of the measurement is the presence of the linear drift superimposed to the signal. In order to minimize its entity a second version of the chip has been designed improving the differential structure of the electrodes,i.e intersecting the measurement and reference electrodes instead of having them on separated areas, as shown in Figure 6.1(C). In this way both the measurement and reference electrodes are subjected to the same environment, thus to the same temperature or conductivity variations, which are the suspected causes of the drift.
The new layout of the sensor is shown in Figure 6.1(D) in which the absence of the two separated areas and their combination can be noticed. Even the structure of the sensitive area has been redesigned with the aim of improving the resolution.
As a matter of fact during the aforementioned experiments a peculiar distribution of the particles on the pillars, in respect to the μ-metal sheet line, has been noticed.
Pillars along or few hundreds micrometer close to said line attract particles along their whole border circumference while in pillars that are on the left or right side of the line it occurs, respectively, on the left or right semicircle border. This phenomenon is linked to the magnetic field lines generated by the magnets assembly, which, along the μ-metal line, are parallel to the pillars axis while oblique to them on the line sides. Moreover, particles fill the pillars border at first, moving gradually to the center when it is filled.
Thus the electrodes sensitive area has been redesigned as shown in Figure 6.1(A) for the electrodes along the μ-metal line and (B) for those on the right side of it (the left side electrodes are simply the mirroring of the latter).
The chip has been successfully fabricated, as shown in Figure 6.2, however it should still be tested and characterized to assess its capability in reducing the drift while increasing the signal.
Moreover a new version of the electronic board will be designed. The main changes that will be made are:

- substitution of the actual stepper motor with a less accurate but more compact and cheaper one;
- power supply of electronics and motor via battery;
- ultra low power design;
- substitution of the actual Arduino Due microcontroller board with a low power, higher performance integrated alternative;
- wireless transmission of data to a PC or portable device.

Due to the motor substitution, also the mechanical setup will be modified accordingly. A new version of the cartridge is currently being redesigned to improve the goodness of the sealing between the chip and glass slide.
Once the system redesign has been made, the new version of Tid Mekii will be extensively tested trough measurement campaigns in malaria endemic area, as already done in Cameroon but on a wider data set.

Figure 6.1: *(A) Layout of the sensitive part of one couple of electrodes along the μ-metal line. (B) Layout of the sensitive part of one couple of electrodes to the right of the μ-metal line. (C) Co-penetration layout scheme of the measurement (in red) and reference (in blue) electrodes. (D) Complete sensor layout in which the measurement and a reference area are combined together.*

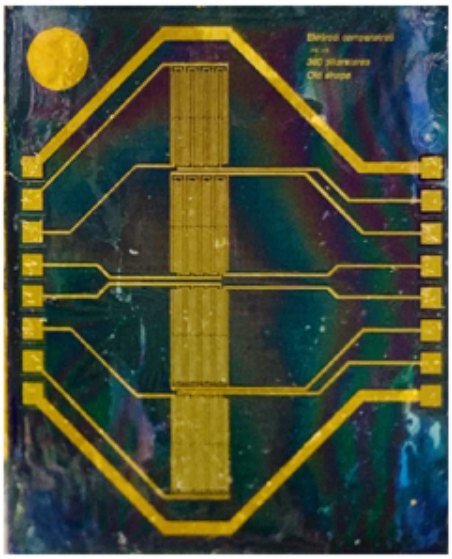

Figure 6.2: *Photograph of the second version of the chip.*

List of Figures

List of Tables

Bibliography

[1] World Health Organization. World Malaria Report 2018. 2018.

[2] World Health Organization. Malaria Fact Sheet, 2016.

[3] Centers for Disease Control and Prevention. About Malaria, 2019.

[4] Carolyn Driver. What is malaria? *Nursing times*, 2002.

[5] Behzad Nadjm and Ron H. Behrens. Malaria: An Update for Physicians, 2012.

[6] John E. Bennett, Raphael Dolin, and Martin J. Blaser. *Mandell, Douglas, and Bennett's Principles and Practice of Infectious Diseases*. 2014.

[7] Hector Caraballo and Kevin King. Emergency department management of mosquito-borne illness: malaria, dengue, and West Nile virus, 2014.

[8] Alessandro Bartoloni and Lorenzo Zammarchi. Clinical aspects of uncomplicated and severe malaria, 2012.

[9] Nicholas A.V. Beare, Terrie E. Taylor, Simon P. Harding, Susan Lewallen, and Malcolm E. Molyneux. Malarial retinopathy: A newly established diagnostic sign in severe malaria. *American Journal of Tropical Medicine and Hygiene*, 2006.

[10] Mary K. Klassen-Fischer and Ronald C. Neafie. *Protozoal infections*. 2008.

[11] Eline L. Korenromp, Brian G. Williams, Sake J. De Vlas, Eleanor Gouws, Charles F. Gilks, Peter D. Ghys, and Bernard L. Nahlen. Malaria attributable to the HIV-1 epidemic, sub-Saharan Africa. *Emerging Infectious Diseases*, 2005.

[12] J.F. Waller. Davidson's Principles and Practice of Medicine. *Postgraduate Medical Journal*, 1992.

[13] Nicholas A.V. Beare, Susan Lewallen, Terrie E. Taylor, and Malcolm E. Molyneux. Redefining cerebral malaria by including malaria retinopathy, 2011.

[14] WHO Report. *World Malaria Report 2017*. 2017.

[15] Eve Worrall, Suprotik Basu, and Kara Hanson. Is malaria a disease of poverty? A review of the literature, 2005.

[16] Brian M. Greenwood, Kalifa Bojang, Christopher J.M. Whitty, and Geoffrey A.T. Targett. Malaria. In *Lancet*, 2005.

[17] Teun Bousema and Chris Drakeley. Epidemiology and infectivity of Plasmodium falciparum and Plasmodium vivax gametocytes in relation to malaria control and elimination, 2011.

[18] Eline L. Korenromp, Brian G. Williams, Sake J. De Vlas, Eleanor Gouws, Charles F. Gilks, Peter D. Ghys, and Bernard L. Nahlen. Malaria attributable to the HIV-1 epidemic, sub-Saharan Africa. *Emerging Infectious Diseases*, 2005.

[19] The biology of parasites. *The Quarterly Review of Biology*.

[20] Alan F. Cowman, Drew Berry, and Jake Baum. The cellular and molecular basis for malaria parasite invasion of the human red blood cell. *Journal of Cell Biology*, 2012.

[21] Elizabeth A. Ashley, Aung Pyae Phyo, and Charles J. Woodrow. Malaria, 2018.

[22] Philip J. Rosenthal and Steven R. Meshnick. Hemoglobin catabolism and iron utilization by malaria parasites, 1996.

[23] Alessandro Esposito, Teresa Tiffert, Jakob M.A. Mauritz, Simon Schlachter, Lawrence H. Bannister, Clemens F. Kaminski, and Virgilio L. Lew. FRET imaging of hemoglobin concentration in Plasmodium falciparum-infected red cells. *PLoS ONE*, 2008.

[24] C. D. Fitch, R. Chevli, P. Kanjananggulpan, P. Dutta, K. Chevli, and A. C. Chou. Intracellular ferriprotoporphyrin IX is a lytic agent. *Blood*, 1983.

[25] C. D. Fitch and P. Kanjananggulpan. The state of ferriprotoporphyrin IX in malaria pigment. *Journal of Biological Chemistry*, 1987.

[26] Silvina Pagola, Peter W. Stephens, D. Scott Bohle, Andrew D. Kosar, and Sara K. Madsen. The structure of malaria pigment β-haematin. *Nature*, 2000.

[27] Ernst Hempelmann. Hemozoin biocrystallization in Plasmodium falciparum and the antimalarial activity of crystallization inhibitors, 2007.

[28] Régis Vanderesse, Ludovic Colombeau, Céline Frochot, and Samir Acherar. Inactivation of Malaria Parasites in Blood: PDT vs Inhibition of Hemozoin Formation. In *Current Topics in Malaria*. 2016.

[29] David J. Sullivan. Theories on malarial pigment formation and quinoline action. In *International Journal for Parasitology*, 2002.

[30] M. Inyushin, Yu Kucheryavih, L. Kucheryavih, L. Rojas, I. Khmelinskii, and V. Makarov. Superparamagnetic Properties of Hemozoin. *Scientific Reports*, 2016.

[31] Lee R. Moore, Hisashi Fujioka, P. Stephen Williams, Jeffrey J. Chalmers, Brian Grimberg, Peter A. Zimmerman, and Maciej Zborowski. Hemoglobin degradation in malaria-infected erythrocytes determined from live cell magnetophoresis. *The FASEB Journal*, 2006.

[32] Linus Pauling and Charles D. Coryell. The Magnetic Properties and Structure of Hemoglobin, Oxyhemoglobin and Carbonmonoxyhemoglobin. *Proceedings of the National Academy of Sciences*, 1936.

[33] A. Roch, J. Prodéo, C. Pierart, R. N. Muller, and P. Duez. The paramagnetic properties of malaria pigment, hemozoin, yield clues to a low-cost system for its trapping and determination. *Talanta*, 2019.

[34] S. Hackett, J. Hamzah, T. M.E. Davis, and T. G. St Pierre. Magnetic susceptibility of iron in malaria-infected red blood cells. *Biochimica et Biophysica Acta - Molecular Basis of Disease*, 2009.

[35] Lorena M. Coronado, Christopher T. Nadovich, and Carmenza Spadafora. Malarial hemozoin: From target to tool. *Biochimica et Biophysica Acta - General Subjects*, 2014.

[36] M. Giacometti, C. Rinaldi, M. Monticelli, L. Callegari, A. Collovini, D. Petti, G. Ferrari, and R. Bertacco. Electrical and magnetic properties of hemozoin nanocrystals. *Applied Physics Letters*, 2018.

[37] Gregory S. Noland, Noelle Briones, and David J. Sullivan. The shape and size of hemozoin crystals distinguishes diverse Plasmodium species. *Molecular and Biochemical Parasitology*, 2003.

[38] Oliver Sabot, Justin M. Cohen, Michelle S. Hsiang, James G. Kahn, Suprotik Basu, Linhua Tang, Bin Zheng, Qi Gao, Linda Zou, Allison Tatarsky, Shahina Aboobakar, Jennifer Usas, Scott Barrett, Jessica L. Cohen, Dean T. Jamison, and Richard G.A. Feachem. Costs and financial feasibility of malaria elimination, 2010.

[39] Kamaraju Raghavendra, Tapan K. Barik, B. P.Niranjan Reddy, Poonam Sharma, and Aditya P. Dash. Malaria vector control: From past to future. *Parasitology Research*, 2011.

[40] World Health Organization. Instructions for treatment and use of insecticide-treated mosquito nets. *World Health Organization, Geneva, Switzerland*, 2002.

[41] Henk Van Den Berg. Global status of DDT and its alternatives for use in vector control to prevent disease, 2009.

[42] World Health Organization. Indoor residual spraying. Use of indoor residual spraying for scaling up global malaria control and elimination. WHO Position Statement. *Tropical Medicine and International Health*, 2006.

[43] Helen Pates and Christopher Curtis. Mosquito behavior and vector control. *Annual Review of Entomology*, 2005.

[44] Lucy S. Tusting, Julie Thwing, David Sinclair, Ulrike Fillinger, John Gimnig, Kimberly E. Bonner, Christian Bottomley, and Steven W. Lindsay. Mosquito larval source management for controlling malaria, 2013.

[45] Maya Tickell-Painter, Nicola Maayan, Rachel Saunders, Cheryl Pace, and David Sinclair. Mefloquine for preventing malaria during travel to endemic areas, 2017.

[46] David R. Hill, Charles D. Ericsson, Richard D. Pearson, Jay S. Keystone, David O. Freedman, Phyllis E. Kozarsky, Herbert L. DuPont, Frank J. Bia, Philip R. Fischer, and Edward T. Ryan. The Practice of Travel Medicine: Guidelines by the Infectious Diseases Society of America. *Clinical Infectious Diseases*, 2006.

[47] Simon Turschner and Thomas Efferth. Drug Resistance in Plasmodium: Natural Products in the Fight Against Malaria. *Mini-Reviews in Medicinal Chemistry*, 2009.

[48] David G. Lalloo, Peju Olukoya, and Piero Olliaro. Malaria in adolescence: burden of disease, consequences, and opportunities for intervention, 2006.

[49] World Health Organization. World Malaria Report. *World Health*, 2010.

[50] Christine Manyando, Kassoum Kayentao, Umberto Dalessandro, Henrietta U. Okafor, Elizabeth Juma, and Kamal Hamed. A systematic review of the safety and efficacy of artemether-lumefantrine against uncomplicated Plasmodium falciparum malaria during pregnancy, 2012.

[51] Geoffrey Pasvol. The treatment of complicated and severe malaria, 2005.

[52] Hmwe Hmwe Kyu and Eduardo Fernández. Artemisinin derivatives versus quinine for cerebral malaria in African children: A systematic review, 2009.

[53] Critical Care Aspects of Malaria, 2010.

[54] N. J. White. Qinghaosu (artemisinin): The price of success, 2008.

[55] Amed Ouattara and Matthew B. Laurens. Vaccines against malaria. *Clinical Infectious Diseases*, 2015.

[56] Peter D. Crompton, Susan K. Pierce, and Louis H. Miller. Advances and challenges in malaria vaccine development, 2010.

[57] Patricia M Graves and Hellen Gelband. Vaccines for preventing malaria (SPf66). *Cochrane Database of Systematic Reviews*, 2006.

[58] Unitaid. Malaria Diagnostics Technology and Market Landscape - 3rd edition (2016). *Unitaid Secretariat World Health Organization*, 2016.

[59] Surasak Kasetsirikul, Jirayut Buranapong, Werayut Srituravanich, Morakot Kaewthamasorn, and Alongkorn Pimpin. The development of malaria diagnostic techniques: A review of the approaches with focus on dielectrophoretic and magnetophoretic methods, 2016.

[60] Noppadon Tangpukdee, Chatnapa Duangdee, Polrat Wilairatana, and Srivicha Krudsood. Malaria diagnosis: A brief review, 2009.

[61] Microscopic Procedures for Diagnosing Malaria.

[62] Wen Zhu, Nancy Zeng, and Ning Wang. Sensitivity, specificity, accuracy, associated confidence interval and ROC analysis with practical SAS® implementations. *Northeast SAS Users Group 2010: Health Care and Life Sciences*, 2010.

[63] Hugh Reyburn, Hilda Mbakilwa, Rose Mwangi, Ombeni Mwerinde, Raimos Olomi, Chris Drakeley, and Christopher J.M. Whitty. Rapid diagnostic tests compared with malaria microscopy for guiding outpatient treatment of febrile illness in Tanzania: Randomised trial. *British Medical Journal*, 2007.

[64] D C Warhurst and J E Williams. ACP Broadsheet no 148. July 1996. Laboratory diagnosis of malaria. *Journal of Clinical Pathology*, 1996.

[65] Mark Amexo, Rachel Tolhurst, Guy Barnish, and Imelda Bates. Malaria misdiagnosis: Effects on the poor and vulnerable, 2004.

[66] D. K. Das, R. Mukherjee, and C. Chakraborty. Computational microscopic imaging for malaria parasite detection: A systematic review. *Journal of Microscopy*, 2015.

[67] Katherine Torres, Christine M. Bachman, Charles B. Delahunt, Jhonatan Alarcon Baldeon, Freddy Alava, Dionicia Gamboa Vilela, Stephane Proux, Courosh Mehanian, Shawn K. McGuire, Clay M. Thompson, Travis Ostbye, Liming Hu, Mayoore S. Jaiswal, Victoria M. Hunt, and David Bell. Automated microscopy for routine malaria diagnosis: A field comparison on Giemsa-stained blood films in Peru. *Malaria Journal*, 2018.

[68] Centers for Disease Control and Prevention, Malaria diagnostic tools.

[69] Pedro Berzosa, Aida De Lucio, María Romay-Barja, Zaida Herrador, Vicenta González, Luz García, Amalia Fernández-Martínez, Maria Santana-Morales, Policarpo Ncogo, Basilio Valladares, Matilde Riloha, and Agustín Benito. Comparison of three diagnostic methods (microscopy, RDT, and PCR) for the detection of malaria parasites in representative samples from Equatorial Guinea 11 Medical and Health Sciences 1108 Medical Microbiology. *Malaria Journal*, 2018.

[70] Gillian H. Stresman, Jennifer C. Stevenson, Nnenna Ngwu, Elizabeth Marube, Chrispin Owaga, Chris Drakeley, Teun Bousema, and Jonathan Cox. High levels of asymptomatic and subpatent Plasmodium falciparum parasite carriage at health facilities in an area of heterogeneous malaria Transmission intensity in the Kenyan highlands. *American Journal of Tropical Medicine and Hygiene*, 2014.

[71] Lilit Garibyan and Nidhi Avashia. Polymerase chain reaction. *Journal of Investigative Dermatology*, 2013.

[72] Mallika Imwong, Sarun Hanchana, Benoit Malleret, Laurent Rénia, Nicholas P.J. Day, Arjen Dondorp, Francois Nosten, Georges Snounou, and Nicholas J. White. High-throughput ultrasensitive molecular techniques for quantifying low-density malaria parasitemias. *Journal of Clinical Microbiology*, 2014.

[73] Michael S. Cordray and Rebecca R. Richards-Kortum. Review: Emerging nucleic acid-based tests for point-of-care detection of malaria, 2012.

[74] Smitha Surendran Thamarath, Aoli Xiong, Po Han Lin, Peter Rainer Preiser, and Jongyoon Han. Enhancing the sensitivity of micro magnetic resonance relaxometry detection of low parasitemia Plasmodium falciparum in human blood. *Scientific Reports*, 2019.

[75] Stefan Miltenyi, Werner Müller, Walter Weichel, and Andreas Radbruch. High gradient magnetic cell separation with MACS. *Cytometry*, 1990.

[76] World Health Organization. Malaria Diagnosis Introduction objectives of the meeting. *World Health Organization*, 2000.

[77] William M. Spees, Dmitriy A. Yablonskiy, Mark C. Oswood, and Joseph J.H. Ackerman. Water proton MR properties of human blood at 1.5 Tesla: Magnetic susceptibility, T1, T2*, T2, and non-Lorentzian signal behavior. *Magnetic Resonance in Medicine*, 2001.

[78] Maciej Zborowski, Graciela R. Ostera, Lee R. Moore, Sarah Milliron, Jeffrey J. Chalmers, and Alan N. Schechter. Red blood cell magnetophoresis. *Biophysical Journal*, 2003.

[79] Xiaoxia Jin, Yang Zhao, Aaron Richardson, Lee Moore, P. Stephen Williams, Maciej Zborowski, and Jeffrey J. Chalmers. Differences in magnetically induced motion of diamagnetic, paramagnetic, and superparamagnetic microparticles detected by cell tracking velocimetry. *Analyst*, 2008.

[80] P. Sajeesh and Ashis Kumar Sen. Particle separation and sorting in microfluidic devices: A review, 2014.

[81] Adam C. Siegel, Sergey S. Shevkoplyas, Douglas B. Weibel, Derek A. Bruzewicz, Andres W. Martinez, and George M. Whitesides. Cofabrication of electromagnets and microfluidic systems in poly(dimethylsiloxane). *Angewandte Chemie - International Edition*, 2006.

[82] E. P. Furlani. Analysis of particle transport in a magnetophoretic microsystem. *Journal of Applied Physics*, 2006.

[83] Ki Ho Han and A. Bruno Frazier. Paramagnetic capture mode magnetophoretic microseparator for high efficiency blood cell separations. *Lab on a Chip*, 2006.

[84] Siddharth Vyas, Vladimir Genis, and Gary Friedman. Computational study of a magnetic design to improve the diagnosis of malaria: 2D model. *Journal of Magnetism and Magnetic Materials*, 2017.

[85] Ki Ho Han and A. Bruno Frazier. Continuous magnetophoretic separation of blood cells in microdevlce format. *Journal of Applied Physics*, 2004.

[86] Jeonghun Nam, Hui Huang, Hyunjung Lim, Chaeseung Lim, and Sehyun Shin. Magnetic separation of malaria-infected red blood cells in various developmental stages. *Analytical Chemistry*, 2013.

[87] Simão Nunes Paula. *Exploring impedance spectroscopy as a mean of malaria diagnostic*. PhD thesis, IST, Lisbon, Portugal, 2014.

[88] Jeong Eun Hyeon, Da Woon Jeong, Young Jin Ko, Seung Wook Kim, Chulhwan Park, and Sung Ok Han. Biomimetic magnetoelectric nanocrystals synthesized by polymerization of heme as advanced nanomaterials for biosensing application. *Biosensors and Bioelectronics*, 2018.

[89] Ruben A. Dilanian, Victor Streltsov, Hannah D. Coughlan, Harry M. Quiney, Andrew V. Martin, Nectarios Klonis, Con Dogovski, Sébastien Boutet, Marc Messerschmidt, Garth J. Williams, Sophie Williams, Nicholas W. Phillips, Keith A. Nugent, Leann Tilley, and Brian Abbey. Nanocrystallography measurements of early stage synthetic malaria pigment. *Journal of Applied Crystallography*, 2017.

[90] Silvina Pagola, Peter W. Stephens, D. Scott Bohle, Andrew D. Kosar, and Sara K. Madsen. The structure of malaria pigment β-haematin. *Nature*, 2000.

[91] M. Ibrahim, J. Claudel, D. Kourtiche, B. Assouar, and M. Nadi. Physical and electrical modeling of interdigitated electrode arrays for bioimpedance spectroscopy. In *Lecture Notes in Electrical Engineering*, 2011.

[92] J. Ross Macdonald. Impedance spectroscopy. *Annals of Biomedical Engineering*, 1992.

[93] Keith Leaver. Conduction in Semiconductors. In *Microelectronic Devices*. 1997.

[94] https://gibbslabblog.files.wordpress.com/2017/03/edl.jpg.

[95] M. Endo et Al. High Power Electric Double Layer Capacitor (EDLC's); from Operating Principle to Pore Size Control in Advanced Activated Carbons. *Carbon letters*, 2001.

[96] Keith B. Oldham. A Gouy-Chapman-Stern model of the double layer at a (metal)/(ionic liquid) interface. *Journal of Electroanalytical Chemistry*, 2008.

[97] H. L. Lord, W. Zhan, and J. Pawliszyn. Fundamentals and applications of needle trap devices. In *Comprehensive Sampling and Sample Preparation*. 2012.

[98] M. Ibrahim, J. Claudel, D. Kourtiche, and M. Nadi. Geometric parameters optimization of planar interdigitated electrodes for bioimpedance spectroscopy. *Journal of Electrical Bioimpedance*, 2013.

[99] S. Gawad, L. Schild, and Ph Renaud. Micromachined impedance spectroscopy flow cytometer for cell analysis and particle sizing. *Lab on a Chip*, 2001.

[100] C. G. Granqvist and O. Hunderi. Conductivity of inhomogeneous materials: Effective-medium theory with dipole-dipole interaction. *Physical Review B*, 1978.

[101] D. Stroud. Generalized effective-medium approach to the conductivity of an inhomogeneous material. *Physical Review B*, 1975.

[102] M. Carminati, L. Pedalà, E. Bianchi, F. Nason, G. Dubini, L. Cortelezzi, G. Ferrari, and M. Sampietro. Capacitive detection of micrometric airborne particulate matter for solid-state personal air quality monitors. *Sensors and Actuators, A: Physical*, 2014.

[103] Cosimo Longo Damiano. *Progetto e realizzazione di un sensore di capacità per misure in liquido ad elevata stabilità*. PhD thesis, Politecnico di Milano, 2017.

[104] S. A. Pactitis and S. A. Pactitis. Sallen-Key Filters. In *Active Filters*. 2014.

[105] Robert A. Greenwald. *Handbook methods for oxygen radical research*. 2018.

[106] W. G. Zijlstra and A. Buursma. Spectrophotometry of hemoglobin: Absorption spectra of bovine oxyhemoglobin, deoxyhemoglobin, carboxyhemoglobin, and methemoglobin. *Comparative Biochemistry and Physiology - B Biochemistry and Molecular Biology*, 1997.

Appendix

In order to better understand the magnetic field and relative gradient produced both by the magnet assembly and the Ni pillars, numerical simulations have been carried out using COMSOL 5.3a.
For this purpose two COMSOL modules have been exploited: *Magnetic fields, no currents* and *Particle tracing*. In particular, the former allows to simulate static magnetic fields distribution in space and their interaction with materials. The latter is used to simulate the motion of particles in a fluid subjected to different kind of forces like: magnetophoretic, Dielectrophoretic, Acustophoretic, gravity, Brownian, drag, buoyancy, particle-particle interactions etc.
In this Appendix, the simulations of the magnetic field gradient generated by the Ni pillars geometry and its influence on the motion of the particle will be described in detail.
In Figure 6.3(a) the simulation geometry is shown. All the material and particles properties as well as the geometric parameters of the simulation are listed in Table 6.1.

The 3D geometry consists of a parallelepiped made of air with a height, H_{air}, width and depth, W_{air}. Inside the aforementioned block, a small portion of the chip, comprising seven pillars, is placed. The 20 μm heigh magnetic concentrators, made of Ni, are placed on top of a cylinder with a height of 40 μm and a radius slightly bigger than the pillar center-center distance, s, representing the portion of fluid between the glass slide and the chip interested by the pillars above. The fluid is a blood plasma and PBS solution 1:10, whit dynamic viscosity, $v_{PBS\&plasma}$ and density, $\rho_{PBS\&plasma}$. The pillars are placed at a distance of 2 μm from the fluid due to the gap given by the SiO_2 layer deposited on the chip surface.
An external magnetic flux density, B, equal to the one generated by the permanent magnets, is applied on the top surface of the parallelepiped pointing downwards, while the bottom surface is set at zero magnetic scalar potential. Such magnetic flux density magnetize the Ni pillars causing their saturation. Consequently the demagnetizing field, generated by pillars, locally perturbs the external magnetic field thus generating a magnetic field gradient. In Figure 6.3(b) the intensity of the gradient of the square of the magnetic field, ∇H^2, is shown in logarithmic scale by the colour plot, while its direction by the red arrows.
As expected, ∇H^2 is higher close to the pillars, decreasing rapidly moving away from them. In particular the maximum gradient is found on the pillars edges, as, the fictitious magnetic charges, similarly to electric ones, accumulate on the edges. Thus, particles will be mainly attracted on the pillars circumference. Moreover it can be noticed that the direction of the gradient between the pillars is opposite to the y-axis thus causing a repulsion from the chip of particles with $\Delta\chi_{PBS-plasma} > 0$. The direction flips moving towards the pillars centers becoming first perpendicular and then concordant to the y-axis.
Subsequently the obtained magnetic field distribution is exploited to simulate t-RBCs trajectory towards the Ni pillars. Magnetophoretic, drag and gravity forces have been considered in the simulation. Moreover, a force along the z-axis, $F_{magnets}$ = 1.4·10^{-13} N, representing the magnetophoretic force caused by the magnetic field gradient generated by the permanent magnets, has been added to the simulation. Assuming that the t-RBCs are almost completely sedimented on the glass slide before the application of the permanent magnets, as it will be the case of the experiments shown in Section 2.5, the particles are released only in a 4 μm thick fluid layer above the bottom of the glass slide. In Figure 6.4 the simulated trajectories of the particles are shown. As can be noticed, particles, starting from the bottom of the fluid are concentrated, moving parallel to the bottom, by the nearest pillar and attracted, moving against gravity as expected from the direction of the magnetic field gradient shown in Figure 6.4(b).

On the top circle of the cylinder representing the portion of fluid between the glass slide and the chip, a particle

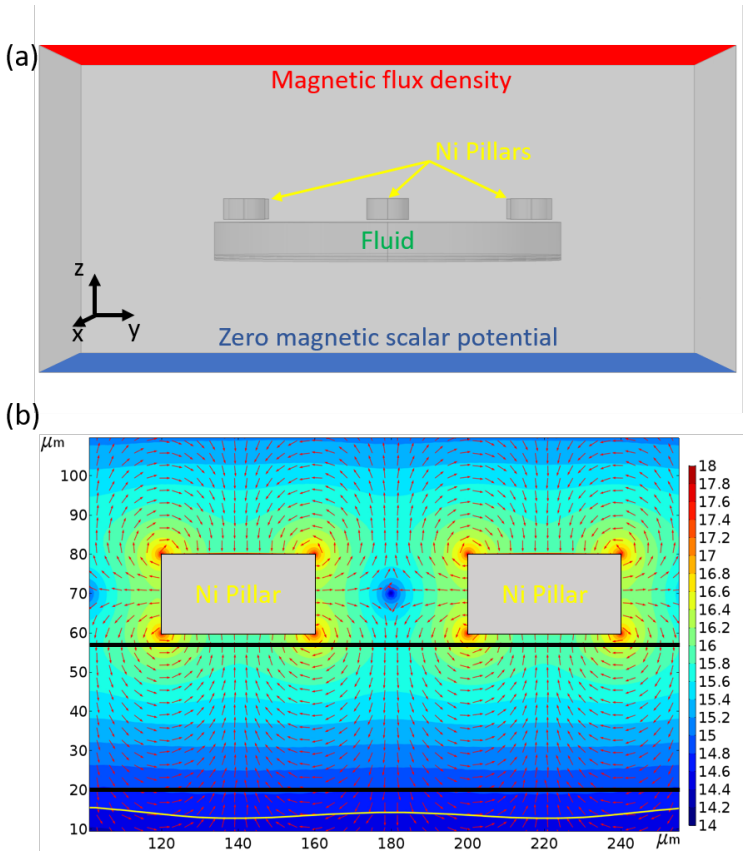

Figure 6.3: *(a) Geometry adopted for the finite element simulations of the magnetic field gradient generated by the Ni pillars and iRBCs trajectory using Comsol 5.3a. (b) Simulation of the magnetic field gradient generated by the 40-80 Ni pillars geometry. The colour plot reports log10(∇H^2) intensity, the red arrows its direction.*

counter has been put. The particle counter counts the number of particles coming into contact with said surfaces, thus enabling to obtain the number of particles attracted as a function of time.
The results of these simulations as well as their agreement with real experiments are shown in Figure 2.9 in Section 2.5.

A similar approach has been exploited to simulate the magnetic field gradient of the permanent magnets assembly, as has been reported in Figure 2.2 in Section 2.3.
Different geometries of the assembly have been simulated to find the geometry offering the best performance in term of magnetic field gradient, thus providing an indispensable support during the design phase of the assembly.
Here we only report the simulation of the final geometry.
For this purpose a 2D simulation has been exploited using only the *Magnetic fields, no currents*. Two rectangles 25x6 mm^2, representing the two permanent magnets, with a third 0.1x25 mm^2 rectangle between them, representing the μ-metal sheet, has been inserted, centered, in a 100x100 mm^2 of air.
Two equal but opposites magnetizations of 950 kA/m have been applied to the two magnets (N42 grade) while the μ-metal magnetic permeability has been set to 2.5.

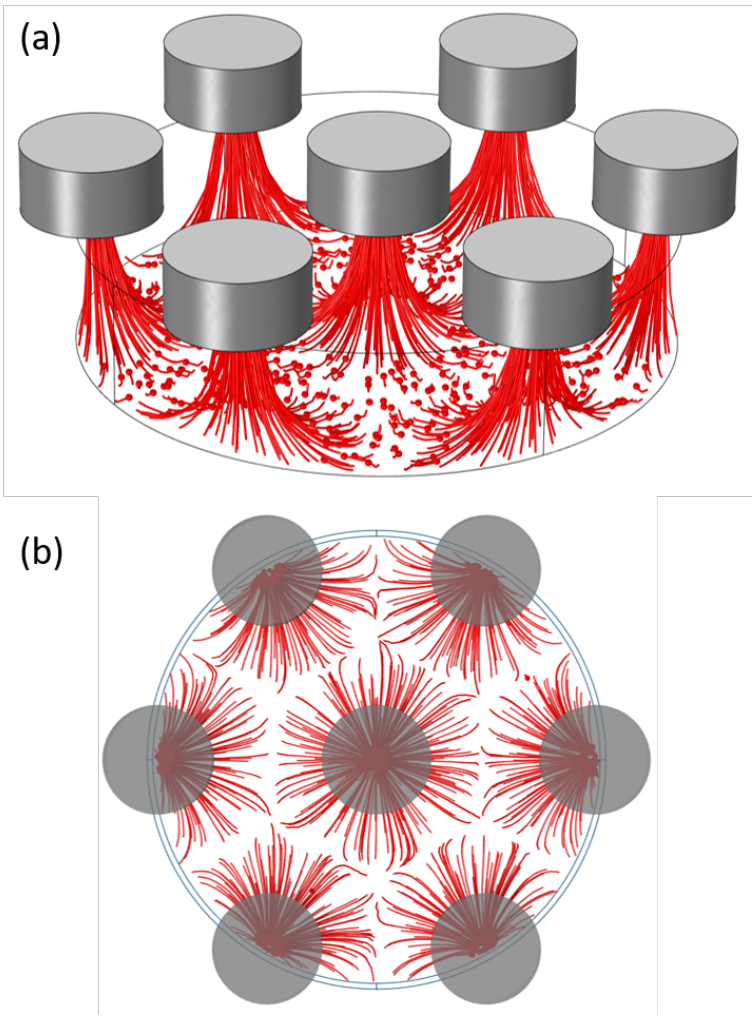

Figure 6.4: *Finite element simulations of iRBCs capture trajectory on a 40 μm diameter and 80 μm spacing pillars geometry using Comsol 5.3a. (a) Side view, (b) top view.*

Table 6.1: *Parameters and constants used in the numerical simulations.*

Parameter	Description	Value
d	Pillars diameter	20, 40 μm
s	Pillars center-center spacing	80, 160 μm
h	Pillars height	20μm
H_{air}	Air volume height	300 μm
W_{air}	Air volume width and depth	4·s
H_{fluid}	Fluid volume height	40 μm
D_{fluid}	Fluid volume diameter	1.1·s
μ_{air}	Air relative permeability	1.00000037
$v_{PBS\&plasma}$	Fluid dynamic viscosity	$1.05{\cdot}10^{-3}$ Pa·s
$\rho_{PBS\&plasma}$	Fluid density	1010 kg/m^3
$\Delta\chi_{RBC-Plasma}$	RBC magnetic susceptibility in respect to the surrounding fluid	$3.9{\cdot}10^{-6}$
B	External magnetic flux density	0.9 T
μ_{Ni}	Nickel magnetic permeability	300
M_{Ni}, sat	Nickel saturation magnetization	477 kA/m[1]
ρ_{RBC}	RBC density	1150 kg/m^3
V_{RBC}	RBC volume	$9.1{\cdot}10^{-11}$ cm^3
$F_{magnets}$	Magnetophoretic force generated by the magnet assembly	$9.1{\cdot}10^{-11}$ cm^3